

# Interplay between Geometry and Fluid Properties

Von der Fakultät für Mathematik und Physik der Universität  
Stuttgart zur Erlangung der Würde eines Doktors der  
Naturwissenschaften (Dr. rer. nat.) genehmigte Abhandlung

Vorgelegt von

Peter-Michael König

aus Würzburg

Hauptberichter: Prof. Dr. S. Dietrich

Mitberichter: Prof. Dr. C. Bechinger

Tag der mündlichen Prüfung: 9. Februar 2005

Institut für Theoretische und Angewandte Physik  
Universität Stuttgart

Max-Planck-Institut für Metallforschung  
Stuttgart

2005

# Contents

<b>Abstract</b>	<b>1</b>
<b>1 Basic Concepts</b>	<b>4</b>
1.1 Density-Functional Theory . . . . .	5
1.2 Fundamental-Measure Theory . . . . .	7
1.3 High Temperature Expansion Theory . . . . .	11
1.4 Effective Potentials . . . . .	12
<b>2 Fluids at Curved Interfaces</b>	<b>16</b>
2.1 Excess Adsorption and Interfacial Tension . . . . .	16
2.2 Sum Rules and Contact Density . . . . .	19
<b>3 Shape Dependence of Thermodynamic Quantities</b>	<b>22</b>
3.1 Morphometric Thermodynamics . . . . .	22
3.2 Morphometric Form of Thermodynamic Quantities . . . . .	27
3.3 Numerical Results . . . . .	29
3.3.1 Thermodynamic Coefficients . . . . .	30
3.3.2 Applications . . . . .	34

---

3.3.3	Accuracy and Error Estimates . . . . .	44
3.3.4	Beyond Pure Hard-Core Interactions . . . . .	46
3.4	Summary . . . . .	50
<b>4</b>	<b>Shape Dependence of Density Profiles</b>	<b>53</b>
4.1	Curvature Expansion of the Density Profile . . . . .	54
4.2	Implications . . . . .	58
4.3	Asymptotic Form of Density Profiles . . . . .	61
<b>5</b>	<b>Depletion Potentials</b>	<b>70</b>
5.1	Preparatory Considerations . . . . .	71
5.2	Spherical-Nonspherical Setup . . . . .	73
5.3	Depletion Potential Between Two Convex Objects . . . . .	78
5.4	Depletion Potential in Key-Lock Systems . . . . .	80
<b>6</b>	<b>Summary and Outlook</b>	<b>92</b>
<b>A</b>	<b>Geometric Quantities</b>	<b>95</b>
<b>B</b>	<b>Obtaining Curvature Expansion Coefficients</b>	<b>100</b>
	<b>Bibliography</b>	<b>104</b>

# Wechselspiel zwischen Geometrie und Flüssigkeitseigenschaften

“Nehmen wir an, die Kuh sei eine Kugel im Vakuum” - viele kennen wohl den Witz, in dem ein Physiker mit ebendiesen Worten seine Theorie zur Ertragssteigerung der Milchkühe einleitet. Obwohl dieser Lösungsansatz für das Problem auf den ersten Blick albern erscheinen mag, so illustriert er doch eines der erfolgreichsten Prinzipien der Physik, nämlich die Idealisierung realer Systeme. Erst mit einfachen Modellen lässt sich die ungeheure Vielfalt physikalischer Phänomene in der Natur verstehen. Dabei ist jedoch Vorsicht geboten, denn entscheidend für die Entwicklung von erfolgreichen Modellen ist es, die tatsächlich relevanten Eigenschaften eines Systems zu identifizieren und geeignet abzubilden. Oft ist das eine Gratwanderung, denn nicht alles, was für eine zufriedenstellende Detailtreue nötig ist, ist auch theoretisch beschreibbar. Gerade die oft in der Natur vorkommenden geometrischen Formen sind oftmals zu komplex, um diese in berechenbare Modelle zu integrieren. In günstigen Fällen reicht es, auf einfachere Geometrien auszuweichen. Es gibt aber auch Objekte, die man nicht durch eine einfache Kugel annähern sollte, um im Bild des Witzes zu bleiben. Auch ein Vakuum ist zuweilen keine sonderlich realistische Beschreibung der Umgebung.

Interessante Systeme, für die eine Näherung der Teilchen durch Kugeln im Vakuum sicherlich fehlschlägt, finden sich vielfach in jeder lebenden Zelle. Wir wollen davon den Wirkungsmechanismus von Enzymen näher betrachten. Diese Biokatalysatoren werden benötigt, um biochemische Vorgänge gezielt zu steuern. Erst die Anwesenheit von eben jenen Enzymen setzt die Energiebarriere der biochemischen Reaktion hinreichend herab, so dass eine schnelle Umsetzung der Edukte möglich ist. Neben dieser Effizienzsteigerung ist im Hinblick auf die Steuerungsfunktion von Enzymen deren Selektivität von besonderer Bedeutung. Darunter versteht man, dass immer jeweils nur genau eine Reaktion durch ein Enzym beschleunigt wird. Diese Tatsache beschreibt man mit einem Schlüssel-Schloss-Bild, in dem nur das passende Edukt in ein Schlossmolekül passt und dort eine Reaktion auslösen kann.

Im Vorfeld einer enzymatischen Reaktion müssen die Moleküle an einem Ort zusammenkommen. Nimmt man an, dass überhaupt keine Kräfte zwischen beiden Teilchen wirken, dann führen diese eine zufällige Relativbewegung aus und es ist sehr unwahrscheinlich, dass Schlüssel und Schloss zueinander finden. Die Reaktionsrate wäre dementsprechend niedrig und das System als Ganzes betrachtet äußerst ineffizient. Quantitative Überlegungen zeigen, dass dies keineswegs der Fall ist. Demnach existiert ein Wechselwirkungspotential zwischen Schlüssel und Schloss, das die Moleküle nicht nur richtig orientiert, sondern diese auch geeignet zusammenführt.

Es gibt eine Vielzahl physikalischer Mechanismen, die für eine solche Anziehung in Frage kommen. Elektrostatische Ladungen auf den Molekülen führen zu Coulombkräften, van-der-Waals Wechselwirkungen entstehen bei der Kopplung von Dipolen und Wasserstoffbrückenbindungen entstehen zwischen einem Wasserstoffatom und einem entsprechenden Heteroatom. All die erwähnten Kräfte sind jedoch chemisch spezifisch, d.h. sie hängen von dem konkreten molekularen Aufbau der beteiligten Moleküle ab. Wären diese also für das nötige Wechselwirkungspotential verantwortlich, so müssten Freiheitsgrade beim Aufbau von Biomolekülen dazu verwendet werden, geeignete Potentiale zu erzeugen. Das ist unwahrscheinlich, denn effizienter wäre ein Mechanismus, der chemisch nicht spezifisch ist und somit bei einer großen Anzahl von Schlüssel-Schloss-Systemen anwendbar ist.

Im Zusammenhang mit Kräften in einer Zelle ist zu beachten, dass das Zytoplasma eine dichte Mischung aus verschiedenen Molekülen und Ionen ist. Die gesamte Packungsdichte der Teilchen ist sehr hoch und man kann davon ausgehen, dass eine vollständige Beschreibung jedes Schlüssel-Schloss-Systems auch den Einfluss der umgebenden Moleküle mit in Betracht ziehen muss. Deren Einfluss kann theoretisch durch eine effektive Wechselwirkung quantifiziert werden, welche in den letzten Jahren als ein wichtiger Beitrag zu intermolekularen Kräften identifiziert wurde. Ein qualitatives Ergebnis einfacher theoretischer Überlegungen mit kugelförmigen Enzymen ist, dass eine anziehende Kraft zwischen Schlüssel und Schloss wirkt, welche die Effizienz der Enzyme günstig beeinflusst. Genauere Überlegungen zeigen jedoch, dass die Annäherung des Schlüssels stets durch eine Energiebarriere verhindert wird. Wir identifizieren in Section 5.4 die einfache sphärische Form des Schlüssels als Ursache für die hohe energetische Barriere und zeigen mit einem einfachen Modell, dass hinreichend asphärischen Schlüssel-moleküle nicht nur die Attraktivität der effektiven Kräfte nutzen können, sondern auch durch entropische Drehmomente geeignet orien-

tiert werden.

Das Berechnen von effektiven Wechselwirkungen zwischen asphärischen Teilchen anhand von direkten Methoden ist extrem aufwändig in Bezug auf die numerische Rechenzeit, da solche Systeme in der Regel auf einem dreidimensionalen Gitter in einem Computer abgebildet werden müssen. Anstatt auf den massiven Einsatz von Computerleistung zu setzen, verfolgen wir in dieser Arbeit einen systematischen Weg um den Einfluss der Geometrie auf verschiedene Aspekte von Flüssigkeiten zu studieren. Dabei steuern wir in drei Schritten auf die Berechnung der erwähnten effektiven Wechselwirkungen hin, welche auch die Arbeit als solche gliedern. Im Einzelnen lassen sich die Kapitel wie folgt zusammenfassen.

**Kapitel 1.** Es wird ein kurzer Abriss über die in der Arbeit verwendeten Methoden gegeben. Der Leser wird mit den wichtigen Größen vertraut gemacht und es werden Quellen für weiterführende Informationen zitiert. Die Dichtefunktionaltheorie (DFT) ist die Basis für viele weiterführende Überlegungen in dieser Arbeit und insbesondere ihre Anwendung auf eine Flüssigkeit von harten Kugeln wird detailliert diskutiert. Die modernsten Theorien für solche Systeme beruhen auf der Fundamentalmaßtheorie von Rosenfeld [15] und erlauben eine äußerst genaue Berechnung von thermodynamischen Observablen. Hartkugelflüssigkeiten sind sehr gut studierte Systeme, sie verhalten sich athermisch und haben nur eine stabile fluide Phase für Packungsdichten  $\eta \leq 0.494$ . In einigen Fällen ist es interessant, auch Systeme mit nicht ausschließlich harten Wechselwirkungen zu betrachten. Dazu verwenden wir eine Störungstheorie, die so genannte Hochtemperaturentwicklung, die ebenfalls in diesem Kapitel vorgestellt wird. Schließlich widmen wir uns der Berechnung von effektiven Wechselwirkungen mit Methoden der DFT.

**Kapitel 2.** Flüssigkeiten an gekrümmten Wänden bilden Grenzflächen mit interessanten physikalischen Effekten. Um diese zu beschreiben verwenden wir die Größen, welche in diesem Kapitel vorgestellt werden. Dazu werden zunächst die Konzepte des “dividing interface” und des “bulk reference systems” nachvollzogen, mit einem besonderen Augenmerk auf Feinheiten, die im Zusammenhang mit gekrümmten Wänden besonders zu beachten sind. Wir definieren die Exzessadsorption  $\Gamma$  und die Grenzflächenspannung  $\gamma$ . Diese beiden thermodynamischen Größen sind nicht unabhängig, sondern durch Summenregeln miteinander verknüpft. In diesem Zusammenhang wird eine weitere zentrale Größe in dieser Arbeit, nämlich die mittlere Kontaktdichte  $\bar{\rho}^c$  an einer harten Wand definiert. Drei Summenregeln, welche wir ableiten, setzen  $\Gamma$ ,

$\gamma$  und  $\bar{p}^c$  miteinander in Beziehung und erweisen sich in den folgenden Kapiteln als sehr nützliche Relationen, da sie unter sehr allgemeinen Annahmen hergeleitet werden können und somit für eine große Klasse von Flüssigkeiten gelten.

**Kapitel 3.** Üblicherweise ist es extrem aufwändig, Flüssigkeitseigenschaften an komplex gekrümmten Wänden zu berechnen. In diesem Kapitel beschäftigen wir uns zunächst mit *thermodynamischen* Eigenschaften, denjenigen Eigenschaften also, die für eine statistische Beschreibung eines Systems verwendet werden. Dazu analysieren wir die Abhängigkeit des großkanonischen Potentials  $\Omega$  von der Geometrie des Systems  $S$ . Letzteres definieren wir als die Menge aller Punkte, die von den Flüssigkeitsteilchen erreicht werden können. Um  $\Omega[S]$  zu bestimmen nutzen wir die bekannte Annahme, dass thermodynamische Potentiale extensive Größen sind und deshalb proportional zu der “Größe” des Systems  $S$  skalieren. Der Ausdruck “Größe” ist üblicherweise nicht näher definiert und man assoziiert damit meist das Volumen  $V[S]$  eines Systems  $S$ , so dass man als Ansatz  $\Omega[S] = \omega \cdot V[S]$  verwendet. Dieser Ansatz gilt jedoch nur, wenn man den Einfluss der Wand, welche  $S$  umgibt, vernachlässigen kann. Ansonsten führt man weitere Terme ein, um den Einfluss zu erfassen. In diesem Zusammenhang definiert man Oberflächen-, Linien- und Punktspannungen, oder für nicht durch Ebenen begrenzte Objekte auch eine unendliche Entwicklung in Potenzen der Wandkrümmungen.

In unserem Ansatz konkretisieren wir, ausgehend vom Extensivitätsbegriff, die Geometrieabhängigkeit von freien Energien. Wir fordern insbesondere von einem thermodynamischen Potential, dass es unabhängig von der Lage und Orientierung des Systems im Raum ist, dass es stetig von der Geometrie des Systems abhängt und dass für zwei beliebige Systeme  $S_1$  und  $S_2$  die folgende Additivitätsrelation gilt:  $\Omega[S_1 \cup S_2] = \Omega[S_1] + \Omega[S_2] - \Omega[S_1 \cap S_2]$ . Demnach muss sich ein Potential additiv aus Subsystemen zusammensetzen lassen und eventuell doppelt gezählte Bereiche  $S_1 \cap S_2$  werden nachträglich abgezogen. Diese drei Annahmen erweitern den gewöhnlichen Extensivitätsbegriff und wir bezeichnen eine Größe, die diese drei Eigenschaften erfüllt, als morphometrisch. Ist  $\Omega[S]$  morphometrisch, dann besagt das Hadwiger Theorem, dass die *allgemeinste* funktionale Form gegeben ist durch

$$\Omega[S] = -pV[S] + \sigma A[S] + \kappa C[S] + \bar{\kappa} X[S]. \quad (1)$$

Dabei sind  $p$  der Druck,  $\sigma$  die Oberflächenspannung an der ebenen Wand und  $\kappa$  und  $\bar{\kappa}$  Biegesteifigkeiten. Diese vier Größen sind intensiv, d.h. unabhängig von der Geo-

metrie des Systems  $S$ . Hingegen sind die konjugierten Größen  $V[S]$ ,  $A[S]$ ,  $C[S]$  und  $X[S]$  morphometrisch und beschreiben die Abhängigkeit von  $\Omega[S]$  von der Geometrie. Es sind die einzigen thermodynamisch relevanten Größen, die etwas mit Geometrie zu tun haben. Die multiplikative Trennung in intensive und konjugiert morphometrische Größen für das thermodynamischen Potential in Gleichung (1) ist äußerst praktisch, weil dies eine Anwendung auch auf kompliziert geformte Geometrien ermöglicht. Neben den geometrischen Maßen müssen nur die intensiven Parameter bekannt sein, wobei letztere in einfachen geometrischen Systemen im Vorfeld bestimmt werden können.

Die Konsequenzen aus der morphometrischen Form des großkanonischen Potentials  $\Omega$  für die thermodynamischen Größen Exzessadsorption  $\Gamma$ , Grenzflächenspannung  $\gamma$  und mittlerer Kontaktdichte  $\bar{\rho}^c$  sind, dass diese eine morphometrische Form besitzen. Das bedeutet, dass die Krümmungsabhängigkeit dieser Größen *ausschließlich* durch lineare Terme in der mittleren und der Gausschen Krümmung  $H$  und  $K$  beschrieben werden kann. In diesem Zusammenhang ist eine geschickte Wahl des “dividing interface” von entscheidender Bedeutung. Nur damit bricht die Krümmungsentwicklung der thermodynamischen Größen bereits nach der linearen Ordnung in  $H$  und  $K$  ab und besteht nicht, wie meist angenommen, aus einer unendlichen Reihe von höheren Krümmungsordnungstermen.

Wir können nicht beweisen, dass  $\Omega$  für eine nichttriviale Flüssigkeit die gewünschten drei Eigenschaften hat, dass also die “morphometrische Hypothese” gilt. Jedoch präsentieren wir die Ergebnisse einer umfangreichen numerischen Studie, im Rahmen derer wir auf keinen Widerspruch gestoßen sind. Dies gilt freilich nur, solange die Voraussetzung erfüllt ist, dass das System  $S$  groß ist im Vergleich zu typischen Längenskalen der Flüssigkeit. Eine Vielzahl der abgeleiteten Ergebnisse werden mit hoher Genauigkeit bestätigt. Dazu präsentieren wir zunächst ein numerisches Schema, um die thermodynamischen Koeffizienten in Gl (1) zu berechnen. Mit diesem demonstrieren wir dann, dass Exzessadsorption  $\Gamma$ , Grenzflächenspannung  $\gamma$  und mittlere Kontaktdichte  $\bar{\rho}^c$  an Zylindern und Kugeln mit unterschiedlichen Radien sehr genau vorhergesagt werden können. Somit erweisen sich DFT Resultate konsistent mit dem morphometrischen Ansatz. Neben numerischen Rechnungen kann mit einer Bulktheorie bei speziellen Dichtefunktionalen näherungsweise die morphometrische Form für das großkanonische Potential  $\Omega$  abgeleitet werden. Wir heben jedoch hervor, dass die Bulktheorie genähert ist und dass die Aussage, DFT und die morphometrische



Hypothese seien kompatibel, weder trivial ist, noch durch die Verwendung von FMT-basierten Dichtefunktionalen impliziert wird.

Der enorme Vorteil der morphometrischen Formen besteht darin, dass diese auch bei komplex geformten Objekten eine einfache Berechnung von thermodynamischen Größen erlauben. Wir demonstrieren anhand von drei Monte-Carlo Simulationen von harten Kugeln um Ellipsoide bzw. einen Sphärozyylinder, dass die Vorhersagen unserer Theorie mit sehr hoher Genauigkeit auch an komplex geformten Objekten erfüllt sind. Es wird darauf hingewiesen, dass die thermodynamischen Größen über das System  $S$  *gemittelte* Größen sind und deshalb die morphometrische Hypothese dann von besonderem Interesse ist, wenn man sich nicht für die mikroskopischen Details einer Wand-Flüssigkeit Grenzfläche interessiert. Als Näherung lassen sich die morphometrischen Formen jedoch auch lokal verwenden, wenn der Einfluss der lateralen Krümmungsabhängigkeit vernachlässigbar ist.

Die morphometrische Form ist nicht auf die Anwendung auf rein konvexe Geometrien  $S$  beschränkt. Die Ergebnisse lassen sich durch die Verwendung von negativen Krümmungen  $H$  und  $K$  auch für die Vorhersage thermodynamischer Größen in konkaven Systemen nutzen. In diesem Zusammenhang muss beachtet werden, dass  $S$  groß gegen die Flüssigkeitsteilchen ist, um kaustische Effekte auszuschließen. Wir quantifizieren diese mithilfe von DFT-Rechnungen einer Hartkugelflüssigkeit in einer zylindrischen Kavität und bestätigen, dass für hinreichend große Zylinderradien die morphometrische Form auf Basis von Daten an konvexen Wänden eine exzellente Vorhersage auch für konkave Geometrien liefert.

Betrachtet man Flüssigkeiten an weichen Wänden, so bleiben die Aussagen der morphometrischen Hypothese weiterhin gültig, man muss jedoch beachten, dass die Kontaktdichte dann keine thermodynamische Größe mehr ist. Das hat zur Konsequenz, dass neben linearen Krümmungstermen noch höhere Potenzen in  $H$  und  $K$  benötigt werden, um den vollständigen Einfluss der Geometrie auf  $\bar{\rho}^c$  zu beschreiben. Diese Beobachtung steht im Gegensatz zu der bei Exzessadsorption und Grenzflächenspannung, welche trotz weicher Wände ihre morphometrische Form beibehalten.

Für eine Square-Well-Flüssigkeit mit weicher Teilchen-Teilchen-Wechselwirkung beobachten wir auch eine morphometrische Form für thermodynamische Größen, solange es nicht zu Effekten wie Drying kommt. Das führt, wie Evans *et. al.* in [53] zeigen, zu einer nichtanalytischen Abhängigkeit der thermodynamischen Größen

von der Geometrie. Wie beobachten diesen Effekt indirekt durch eine Verletzung der morphometrischen Form.

**Kapitel 4.** Mit morphometrischen Formen lassen sich thermodynamische Größen sehr genau berechnen. Dabei handelt es sich jedoch stets um gemittelte bzw. globale Größen. Diese können nicht die mikroskopischen Details einer Wand-Flüssigkeit Grenzfläche beschreiben. Darunter verstehen wir insbesondere strukturelle Eigenschaften wie die Verteilung der Dichte von Flüssigkeitsteilchen. Mit deren Hilfe werden wir, in einem weiteren Schritt, im folgenden Kapitel effektive Wechselwirkungspotentiale zwischen komplex geformten Körpern berechnen. Um die Geometrieabhängigkeit der Dichte  $\rho(\mathbf{r})$  am Ort  $\mathbf{r}$  zu beschreiben, führen wir Normalkoordinaten ein. Aufbauend auf den Ergebnissen des vorherigen Kapitels benutzen wir als Ansatz für  $\rho(\mathbf{r})$  eine analytische Entwicklung in Potenzen der Krümmungen  $H$  und  $K$

$$\begin{aligned} \rho(\mathbf{r}) = & \rho_P(u) + \rho_H(u)H + \rho_K(u)K + \rho_{H^2}(u)H^2 + \\ & + \rho_{H^3}(u)H^3 + \rho_{HK}(u)HK + \mathcal{O}(R_{1,2}^{-4}). \end{aligned} \quad (2)$$

Hier bezeichnen  $u$  den Normalabstand,  $\rho_P(u)$  das Dichteprofil an einer ebenen Wand und  $\rho_\xi(u)$  für  $\xi = H, K, H^2, HK, H^3, \dots$  die Krümmungsentwicklungskoeffizientenfunktionen. Um diesen Ansatz zu testen betrachten wir eine Hartkugelflüssigkeit und bestimmen die Koeffizientenfunktionen durch die Analyse von Dichteprofilen in einfachen Geometrien. Da es aus praktischen Gründen kaum möglich ist, DFT auf komplex geformte Objekte anzuwenden, nutzen wir Monte-Carlo Simulationen um die Verteilung von harten Kugeln um ein biaxiales hartes Ellipsoid zu bestimmen. Die Ergebnisse stimmen ausgezeichnet mit denen der Krümmungsentwicklung überein, wobei beachtet werden muss, dass Gl. (2) nur den Einfluss der lokalen Krümmungen auf die Dichte betrachtet. Die Geometrie der Wand muss also so beschaffen sein, dass der Einfluss von lateralen Variationen von  $H$  und  $K$  vernachlässigbar ist.

Die Krümmungsentwicklung eines Dichteprofiles und die morphometrische Form thermodynamischer Größen sind eng miteinander verknüpft. Erstere stellt eine weit allgemeinere Form der Krümmungsabhängigkeit als eine morphometrische Form dar. Deshalb müssen die Krümmungsentwicklungskoeffizientenfunktionen  $\rho_\xi(u)$  Summenregeln erfüllen. Ein naheliegender Zusammenhang ist  $\rho^c = \rho(u = 0)$ , d.h. die Kontaktdichte ist die Dichte mit verschwindendem Normalabstand von der Wand. Da wir im vorangehenden Kapitel zeigen, dass nichtmorphometrische Terme für  $\bar{\rho}^c$  an der harten Wand verschwinden, muss folglich  $\rho_\xi(u = 0) = 0$  für alle  $\xi = H^2, HK, H^3, \dots$  gelten.

Das beobachten wir numerisch mit hoher Genauigkeit sowohl für verschiedene Modelle als auch Packungsdichten. Weitere Zusammenhänge zwischen der Exzessadsorption  $\Gamma$  und dem Dichteprofil werden abgeleitet und numerisch verifiziert. Besonders bemerkenswert sind die Implikationen des Harte-Wand-Theorems in Verbindung mit dem Gibbs-Adsorptions-Theorem. Es verbindet die Kontaktdichte mit der Exzessadsorption, also dem Integral über die Dichte. Nimmt man eine analytische Entwicklung des Dichteprofiles an, so folgt daraus ohne weitere Annahmen, dass  $\rho_{H^2}(0) = 0$  für alle Flüssigkeiten, chemischen Potentiale und Temperaturen. Eine weitere Beziehung schränkt die Krümmungsabhängigkeit der Kontaktdichte speziell an harten Kugeln ein. Weitere Resultate sind zwar notwendig für die morphometrische Form des großkanonischen Potentials, jedoch nicht hinreichend.

Verblüffenderweise kann die funktionale Form der Krümmungsentwicklungskoeffizientenfunktionen  $\rho_\xi(u)$  und somit auch der Dichte  $\rho(\mathbf{r})$  an einer beliebig geformten Wand für hinreichend große Normalenabstände  $u$  analytisch berechnet werden. Dazu untersuchen wir die totale Korrelationsfunktion  $h_{wp}(\mathbf{r})$  zwischen der Wand und den Teilchen unter Verwendung der Ornstein-Zernike-Gleichung. Wir nehmen an, dass die Flüssigkeit eine isotrope Bulkphase hat, dass also keine spontane Symmetriebrechung auftritt und dass desweiteren die Wand-Teilchen- und Teilchen-Teilchen-Wechselwirkung kurzreichweitig sind. Für große Abstände von der Wand lässt sich dann eine Differentialgleichung ableiten, die die totale Wand-Teilchen-Korrelationsfunktion  $h_{wp}(u)$  erfüllen muss. Diese lässt sich näherungsweise integrieren

$$h_{wp}(u) = \frac{A \exp(-i\Im(k_0)u) \sin(\Re(k_0)u + \theta)}{\sqrt{1 + 2Hu + Ku^2}}. \quad (3)$$

Dabei sind  $k_0$  die (komplexe) Position des Pols führender Ordnung und  $A$  und  $\theta$  unbekannte Amplituden und Phasen, die nicht mehr vom Normalabstand  $u$  abhängen. Numerisch zeigt sich, dass diese nur sehr schwach von  $H$  und  $K$  abhängen, so dass die asymptotische Form der Korrelationsfunktion  $h_{wp}(u)$  vollständig definiert ist. Es lassen sich nun Dichteprofile und Krümmungsentwicklungskoeffizientenfunktionen  $\rho_\xi(u)$  bestimmen. Wir bestätigen eine ausgezeichnete Übereinstimmung mit numerischen Daten.

**Kapitel 5.** Kennt man die Dichteverteilung von Flüssigkeitsteilchen um einen Körper, kann man mit der sog. Einfügemethode effektive Wechselwirkungen zwischen eben diesem und einem weiteren Körper berechnen. Diese Methode wurde erfolgreich für einfach geformte Objekte getestet. In einem solchen Fall ist es nämlich möglich,

herkömmliche DFT Verfahren zu verwenden, um die Dichteprofile um einen der Körper zu bestimmen. Dies wird jedoch praktisch unmöglich, sobald beide Körper keine hochsymmetrische Form mehr haben. Für ein biologisches Schlüssel-Schloss-System, das wir hier näher studieren, ist das jedoch gerade wesentlich. Wir entwickeln deshalb eine Methode, die solches leistet.

Wir beginnen dazu unsere Betrachtungen mit der effektiven Wechselwirkung zwischen einer Kugel und einem Ellipsoid. Nach der Einfügemethode gibt es dann zwei unterschiedliche Wege, das effektive Wechselwirkungspotential zu berechnen. In einem Fall beginnt man mit der Kugel und fixiert diese im Ursprung. Man errechnet das Dichteprofil der Flüssigkeitsteilchen und fügt dann das Ellipsoid ein. Letzteres geschieht mithilfe der FMT für asphärische Teilchen, was einen kleinen systematischen Fehler mit sich bringt. Der alternative Weg besteht darin, mit dem Ellipsoid zu beginnen, dieses zu fixieren und das Dichteprofil unter Verwendung der Krümmungsentwicklung zu bestimmen. Dann kann man die Kugel einfügen und erhält so alternativ zum ersten Weg das effektive Wechselwirkungspotential. Für den zweiten Weg kann man die FMT für Kugeln verwenden, jedoch erwartet man auch hier einen kleinen Fehler, da die Krümmungsentwicklung nicht exakt ist. Der entscheidende Punkt ist, dass beide Wege jeweils unabhängige systematische Fehler bei der Berechnung des Wechselwirkungspotentials liefern. Da aber beide Alternativen aus physikalischen Überlegungen heraus ein identisches Resultat liefern müssen, kann man die Abweichung beider Ergebnisse voneinander als ein Maß für die Genauigkeit beider Verfahren nutzen. Wir finden eine sehr gute Übereinstimmung, solange die lateralen Variationen der lokalen Krümmungen  $H$  und  $K$  klein sind. Der Grund ist, analog zu den Beobachtungen bei dem Dichteprofil, dass die Krümmungsentwicklung nur lokale Krümmungen betrachtet.

Mit dem Wissen, dass sowohl die Krümmungsentwicklung als auch die FMT für asphärische Teilchen sehr gute Näherungen sind, können beide Methoden kombiniert verwenden, um effektive Wechselwirkungen zwischen zwei komplex geformten Objekten zu bestimmen. Wir studieren aus der Fülle von möglichen Systemen zwei Ellipsoide und zeigen ausgewählte Ergebnisse für verschiedene relative Lagen. Da die Wechselwirkung zwischen diesen beiden Objekten neben der Lage auch von der gegenseitigen Orientierung abhängt, entstehen für solche Systeme neben den effektiven Kräften auch entropische Drehmomente, welche ebenfalls durch unseren Ansatz berechnet werden können und präsentiert werden.

Um den Einfluss der effektiven Wechselwirkungskräfte auf ein Schlüssel-Schloss-System zu studieren, schlagen wir ein einfaches Modell vor. Es besteht aus einem ellipsoidalen Schlüssel und einem Schloss mit einem ellipsenförmigen Hohlraum, in den das Schlüsselteilchen passt. Beide Objekte sind von einer Hartkugelflüssigkeit umgeben. Der entscheidende Unterschied zu den vorherigen Systemen besteht in der Tatsache, dass es sich bei dem Schlüssel um ein teilweise konkaves Objekt handelt, so dass in der Krümmungsentwicklung negative  $H$  und  $K$  auftreten. Wir haben bereits für den Kontaktwert der Dichte gezeigt, dass sich Ergebnisse von konvexen auch auf konkave Geometrien verallgemeinern lassen und erwarten deshalb auch in diesem Fall sehr genaue Vorhersagen der Krümmungsentwicklung.

In Ref. [97] präsentiert Kinoshita effektive Wechselwirkungspotentiale zwischen einem *kugelförmigen* Schlüssel und einem Schloss mit einem entsprechend halbkugelförmigen Hohlraum. Diese Berechnungen beruhen auf der numerischen Lösung von genäherten Integralgleichungen auf einem dreidimensionalen Gitter. Wir wiederholen die Rechnungen mit unserem Ansatz, wobei zu beachten ist, dass wir die verwendete Geometrie leicht modifizieren. Dazu ist es erforderlich, die Kanten am Schlüsselobjekt abzurunden, um so die Krümmungsentwicklung anwenden zu können. Demnach sind beide Geometrien nicht völlig identisch, jedoch stimmen wichtige Beobachtungen qualitativ überein. Das resultierende effektive Wechselwirkungspotential ist stets sehr negativ, wenn sich Schlüssel und Schloss berühren, d.h. die Anwesenheit von weiteren Teilchen führt dazu, dass der gebundene Zustand energetisch stark begünstigt wird. Wir beobachten, dass geometrisch kompatible Schlüssel und Schlösser eine besonders hohe stabilisierende freie Energie für den gebundenen Zustand haben, was vor dem Hintergrund der hohen Selektivität der enzymatischen Reaktion besonders interessant ist. Diese Beobachtung ist verständlich durch ein Argument der Asakura-Oosawa Näherung. Es besagt, dass die stabilisierende freie Energie proportional zum Überlappungsbereich der für die umgebenden Teilchen ausgeschlossen Volumina ist, welches konsequenterweise am größten ist, wenn Schlüssel und Schloss kompatible Formen haben. Ein sehr wichtiger Aspekt wird jedoch nur von aufwändigeren Theorien vorhergesagt, nämlich dass das Annähern von dem Schlüssel zum Schloss von einer energetischen Barriere begleitet wird. Die Höhe überschreitet für große Schlüssel-moleküle die thermische Anregungsenergie bei weitem, so dass zwar der gebundene Zustand nach wie vor energetisch begünstigt ist, jedoch praktisch nie erreicht wird. Mit kugelförmigen Schlüsseln gibt es keine Möglichkeit, die Barriere zu umgehen.

Wir erweitern deshalb unser Modell und betrachten nun einen ellipsoidalen, also asphärischen Schlüssel mit entsprechend kompatibelem Schloss. Führt man den Ellipsoid wie gewohnt mit fester Orientierung in das Schloss, so tritt auch in diesem Fall wieder eine energetische Barriere und ein stark negativer Kontaktwert auf. Allerdings sind nun die Winkelfreiheitsgrade des Schlüssels nicht mehr energetisch entartet. Wir zeigen, dass die Annäherung von einem gedrehten Schlüssel­molekül zwar das effektive Wechselwirkungspotential quantitativ verändert, jedoch kann in allen Fällen eine Energiebarriere beobachtet werden. Desweiteren ist für einen gedrehten Schlüssel keine vollständige Annäherung an das Schloss mehr möglich. Um das zu umgehen betrachten wir außerdem die Annäherung des Schlüssel­moleküls unter der Annahme, dass es sich stets nach dem lokalen entropischen Drehmoment ausrichtet. Es nutzt also für alle Positionen seine Winkelfreiheitsgrade, um das effektive Wechselwirkungspotential zu minimieren. Mit dieser Annahme erhalten wir einen nahezu monotonen Verlauf des Wechselwirkungspotentials bei Annäherung, d.h. ein asphärischer Schlüssel kann in das Schloss finden, indem er stets den lokalen Kräften und Drehmomenten folgt. Wir weisen darauf hin, dass einer solchen Interpretation die Annahme zugrunde liegt, dass sich das Gesamtsystem zu jedem Zeitpunkt im thermischen Gleichgewicht befindet, was nur genähert der Fall ist. Weiterhin ist unser Modell idealisiert, da keine nur Hartkörperwechselwirkungen betrachtet werden. Jedoch erlauben diese rein entropischen effektiven Wechselwirkungspotentiale einen Mechanismus, der einige wesentliche Aspekte in einem Schlüssel-Schloss-System erklärt.

# Abstract

In a cell biochemical reactions are controlled by the use of enzymes, which catalyze reactions by providing a binding site where other molecules can react with a highly decreased activation energy. This means that enzymes increase the reaction rate of a biochemical process. In order to use them to selectively control a certain reaction it is necessary that they are specific, i.e. they should only promote a unique biochemical reaction. This is observed experimentally and this finding is normally explained by a key-lock picture, which describes the enzyme as a “lock” and the reacting molecule as a “key”. Only if the key fits into the lock it can be used to trigger a specific action.

Prior to the chemical reaction, the key-molecule must be moved to the lock for touching, which means that it must be positioned and oriented in a pre-defined way. This is not trivially achieved. If there is no interaction between key and lock molecule, the particles essentially exhibit a random walk - both concerning their positions and orientations. In such a system it is very unlikely that touching occurs, because the phase-space where the chemical reaction can be triggered is very small. Consequently, the reaction rate would be low and the enzyme very inefficient. This is not observed which means that for actual systems an interaction potential between key and lock is present.

There are various physical effects which can be used to explain intermolecular interaction potentials. Electric charges on the molecules lead to Coulomb forces, Van-der-Waals interactions are due to the coupling of dipoles, and hydrogen bonds arise between the partial charges of a hydrogen atom and a heteroatom. Common to these interactions is that they depend on the molecular structure of the molecules, i.e. they are chemically specific. Therefore, if these potentials are responsible for the interaction potential needed for a fast enzymatic reaction, all involved molecules must be designed in a way that the resulting interaction potential leads to a bonding between the key and the lock molecule. This constraint would limit the degrees of freedom for the design of biomolecules which is unlikely as this would be inefficient.

It is more likely that the source of attraction between key and lock is based on

a more fundamental, chemically unspecific mechanism. Effective interactions are a good candidate for the intermolecular forces in such a system [1, 2, 3]. In the past years they have been discussed to be essential for the understanding of many biological processes which are controlled by interactions between macromolecules [4, 5, 6]. The origin of effective interactions is that the key-lock system is immersed in a sea of other molecules. Such a situation is typical in a physiological environment, as a cell is a densely packed mixture of various particles. These “background” particles do not take part in the actual reaction of key and lock, they however undergo thermal motion and interact physically with the key, the lock, and among each other. The interaction leads to a momentum transfer on key and lock, also referred to as osmotic pressure. It is balanced, if both particles are at a large mutual distance, i.e. the net effect of the momentum transfer vanishes. It however becomes unbalanced when both particles are close to each other because of correlations within the fluid. The net effect can be described by an effective interaction potential. According to a simple model, the Asakura and Oosawa approximation [7], the effective potential is minimal for touching, which means that such a configuration is thermodynamically favored. In the thermodynamic equilibrium it is therefore likely that the key and lock touch. This could explain the efficiency of key-lock reactions in particular as this simple approximation agrees qualitatively also with more elaborate theories. It however fails to predict other important features of the effective interactions as we describe in Section 5.4. There are potential barriers that must be overcome during the approach by the key-particle, which are not accounted for by the Asakura-Oosawa approximation. It furthermore yields a vanishing effective force as the long-distance behavior, which is an artifact of the assumptions made for the approximation.

In this thesis we develop a more elaborate technique to calculate effective interactions between asymmetric particles, which we use as a model for a key and lock system. It is however essential to understand that the reason for this work is *not* to model a specific key-lock system with a high accuracy. From a physical viewpoint it is rather interesting to study the influence of the depletion effects in such systems by employing models which on the one hand capture all relevant effects but on the other hand are sufficiently simple that the results can be interpreted and generalized to a larger class of different key-lock systems. One particular approximation we therefore choose is the use of purely hard objects, which means that the effective interactions is of purely entropic origin. In doing so we neglect all chemically specific forces mentioned above. These are of minor interest here, because we aim to study the influence of *effective* interactions on the biological key-lock system. Note that aside



from this pragmatic argument electric forces are also shielded on a short lengthscale at physiological salt ion concentrations. The macromolecules, which act as key and lock, are usually large compared to the range of electrical interactions such that we expect that the use of hard objects represents an adequate approximation. A further approximation is the use of a hard-sphere fluid to describe the background fluid of objects the key-lock system is immersed in.

One aspect which we find to be essential for these systems is the geometry of the key and the lock. A simple approximation of the key molecule as a sphere inevitably leads to energetic barriers which are very unlikely to be overcome by thermal energy. If however sufficiently asymmetric particles are considered, the potential barrier can be overcome by using the angular degrees of freedom of the key, as we report in Section 5.4. Unfortunately it is very complicated to calculate effective interactions between non-symmetric objects by means of direct methods. These normally require to perform calculations on a three-dimensional grid which makes the numerical evaluation very costly and inaccurate. Our approach is to systematically study the influence of an object with a complex shape on the surrounding fluid by treating the influence of the curvature perturbatively. This is done in three major steps, which we describe in Chapters 3, 4, and 5.

Before the actual presentation of these results, we give in Chapter 1 a brief overview concerning the different concepts used in this work. We review the models and approximations employed in various places of the thesis. In Chapter 2 we introduce thermodynamic quantities which are associated with a fluid in contact with a curved wall. These quantities, such as excess adsorption or interfacial tension are commonly used in the literature, such that here we particularly emphasize the subtleties that arise near a *curved* interface. This allows us in Chapter 3 to formulate a morphometric thermodynamics, which implies a simple dependence for thermodynamic quantities on the shape of an immersed particle. These results are generalized in Chapter 4 to predict also structural quantities, in particular density distributions of solute particles near curved walls. In a final step we calculate effective interactions in Chapter 5 and study the influence of these entropic interactions in the context of biological key-lock systems.

# Chapter 1

## Basic Concepts

In this chapter we provide a brief introduction into the various theoretical concepts that are used in this work. The general aim is not to provide a detailed review, which would be beyond the scope of a thesis, but to define important quantities, quote useful relations, and cite important references. In the first section, the basic ideas concerning density-functional theory (DFT) of simple fluids are summarized. Then, in the second section, we give a short introduction to the fundamental measure theory (FMT). This theory provides, within the framework of DFT, the state-of-the-art description for fluids with hard-core interactions. It is in particular successful to model a fluid that consists of hard *spherical* particles, the so-called hard-sphere fluid. This system serves as a “working horse” for many fundamental considerations and will be commonly used to numerically verify the results derived in this work. For some studies however, we use fluids which are not exclusively dominated by entropy. We review in section three a high temperature perturbation theory which allows us to extend models used for fluids with *pure* hard-core interactions to account also for colloids that feature in addition to a hard core also a soft interparticle interaction potential. One particular application of such a theory is the square-well fluid. Finally, in the fourth section, the idea of integrating out internal degrees of freedom is addressed. This leads to effective many-body interactions and a method is reviewed that, based on the FMT, allows to calculate effective interaction potentials. We apply this theory later in Chapter 5 to calculate the depletion interaction in a key-lock system.

## 1.1 Density-Functional Theory

Density-functional theory is based on the finding that all thermodynamic quantities of a statistical system can be expressed as functionals of the equilibrium single-particle density. This idea was originally formulated by Hohenberg, Kohn [8], and Mermin [9] for quantum systems but later this finding was generalized also to classical fluids [10]. It was in particular proven that for a statistical system with given interparticle interactions the equilibrium single-particle density  $\rho(\mathbf{r})$  can be used to *uniquely* calculate the external potential acting on the fluid particles in the system. With this knowledge, namely the external potential and the interparticle interaction, the full Hamiltonian of the statistical system is in principle known and thus a partition sum and all thermodynamic observables can be calculated. This shows that in essence all thermodynamic quantities can be regarded as *functionals* of the equilibrium single-particle density of the particles. The implications of this finding alone are however limited, as it does not provide a systematic way to calculate the actual equilibrium single-particle density  $\rho(\mathbf{r})$ . In order to obtain it, a functional  $\Omega[f]$  of the phase space density  $f(\mathbf{r}^N, \mathbf{p}^N; N)$  is constructed such that it has a global minimum for the *equilibrium* phase space density  $f_0(\mathbf{r}^N, \mathbf{p}^N; N)$ , i.e.  $\Omega[f] \geq \Omega[f_0]$  for all phase space densities  $f$ . To this end it is essential to realize that the equilibrium phase space density  $f_0(\mathbf{r}^N, \mathbf{p}^N; N)$  itself is also a functional of the equilibrium density distribution  $\rho(\mathbf{r})$  and therefore the constructed functional  $\Omega[f]$  with a minimum for  $f = f_0$  can also be interpreted as a functional  $\Omega[f[\rho]] = \Omega[\rho]$  of the single-particle density  $\rho(\mathbf{r})$ . This density functional also has, by construction, a global minimum for the equilibrium single-particle density. This special property allows one to use a variational principle to find the equilibrium density distribution  $\rho(\mathbf{r})$ . Once the distribution of the density  $\rho(\mathbf{r})$  is found, all other thermodynamic quantities can in principle be calculated as indicated above. Survey articles about DFT and a more detailed presentation of these concepts can be found in Refs. [10, 11, 12].

The actual functional mapping  $\Omega[\rho]$  is very complicated and can, for a general fluid, usually not be expressed in a closed form. To proceed, one normally splits the functional  $\Omega[\rho(\mathbf{r})]$  into the following three contributions

$$\Omega[\rho(\mathbf{r})] = \mathcal{F}_{id}[\rho(\mathbf{r})] + \mathcal{F}_{ex}[\rho(\mathbf{r})] + \int \rho(\mathbf{r})(V_{ext}(\mathbf{r}) - \mu) d\mathbf{r}. \quad (1.1)$$

$\mathcal{F}_{id}[\rho]$  is the functional of the intrinsic free energy of an ideal gas and  $\mathcal{F}_{ex}[\rho]$  denotes the excess free energy, where “excess” refers to the difference to the ideal contribution  $\mathcal{F}_{id}[\rho]$ . The third term in Eq. (1.1) describes the influence of the external potential

$V_{ext}(\mathbf{r})$  on the grand potential. It includes the chemical potential  $\mu$ , which is the conjugated quantity to the total number of particles. The first term of Eq. (1.1),  $\mathcal{F}_{id}[\rho]$ , is known in closed form

$$\beta\mathcal{F}_{id}[\rho(\mathbf{r})] = \int \rho(\mathbf{r})(\ln(\Lambda^3\rho(\mathbf{r})) - 1) d\mathbf{r}, \quad (1.2)$$

where  $\Lambda = \sqrt{2\pi\beta\hbar^2/m}$  stands for the thermal wavelength of the fluid particles with mass  $m$ .  $\beta = 1/(k_B T)$  is the inverse temperature. In order to avoid dimensional expression one normally substitutes  $\Lambda$  by the ideal chemical potential  $\beta\mu_{id} = \ln(\Lambda^3\rho_b)$ , where  $\rho_b$  denotes the bulk density of the fluid. Eq. (1.2) then becomes

$$\beta\mathcal{F}_{id}[\rho(\mathbf{r})] = \int \rho(\mathbf{r}) \left( \ln\left(\frac{\rho(\mathbf{r})}{\rho_b}\right) + \mu_{id} - 1 \right) d\mathbf{r}. \quad (1.3)$$

It should be noted that up to this point no approximation is made. Therefore the exact density functional  $\Omega[\rho]$  of an ideal gas is obtained by setting  $\mathcal{F}_{ex}[\rho] = 0$ . In case of a non-ideal fluid however, an expression for the functional  $\mathcal{F}_{ex}[\rho] \neq 0$  must be used to describe the correlation between the non-ideal fluid particles. This can usually only be done approximately and we address this issue in more detail in Section 1.2. Here we assume that  $\mathcal{F}_{ex}[\rho]$  and hence all terms in Eq. (1.1) are known for the fluid of interest. With a given  $\Omega[\rho]$ , the equilibrium density distribution is obtained and then, in a second step, other thermodynamic properties are derived. Note that an expression for  $\mathcal{F}_{ex}[\rho]$  is normally hard to find. However, once it is found for a certain type of fluid, it is *independent* of the external potential, such that the same expression  $\mathcal{F}_{ex}[\rho]$  can be re-used for all  $V_{ext}(\mathbf{r})$ . This property makes DFT a very powerful tool to study the influence of differently shaped walls, which enter the functional  $\Omega[\rho]$  as an external potential.

Suppose  $\mathcal{F}_{ex}[\rho]$  is known and therefore all three contributions in Eq. (1.1) for  $\Omega[\rho]$  are given. One then uses the fact that  $\Omega[\rho]$  is minimal for the equilibrium density profile  $\rho(\mathbf{r})$ . The density profile  $\rho(\mathbf{r})$  is hence found by the necessary condition  $\delta\Omega/\delta\rho(\mathbf{r}) = 0$ , which demands that  $\Omega[\rho]$  is stationary for the equilibrium density  $\rho(\mathbf{r})$ . In DFT, this condition is called the Euler-Lagrange equation and must be satisfied for all positions  $\mathbf{r}$  in space. Applying  $\delta\Omega/\delta\rho(\mathbf{r}) = 0$  to the expression in Eq. (1.1) and using Eq. (1.3) for  $\mathcal{F}_{id}[\rho]$  leads to

$$\rho(\mathbf{r}) = \rho_b \exp(c^{(1)}(\mathbf{r}) - \beta V_{ext}(\mathbf{r}) + \beta\mu_{id} - \beta\mu). \quad (1.4)$$

Here we introduce the one-particle direct correlation function  $c^{(1)}(\mathbf{r})$ , which is the

first function in a hierarchy of higher order direct correlation functions

$$c^{(n)}(\mathbf{r}_1, \dots, \mathbf{r}_n) = -\frac{\delta^n \beta \mathcal{F}_{ex}[\rho]}{\delta \rho(\mathbf{r}_1) \dots \delta \rho(\mathbf{r}_n)}. \quad (1.5)$$

All direct correlation functions  $c^{(n)}$ ,  $n = 1, 2, \dots$  are functionals of the density profile  $\rho(\mathbf{r})$  and in general very complicated functions that depend on multiple positions  $\mathbf{r}_1, \dots, \mathbf{r}_n$  in space. They however simplify significantly in the bulk, i.e. under the assumption of a constant density profile  $\rho(\mathbf{r}) = \rho_b$ . In particular the one-particle direct correlation function  $c^{(1)}(\mathbf{r})$  becomes a constant which is referred to as the excess chemical potential  $\beta \mu_{ex} = -c^{(1)}(\mathbf{r}_1)|_b = \mu - \mu_{id}$ . With this definition, Eq. (1.4) can be written as

$$\rho(\mathbf{r}) = \rho_b \exp(c^{(1)}(\mathbf{r}) - \beta V_{ext}(\mathbf{r}) - \beta \mu_{ex}). \quad (1.6)$$

Note that Eq. (1.6) represents only a formal solution of the Euler-Lagrange equations  $\delta \Omega / \delta \rho(\mathbf{r}) = 0$ , as  $c^{(1)}(\mathbf{r})$  on the right hand side is in general a functional of the density profile  $\rho(\mathbf{r})$  itself, as indicated above. Therefore both sides of Eq. (1.6) depend on  $\rho(\mathbf{r})$ . The equation can however be solved iteratively by guessing an initial density profile. Based on this profile we obtain in a first step  $c^{(1)}(\mathbf{r})$  using Eq. (1.5) and then, in a second step, a new guess for  $\rho(\mathbf{r})$  using Eq. (1.6). Usually the new guess is closer to the actual equilibrium density profile such that this scheme converges after multiple iterations.

## 1.2 Fundamental-Measure Theory

The construction of a practical expression for  $\mathcal{F}_{ex}[\rho]$  in Eq. (1.1) is usually complicated. Although an exact expression for this functional is in principle known from a systematic expansion in terms of single-particle density clusters [13], such an expansion is not practicable to be used numerically. It contains a slowly converging, infinite series of multiple convolutions of the density  $\rho(\mathbf{r})$ , which are very costly when calculated numerically. Modern functionals  $\mathcal{F}_{ex}[\rho]$  therefore sacrifice the exactness of the cluster expansions for the sake of more practical expressions. When considering fluids of hard convex particle, a very powerful and successful framework for approximate functionals is provided by the fundamental measure theory (FMT) [14, 15]. This theory makes an approximation concerning the functional form of  $\mathcal{F}_{ex}[\rho]$ , but still allows further theories to improve the density functional in order to model the behavior of the respective fluid as close as possible. For reasons of clarity we review the FMT for a monodisperse fluid of hard spheres with radius  $R$ , although this theory

was developed originally for a fluid mixture of spheres. More recent generalizations include a treatment of components which consist of nonspherical hard particles. We review them at the end of this section.

If the center of one sphere  $i$  is at position  $\mathbf{r}_i$  and the center of another sphere  $j \neq i$  is at  $\mathbf{r}_j$ , the pair interaction potential can be written in the following form

$$V(\mathbf{r}_i, \mathbf{r}_j) = \begin{cases} \infty & \text{if } |\mathbf{r}_i - \mathbf{r}_j| \leq 2R, \\ 0 & \text{otherwise,} \end{cases} \quad (1.7)$$

where  $R$  denotes the radius of the spheres. Sometimes it is more convenient to rewrite this equation using the so-called Mayer- $f$  bond  $f(\mathbf{r}_i, \mathbf{r}_j) = \exp(-\beta V(\mathbf{r}_i, \mathbf{r}_j)) - 1$  [13], which for a fluid of hard spheres has the form

$$f(\mathbf{r}_i - \mathbf{r}_j) = -\Theta(|\mathbf{r}_i - \mathbf{r}_j| - 2R), \quad (1.8)$$

where  $\Theta$  denotes the usual Heaviside unit step function. In order to describe particles that interact via this potential using DFT methods, a functional expression for the excess free energy  $\mathcal{F}_{ex}[\rho]$  is needed. From the cluster expansion [13] it is known that  $\mathcal{F}_{ex}[\rho]$  can be written to lowest order term in the density  $\rho$  in the following form

$$\lim_{\rho \rightarrow 0} \beta \mathcal{F}_{ex}[\rho] = -\frac{1}{2} \int d\mathbf{r}_i d\mathbf{r}_j \rho(\mathbf{r}_i) \rho(\mathbf{r}_j) f(\mathbf{r}_i - \mathbf{r}_j). \quad (1.9)$$

One way to proceed was developed by Rosenfeld [15, 16, 17] and is motivated by the findings in Percus-Yevick theory [18]. The idea is to decompose the Mayer- $f$  bond used in Eq. (1.9) into convolutions of the geometries of the two spheres. This is for example achieved by

$$\begin{aligned} \Theta(|\mathbf{r}_i - \mathbf{r}_j| - 2R) &= \omega^{(3)}(\mathbf{r}_i) \otimes \omega^{(0)}(\mathbf{r}_j) + \omega^{(0)}(\mathbf{r}_i) \otimes \omega^{(3)}(\mathbf{r}_j) + \omega^{(2)}(\mathbf{r}_i) \otimes \omega^{(1)}(\mathbf{r}_j) \\ &\quad + \omega^{(1)}(\mathbf{r}_i) \otimes \omega^{(2)}(\mathbf{r}_j) - \omega^{(1)}(\mathbf{r}_i) \otimes \omega^{(2)}(\mathbf{r}_j) - \omega^{(2)}(\mathbf{r}_i) \otimes \omega^{(1)}(\mathbf{r}_j), \end{aligned} \quad (1.10)$$

where  $\omega^{(\alpha)}(\mathbf{r})$  for  $\alpha = 0, 1, 2, 3, \mathbf{1}, \mathbf{2}$  are the geometries or fundamental measures of a sphere with radius  $R$ . Note that this decomposition is not unique, but the resulting functionals based on different decompositions are equivalent [19]. The geometries of the spheres have the following form

$$\begin{aligned} 4\pi R^2 w^{(0)}(\mathbf{r}) &= 4\pi R w^{(1)}(\mathbf{r}) = w^{(2)}(\mathbf{r}) &= \delta(R - |\mathbf{r}|), \\ w^{(3)}(\mathbf{r}) &= \Theta(R - |\mathbf{r}|), & (1.11) \\ 4\pi R w^{(1)}(\mathbf{r}) &= w^{(2)}(\mathbf{r}) &= \frac{\mathbf{r}}{|\mathbf{r}|} \delta(R - |\mathbf{r}|). \end{aligned}$$

The symbol  $\otimes$  in Eq. (1.10) denotes a convolution between two fields  $f(\mathbf{r})$  and  $g(\mathbf{r})$

$$f(\mathbf{r}_i) \otimes g(\mathbf{r}_j) = \int d\mathbf{x} f(\mathbf{x} - \mathbf{r}_i)g(\mathbf{x} - \mathbf{r}_j). \quad (1.12)$$

Note that this definition implies a scalar product if  $f(\mathbf{r})$  and  $g(\mathbf{r})$  are vector-valued weight functions. Inserting Eq. (1.10) in Eq. (1.9) yields expressions where the density profile  $\rho(\mathbf{r})$  is convolved with the fundamental measures  $\omega^{(\alpha)}(\mathbf{r})$ . These expressions, which are referred to as weighted densities  $n_\alpha(\mathbf{r})$ , have the form

$$n_\alpha(\mathbf{r}) = \int d\mathbf{r}' \rho(\mathbf{r}')\omega^{(\alpha)}(\mathbf{r} - \mathbf{r}'). \quad (1.13)$$

With  $n_\alpha(\mathbf{r})$  as an abbreviation for the convolution integrals, the excess free energy functional  $\mathcal{F}_{ex}[\rho]$  can, to lowest order in the density, be rewritten as follows

$$\mathcal{F}_{ex}[\rho] = \int d\mathbf{r} \phi(\{n(\mathbf{r})\}). \quad (1.14)$$

The *function* (not functional)  $\phi(\{n(\mathbf{r})\})$  of all weighted densities  $n_\alpha(\mathbf{r})$  is explicitly known in lowest order in the density  $\rho$  by virtue of Eq. (1.9) with Eqs. 1.8 and 1.10. FMT however assumes that this functional form is approximately also true for all higher orders in the density. With this assumption also the full density functional, comprising all orders in the density  $\rho$ , has a functional form as indicated in Eq. (1.14). Although this is necessarily an approximation to the exact expression of  $\mathcal{F}_{ex}[\rho]$ , practice tells that with an appropriate  $\phi(\{n(\mathbf{r})\})$  the properties of the hard-sphere fluid can be modeled very accurately. There are several approaches that yield different expressions for the function  $\phi(\{n(\mathbf{r})\})$ . In the original version of FMT [15], an ansatz was chosen based on dimensional arguments and then the scaled particle differential equation [20, 21, 22, 14] was used to determine the unknown functions used for the ansatz. This idea leads to the following excess free energy density  $\phi(\{n(\mathbf{r})\})$

$$\beta\phi = -n_0 \ln(1 - n_3) + \frac{n_1 n_2 - n_1 \cdot n_2}{1 - n_3} + \frac{n_2^3 - 3n_2 (n_2 \cdot n_2)}{24\pi(1 - n_3)^2}. \quad (1.15)$$

This expression is referred to as the Rosenfeld functional which models various aspects of the hard-sphere fluid accurately. One interesting aspect is for example the pressure  $p$  of a hard-sphere fluid which we obtain within FMT via

$$\beta p = n_0 - \phi + \sum_{\alpha} n_{\alpha} \frac{d\phi}{dn_{\alpha}}. \quad (1.16)$$

For the Rosenfeld functional, Eq. (1.15), the pressure  $p$  is given by the Percus-Yevick (PY) Equation of State (EoS) [23]

$$\beta p = \rho_b \frac{1 + \eta + \eta^2}{(1 - \eta)^3}, \quad (1.17)$$

where  $\eta = 4\pi\rho_b/3$  is the bulk packing fraction. This EoS for hard spheres is in relatively good agreement to the actual one, which can be determined either numerically by simulations [24] or by experiments [25, 26, 27]. There are however limitations to the original Rosenfeld functional. It was shown that the actual fluid of hard spheres freezes for  $\eta > 0.494$  [28, 29, 30, 12], which is not accounted for by the expression in Eq. (1.15). For this reason the functional was modified later [31, 32, 33, 34], however in this thesis we are particularly interested in the fluid state and therefore exclusively use the original version of the functional. Another ansatz to construct a function  $\phi(\{n(\mathbf{r})\})$  is to modify the Rosenfeld functional such that the pressure  $p$  obtained from the density functional via Eq. (1.16) is closer to the actual EoS. A particularly successful parameterization of the EoS of a hard-sphere fluid is given by the Mansoori-Carnahan-Starling-Leland (MCSL) EoS [35], which reads for a monodisperse fluid [36]

$$\beta p = \rho_b \frac{1 + \eta + \eta^2 - \eta^3}{(1 - \eta)^3}. \quad (1.18)$$

One can enforce this EoS by an appropriate function  $\phi(\{n(\mathbf{r})\})$  that yields a pressure according to Eq. (1.18) when inserted in Eq. (1.16). Such a function  $\phi$  defines the White-Bear version of FMT [37, 38] and reads

$$\begin{aligned} \beta\phi = & -n_0 \ln(1 - n_3) + \frac{n_1 n_2 - \mathbf{n}_1 \cdot \mathbf{n}_2}{1 - n_3} + \\ & + (n_2^3 - 3n_2 (\mathbf{n}_2 \cdot \mathbf{n}_2)) \frac{n_3 + (1 - n_3)^2 \ln(1 - n_3)}{36\pi n_3^2 (1 - n_3)^2}. \end{aligned} \quad (1.19)$$

The latter functional shows an excellent agreement with simulation data not only concerning the equation of state, which is by construction given by Eq. (1.18), but also concerning other thermodynamic quantities and structural properties of the hard-sphere fluid like, e.g. density profiles or correlation functions. We will use it successfully in Section 3.3 to predict results of quasi-exact Monte-Carlo simulations.

The main advantage when using FMT-based functionals is the fact that the results found for a monodisperse fluid can easily be extended to fluid mixtures. Such an extension leaves  $\phi(\{n(\mathbf{r})\})$  unaltered, but leads to an extended definition of the weighted densities  $n_\alpha(\mathbf{r})$ , which add up for each component of the fluid

$$n_\alpha(\mathbf{r}) = \sum_i \int \rho_i(\mathbf{r}') w_i^{(\alpha)}(\mathbf{r} - \mathbf{r}') d\mathbf{r}'. \quad (1.20)$$



Here,  $\alpha$  labels the respective fundamental measure and  $i$  the different components of the fluid mixture. Note that the weight functions  $w_i^{(\alpha)}(\mathbf{r})$  depend on the different radii of the particles of each component  $i$ . For each hard-sphere component with radius  $R_i = R$  their functional form is given by Eq. (1.11). If a component consists of hard, but nonspherical convex particles, yet another extension of FMT is possible as described in Ref. [39]. The generalization to nonspherical particles follows closely the ideas for spheres and again aims to decompose the Mayer- $f$  bond into fundamental measures of the particles. The expression has a similar form as in Eq. (1.10), however the fundamental measures for an arbitrary convex object are more complicated as the ones provided by Eq. (1.11)

$$\begin{aligned}
w^{(0)}(\mathbf{r}) &= \frac{K(\mathbf{r})}{4\pi} \delta(R(\mathbf{r}) - |\mathbf{r}|), \\
w^{(1)}(\mathbf{r}) &= \frac{H(\mathbf{r})}{4\pi} \delta(R(\mathbf{r}) - |\mathbf{r}|), \\
w^{(2)}(\mathbf{r}) &= \delta(R(\mathbf{r}) - |\mathbf{r}|), \\
w^{(3)}(\mathbf{r}) &= \Theta(R(\mathbf{r}) - |\mathbf{r}|), \\
w^{(4)}(\mathbf{r}) &= \frac{H(\mathbf{r})}{4\pi} \frac{\mathbf{r}}{|\mathbf{r}|} \delta(R(\mathbf{r}) - |\mathbf{r}|), \\
w^{(5)}(\mathbf{r}) &= \frac{\mathbf{r}}{|\mathbf{r}|} \delta(R(\mathbf{r}) - |\mathbf{r}|).
\end{aligned} \tag{1.21}$$

$R(\mathbf{r})$  denotes the extend of the particle in  $\mathbf{r}$  direction.  $H(\mathbf{r})$  and  $K(\mathbf{r})$  are the mean and Gaussian curvatures of the particle and are only used together with a delta-distribution  $\delta$  which restricts  $\mathbf{r}$  to the surface of the particle. They can be calculated using the definitions derived in Eq. (A.8). It is interesting to note that both for spherical and nonspherical particles only four scalar and two vectorial weight functions are sufficient to model the interactions between variously shaped objects. This observation will become important in Section 3.3.1 where we review a bulk theory that is based on this very specific functional form of FMT based functionals. Note that for nonspherical objects the decomposition of the Mayer- $f$  bond as used in FMT is approximate.

### 1.3 High Temperature Expansion Theory

The well-established functionals for fluids with pure hard-core interactions can be extended by means of a perturbation theory to account also for pair interaction potentials that have in addition to a hard-core also a small, but non-zero soft interaction

for larger particle separations

$$V(\mathbf{r}_i, \mathbf{r}_j) = \begin{cases} \infty & \text{if } |\mathbf{r}_i - \mathbf{r}_j| \leq 2R, \\ V_{soft}(\mathbf{r}_i - \mathbf{r}_j) & \text{otherwise.} \end{cases} \quad (1.22)$$

In order to apply the perturbation theory,  $\beta V_{soft}(\mathbf{r})$  must be sufficiently small, which is in particular the case for high temperatures. Then the excess free energy density functional  $\mathcal{F}_{ex}[\rho]$  is then approximately given by

$$\mathcal{F}_{ex}[\rho] = \mathcal{F}_{ex}^{HS}[\rho] + \int d\mathbf{r} d\mathbf{r}' \rho(\mathbf{r}) \rho(\mathbf{r}') V_{soft}(\mathbf{r} - \mathbf{r}'), \quad (1.23)$$

where  $\mathcal{F}_{ex}^{HS}[\rho]$  denotes the excess free energy of the pure hard-core fluid and the second term the perturbation contribution. The ansatz for  $\mathcal{F}_{ex}[\rho]$  in Eq. (1.23) is relatively simple and there exist more elaborate methods to treat fluids in the high temperature limit. It is however capable of qualitatively describing phenomena like phase separations, wetting, or drying [40]. We use it in this thesis to describe a square-well fluid, which has the following perturbation potential

$$\beta V_{soft}(\mathbf{r} - \mathbf{r}') = \begin{cases} \beta\epsilon & \text{if } |\mathbf{r} - \mathbf{r}'| < R + R_\epsilon, \\ 0 & \text{otherwise,} \end{cases} \quad (1.24)$$

where  $R$  is the hard core radius.  $R_\epsilon$  denotes the width and  $\beta\epsilon$  the depth of the sort-ranged interaction. If the mutual attraction between the spherical particles is large enough, which means that  $\beta\epsilon$  is sufficiently negative for fixed  $R_\epsilon$ , a phase separation occurs, as displayed in the phase diagram in Fig. 1.1.

## 1.4 Effective Potentials

In order to describe the behavior of one or more big particles immersed in a sea of small particles it is often favorable to trace out the internal degrees of freedom of the smaller particles. This averaging over the phase-space of the small particles leads to an effective picture of the system. It consists only of the big particles that interact via effective many-body potentials. The one-body potential for instance equals the difference in the grand potential before and after the insertion of a single big particle in the bulk fluid of the smaller particles. When additionally a second big particle is added to the first one, the free energy cost for the insertion is again given by the one-body potential of the second particle, but there is an additional

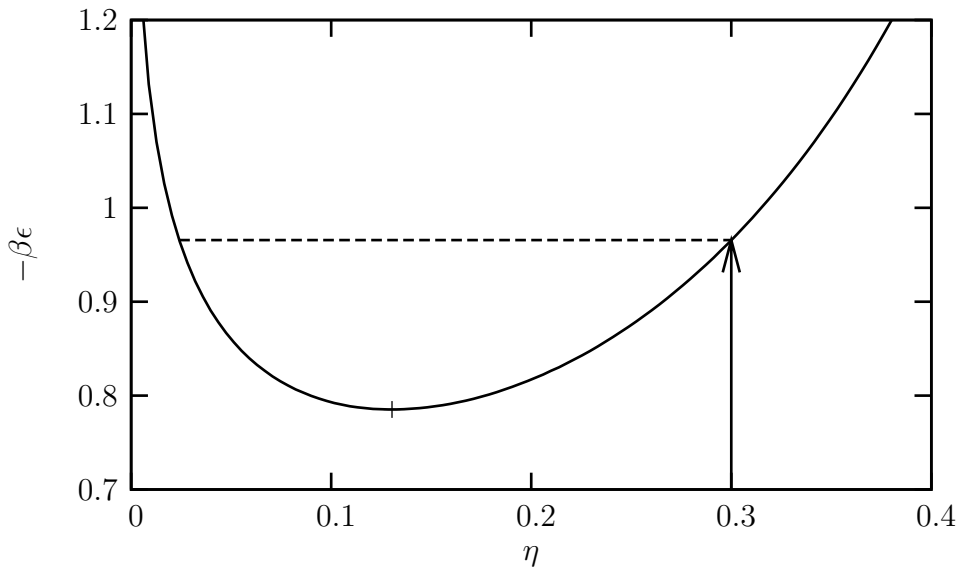


Figure 1.1: Phase diagram of a square-well fluid for  $R_\epsilon/R = 2$ . The high temperature expansion is applied using the White-Bear version of FMT as a reference system and the expression in Eq. (1.24) as the soft perturbation potential. The perturbation theory yields for this fluid a critical point at  $\eta_{cr} = 0.13044$  and  $\beta\epsilon_{cr} = -0.78528$ . For constant  $\eta_{liquid} = 0.3$  (arrow) and variable  $\beta\epsilon$ , the system is in a one-phase fluid state until it reaches the dashed tie-line at  $\beta\epsilon_{gl} = -0.96557$ . At this state point the bulk square well fluid coexists with a gas-phase with a smaller packing fraction of  $\eta_{gas} = 0.02404$ . If the system is close to the binodal and the fluid is brought in contact with a hard wall, a gas-phase wets the wall (drying).

amount of energy associated with the insertion which is referred to as the two-body potential. It equals the change in the grand potential when moving two big particles from infinite separations to a position of finite mutual distance and it is therefore called the effective interaction potential or depletion potential.

The first theoretical study of depletion potentials was done for a mixture of big colloids and ideal, non-interacting polymers by Asakura and Oosawa [7, 41] and, independly, by Vrij [42]. According to their models the effective interaction potential is proportional to the gain in accessible volume for the small polymers which is due to the depletion of excluded volume around two adjacent big colloids. The resulting effective potential is purely attractive and in qualitative agreement even for other solute mixtures as long as the bulk density of the small particles is low. This zeroth-order model however fails to predict the oscillatory structure of depletion potentials

as it completely neglects correlations among the small solute particles. For this reason more sophisticated methods like the Derjaguin approximation [43] or integral equation techniques [44, 45, 46] were developed. In this work we employ a theory for the calculation of the many-body potentials that is based on DFT [47]. It considers as an elementary step the “insertion” of one additional big colloidal particle  $B$  in an equilibrated fluid of small particles. The fluid may already contain zero or more other big particles at fixed positions. The term “big” does not necessarily mean that these particles must be larger than the small particles, it merely means that these particles are held fixed at a certain position and their internal degrees of freedom are not traced out, in contrast to the ones of the small particles. The reason for such a nomenclature is that, if the size asymmetry between “big” and “small” particle is large, the effective description of the big particles becomes increasingly effective because higher order many-body potentials can be neglected [48].

Upon the insertion of a particle  $B$  into a system the grand potential of the system changes. The potential distribution theorem, applied for a grand canonical ensemble, provides an exact expression for this change in  $\Omega$

$$\beta\Omega(\mathbf{r}_B) - \beta\Omega = -c_B^{(1)}(\mathbf{r}). \quad (1.25)$$

In this equation,  $\beta\Omega$  stands for the grand potential of the fluid before the insertion of particle  $B$  and  $\beta\Omega(\mathbf{r}_B)$  for the grand potential after the insertion of particle  $B$  at position  $\mathbf{r}_B$  to the equilibrated fluid. On the right hand side of Eq. (1.25),  $c_B^{(1)}(\mathbf{r})$  denotes the one-body direct correlation function of species  $B$  in the fluid. Note that Eq. (1.25) is also valid if only some of the particles of species  $B$  are held fixed, i.e. when one considers the particles of type  $B$  to make up a separate component of the background fluid with a density  $\rho_B \neq 0$ . Here however, we take the so-called dilute limit which means that there are no particles of species  $B$  except the fixed ones, i.e.  $\rho_B \rightarrow 0$ . In this limit we use the definition of the direct correlation function, Eq. (1.5), together with the expression for the excess free energy density functional  $\mathcal{F}_{ex}[\rho]$  as provided by FMT, Eq. (1.14). This yields

$$c_B^{(1)}(\mathbf{r}) = - \sum_{\alpha} \int d\mathbf{r}' \frac{\partial\beta\phi}{\partial n_{\alpha}(\mathbf{r}')} w_B^{(\alpha)}(\mathbf{r}' - \mathbf{r}), \quad (1.26)$$

where  $\alpha$  labels the six weight functions  $w_B^{(\alpha)}(\mathbf{r})$  of the big particle  $B$  and  $n_{\alpha}$  are the weighted densities of the background fluid. Note that in the dilute limit,  $\rho_B \rightarrow 0$ , the weighted densities  $n_{\alpha}(\mathbf{r})$  are determined by the density distribution of the small particles *before* the insertion of the additional particle  $B$ . Hence the density

---

distribution of the small fluid particles, which is needed to obtain  $c_B^{(1)}(\mathbf{r})$ , can be calculated without considering the inserted particle  $B$ . This makes Eq. (1.26) very efficient concerning actual numerical calculations. After the weighted densities and the fields  $\psi^\alpha(\mathbf{r}) = \delta\beta\phi/\delta n_\alpha(\mathbf{r})$  have been determined the other big particle is, in a second step, “inserted” in the system which yields a direct correlation function  $c_B^{(1)}(\mathbf{r})$  according Eq. (1.26). The shape of  $B$  enters  $c_B^{(1)}(\mathbf{r})$  by the functional form of the weight functions  $w_B^{(\alpha)}(\mathbf{r})$ .

# Chapter 2

## Fluids at Curved Interfaces

Fluids brought in contact with a wall form an interface which leads to interesting physical effects. The particular focus of Chapter 3 is to study the influence of curved interfaces on fluids, i.e. the dependence of various physical quantities of the fluid on the shape of the wall that determines the interface. In the first section of this chapter, commonly used thermodynamic quantities associated with an interface are reviewed and the concept of the dividing interface is presented in detail. The particular focus concerns the involved subtleties when considering curved interfaces or fluid mixtures. In the second section, three sum-rules are derived that connect thermodynamic quantities and must be fulfilled for all types of fluids. Such relations are very useful to validate numerical data and will allow us in a later stage to make rigorous statements about the shape dependence of different fluid properties in Section 4.2.

### 2.1 Excess Adsorption and Interfacial Tension

We consider a fluid in contact with a wall as sketched in Fig. 2.1. For reasons of clarity we limit our presentation in the beginning to a one-component fluid of spheres and a hard curved wall, although generalizations of this simple situation are possible for most of the following equations and will be provided separately whenever necessary. From the viewpoint of DFT, a monodisperse fluid is described by a density functional  $\Omega[\rho(\mathbf{r})]$  of the form as defined in Eq. (1.1). Although exact and practical expressions for  $\Omega[\rho(\mathbf{r})]$  are usually not known we can assume without loss of generality that such a functional exists and that it has a form as required by Eq. (1.1). The shape of the wall enters the functional  $\Omega[\rho(\mathbf{r})]$  via the external potential  $V_{ext}(\mathbf{r})$ . In case of a pure hard wall the potential is infinite if any part of the particle overlaps with

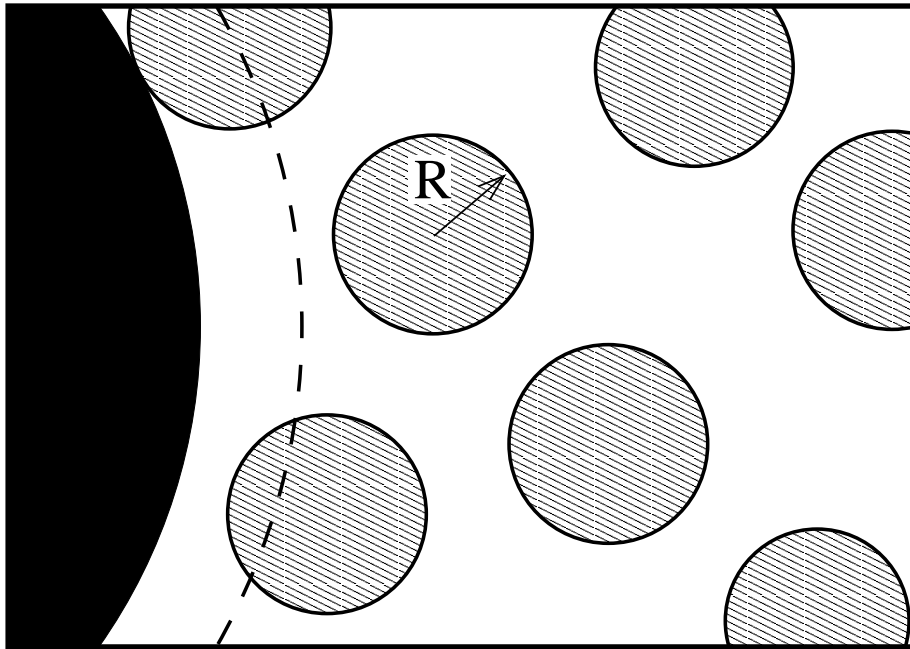


Figure 2.1: Sketch of fluid particles near a hard curved wall. The fluid particles are excluded from the full region, the physical wall, which means that the centers of the particles must not cross the surface indicated by the dashed line. For spherical particles with radius  $R$ , the dashed line is a parallel surface with normal distance  $u = R$  to the physical wall. We refer to it as an effective wall for the fluid and it may serve as a dividing interface when calculating excess quantities.

the wall and vanishes otherwise. For spherical particles this is equivalent to saying that the external potential equals infinity if the centers of the particles are within a volume bound by a parallel surface to this wall, indicated by the dashed line in Fig. 2.1. The distinction between the two parallel surfaces becomes crucial later in this thesis and we therefore introduce the following nomenclature. The volume in space from which all points of the particles are excluded is bound by a surface which we refer to as “physical wall” (perimeter of the full region in Fig. 2.1). In contrast to this, the “effective wall” bounds a volume that must not be crossed by the *centers* of the particles. Note that for a fluid mixture the physical wall is the same for every component whereas the effective wall is in general different for each species of particles. For a mixture of polydisperse spheres, the physical and all effective walls are mutual parallel surfaces. This is in principle also the case for components which consist of nonspherical particles as long as the particles can freely orient in space.

The external potential exerted by the wall leads to an equilibrium density distri-

bution of fluid particles, which can be determined e.g. by means of DFT. The density profile  $\rho(\mathbf{r})$  tends for sufficient large normal separation from the wall to the bulk density  $\rho_b$ , which is determined by the chemical potential  $\mu$ . In order to quantify the degree of perturbation induced by the external potential  $V_{ext}$  one uses the excess adsorption

$$\Gamma = \frac{1}{A} \left( \int \rho(\mathbf{r}) d\mathbf{r} - \rho_b V \right). \quad (2.1)$$

It describes how many particles of the fluid are adsorbed at the wall per unit area of the effective wall. The term ‘‘excess’’ refers to the fact that the total adsorption, i.e. the number of particles  $\int \rho(\mathbf{r}) d\mathbf{r}$  in the system, is measured relative to the number of particles in a virtual bulk reference system with an adsorption  $\rho_b V$ . This bulk reference system extends up to a surface called the dividing interface and is defined such that it has bulk properties *everywhere* within the volume bounded by the dividing interface. The choice of the position of the dividing interface is in principle completely arbitrary. For fluid mixtures, the most natural choice is the physical wall, however for a single-component fluid in the literature often the effective wall is selected instead. Unlike otherwise stated, the dividing interface in this thesis is chosen to lie on the effective wall (dashed line in Fig. 2.1) for reasons that will be discussed in detail in Section 3.2. This convention determines the surface area  $A$  of the dividing interface and also the volume  $V$  of the bulk reference system that is confined by the dividing interface. These two geometrical quantities,  $A$  and  $V$ , are used in Eq. (2.1) and it is therefore obvious that the choice of the dividing interface influences the numerical value of the excess adsorption  $\Gamma$ . This fact does not represent a practical problem as excess absorptions obtained for different dividing interfaces can always be converted using Eq. (A.14), however physical statements involving the adsorption should be made such that they are independent of the actual choice of the dividing interface. This important point will be discussed when deriving Eq. (3.5).

Similar to the change in the density profile  $\rho(\mathbf{r})$  the hard curved wall leads to a grand potential  $\Omega = \Omega[\rho(\mathbf{r})]$  that is different from the grand potential of the bulk reference system. The difference in the potentials can be interpreted as the free energy cost to form the wall-fluid interface and is conventionally quantified using the interfacial tension

$$\gamma = \frac{1}{A} (\Omega[\rho(\mathbf{r})] - \Omega_b), \quad (2.2)$$

where  $\Omega_b = -pV$  is the grand potential of the bulk reference system. This definition also uses the volume  $V$  and area  $A$  as defined by the convention for the bulk reference system or the dividing interface, respectively. Note that we distinguish the interfacial



tension  $\gamma$  from the *surface* tension. The latter denotes the interfacial tension at a planar, infinitely extended wall.

## 2.2 Sum Rules and Contact Density

Excess adsorption  $\Gamma$  and interfacial tension  $\gamma$  are not independent thermodynamic quantities of the interface, but connected through a sum rule, which can be derived by forming partial derivatives with respect to the chemical potential  $\mu$  on both sides of Eq. (2.2). Using the definition of the density functional, Eq. (1.1), and the result of the Gibbs-Duhem relation that  $\partial p/\partial\mu = \rho_b$  one finds the Gibbs adsorption theorem

$$\left(\frac{\partial\gamma}{\partial\mu}\right)_{T,V} = -\Gamma. \quad (2.3)$$

The partial derivative is meant to be taken for a constant temperature  $T$  and, indicated by the subscript  $V$ , a fixed position of the physical wall which means in particular that the geometry of the wall is unchanged. It is worthwhile to note that the connection between  $\gamma$  and  $\Gamma$  is done by a partial derivative with respect to an intensive quantity, where ‘‘intensive’’ means that it does not depend on any geometrical feature of the wall. This observation is important as it results in the same dependence for  $\gamma$  and  $\Gamma$  on the shape of the wall.

We find another sum rule for a hard wall by forming a normal derivative on both sides of Eq. (2.2). The concept of a normal derivative is described in Appendix A and defined in Eq. (A.15). In the case of a cylindrical or a spherical wall it is equivalent to a derivative with respect to the radius of the wall. For the normal derivative of  $\Omega[\rho]$  we find

$$d_u\beta\Omega[\rho(\mathbf{r})] = \int \underbrace{\frac{\delta\beta\Omega[\rho(\mathbf{r})]}{\delta\rho(\mathbf{r}')}}_{=0} d_u\rho(\mathbf{r}') d\mathbf{r}' + \int \rho(\mathbf{r})d_u(\beta V_{ext}(\mathbf{r})) d\mathbf{r}. \quad (2.4)$$

The functional derivative in the first integral vanishes because of the Euler-Lagrange equation for the equilibrium grand potential  $\Omega[\rho(\mathbf{r})]$ . In order to evaluate the second term we recall that the potential exerted by a hard wall is infinite inside the effective wall and vanishes outside. One can formulate the potential exerted by the effective wall on the centers of the particles using the normal coordinates generated by the effective wall, Eq. (A.17). If we denote  $u(\mathbf{r})$  the normal distance of the center  $\mathbf{r}$  of a particle from the effective wall, we can write for the wall-fluid potential

$$\exp(-\beta V_{ext}(\mathbf{r})) = \Theta(u(\mathbf{r})). \quad (2.5)$$

From this equation we evaluate the normal derivatives on both sides which yields  $d_u \beta V_{ext}(\mathbf{r}) = -\exp(\beta V_{ext}(\mathbf{r}))\delta(u)$ , where  $\delta(u)$  denotes the usual Dirac  $\delta$ -distribution. This yields, inserted in Eq. (2.4),

$$d_u \Omega[\rho(\mathbf{r})] = - \int \rho(\mathbf{r}) \exp(\beta V_{ext}(\mathbf{r})) \delta(u(\mathbf{r})) d\mathbf{r}. \quad (2.6)$$

The  $\delta$ -distribution in the integrand on the right hand side restricts the integration to  $u = 0$ , i.e. the volume integration becomes a surface integration along the effective wall of the component. As this is the surface which no center of the particle must cross, the density profile  $\rho(\mathbf{r})$  jumps at this locus between a finite contact density, denoted  $\rho^c$ , and zero. One can show that in contrast to the discontinuity of  $\rho(\mathbf{r})$  the integrand in Eq. (2.6),  $\rho(u) \exp(\beta V_{ext}(u))$  is a continuous function of  $u$  such that the integrand yields for  $u \rightarrow 0^+$

$$-d_u \beta \Omega[\rho(\mathbf{r})] = \int_W \rho(\mathbf{r}) d^2 r = \int_W \rho^c d^2 r = A \bar{\rho}^c, \quad (2.7)$$

where  $W$  denotes the effective wall and  $A$  its total surface area. We introduced  $\bar{\rho}^c$ , the average contact density, where the averaging is done over the effective wall  $W$ .

The result found in Eq. (2.7) can be extended to account also for two more general cases: a multi-component fluid and a wall that features aside from a hard interaction also a soft potential  $V_{soft}^i(u)$  for each component  $i = 1, 2, \dots, N$ . In this more general case, Eq. (2.7) becomes

$$-d_u \beta \Omega[\rho(\mathbf{r})] = \sum_{i=1}^N \left( A_i \bar{\rho}_i^c + \int_{W_i} d^2 r \int du J_i(u) \frac{dV_{soft}^i(u)}{du} \rho_i(u) \right), \quad (2.8)$$

where  $W_i$  denotes the effective wall of component  $i$ ,  $A_i$  the total surface of  $W_i$  and  $J_i(u)$  the Jacobi determinant, Eq. (A.13), of the normal coordinates generated by  $W_i$ .  $\rho_i(u)$  is the density profile of species  $i$ . Equation (2.8) shows that for a pure hard wall,  $V_{soft}^i(u) = 0$ , the normal derivative  $d_u \Omega$  is solely determined by the weighted sum of all averaged contact densities  $\bar{\rho}_i^c$  of each component  $i$ . Only in this case the grand potential is linked directly to the contact densities, which will become important when deriving the morphometric form of the contact density in Eq. (3.6). If, in contrast, the soft tail  $V_{soft}^i(u)$  of the potential is not a constant, also densities aside from the contact  $u = 0$  contribute to  $d_u \Omega$ .

We now return to the considerations for a pure hard wall. With the results of Eq. (2.7) the normal derivative of  $A\beta\gamma = \beta\Omega[\rho] + \beta pV$  [Eq. (2.2)] can be written as

$$\bar{\rho}^c = \beta p + 2\bar{H}\beta\gamma + \partial_u \beta\gamma. \quad (2.9)$$

Here  $\bar{H} = C/A$  denotes the averaged mean curvature of the wall. This sum rule, Eq. (2.9) represents a generalization of the relations derived in Refs. [49, 50] for a cylindrical and a spherical wall. It applies to any fluid in contact with an arbitrarily shaped hard wall. Note that in order to derive Eq. (2.9) in this form we assume that the quantity  $A$  in Eq. (2.7), the surface area of the effective wall, is the same as the quantity  $A$  in Eq. (2.2), the surface area of the dividing interface. This is indeed the case by virtue of our convention for the dividing interface of a monodisperse fluid. For a multi-component fluid, the sum-rule becomes

$$\sum_i \frac{A_i^e}{A^d} \bar{\rho}_i^c = \beta p + 2\bar{H}\beta\gamma + \partial_u \beta\gamma. \quad (2.10)$$

$A_i^e$  denotes the surface area of the effective wall of component  $i$  and  $A^d$  the surface area of the dividing interface.

A third sum rule is obtained by combining the two previous ones. For a monodisperse fluid we apply Eq. (2.9) and form a partial derivative with respect to the chemical potential  $\mu$ . Using Eq. (2.3) and the Gibbs-Duhem relation yields

$$\frac{\partial \bar{\rho}^c}{\partial \beta \mu} = \rho_b - 2\bar{H}\Gamma - \partial_u \Gamma. \quad (2.11)$$

Again,  $\bar{H} = C/A$  was used. This sum-rule is remarkable as it connects  $\bar{\rho}^c$ , the contact density averaged over the effective wall, to the excess adsorption  $\Gamma$ , which stems from an integral over the whole density profile  $\rho(\mathbf{r})$ . We elucidate the special status of the contact density at a hard wall and its connection to the density profile in more detail in Section 3.2.

The three sum rules, Eqs. (2.3), (2.9), and (2.11), are all exact relations provided that the wall-particle interaction is hard and that the grand potential  $\Omega$  depends continuously on the geometry of the wall. The latter restriction is needed in order to ensure that partial derivatives acting on  $\Omega$  can be interchanged. Aside from these assumptions, the sum rules are very general, i.e. they can be applied to all kinds of fluids under all thermodynamic states. We use them in Sections 3.1 and 3.2 to connect the shape dependence of thermodynamic quantity to other quantities.

# Chapter 3

## Shape Dependence of Thermodynamic Quantities

When a fluid is brought in contact with a wall, it forms an interface which can be described by thermodynamic quantities introduced in the previous chapter. These thermodynamic quantities depend on a large variety of different parameters, such as the type of fluid, the chemical potentials, or the temperature of the system. Some of the parameters, as the ones mentioned, do not depend on the geometry of the wall which determined the shape of the interface. Aside from these so-called intensive parameters there is however also a dependence on the shape of the wall. It is the main topic of this chapter to study this functional dependence on the geometric properties of the wall in detail. Before we analyze it for different thermodynamic quantities, we first examine the dependence of the grand potential  $\Omega$  on the shape of the wall. From this result we then deduce in Section 3.2 the shape-dependence of other thermodynamic quantities.

### 3.1 Morphometric Thermodynamics

We consider fluid particles which are confined to a certain volume in space by a wall which surrounds the system. We refer to the set of points accessible to the centers of fluid particles as the system  $S$ . As indicated in the introduction, the particular interest of this section is the dependence of the grand potential  $\Omega$  on  $S$ , i.e. we regard  $\Omega$  as a functional  $\Omega[S]$  of the system  $S$ . The actual form of the functional depends on the intensive parameters of the fluid, which are however taken to be constant throughout this section and their notion is consequently suppressed. In principle the

functional mapping  $\Omega[S]$  is known explicitly. If  $\rho_b$  denotes the bulk density,  $\mu_{ex}$  the excess chemical potential and  $V(\mathbf{r}^N)$  the total potential of a given configuration  $\mathbf{r}^N$  of centers of particles,  $\Omega[S]$  is the logarithm of the grand partition sum

$$\beta\Omega[S] = \log \left( \sum_{N=0}^{\infty} \frac{(\rho_b \exp(\mu_{ex}))^N}{N!} \int_S d\mathbf{r}^N \exp(\beta V(\mathbf{r}^N)) \right). \quad (3.1)$$

Note that the functional dependence of  $\Omega[S]$  on system  $S$  enters via the range of integration over the phase-space in Eq. (3.1). Unfortunately, for a non-trivial fluid and a complexly shaped  $S$ , it is usually impossible to calculate the integrals over the phase-space exactly and therefore Eq. (3.1) provides little insight into the shape dependence of  $\Omega[S]$ . To proceed, various methods are used. DFT or integral equation techniques provide approximate expressions for quantities that cannot be obtained exactly by analytic means. In contrast to these analytic approaches, Monte-Carlo (MC) or molecular dynamics (MD) simulations are conceptually exact numeric algorithms, the results however are affected by inevitable statistical errors. These methods have in common that a system  $S$  must be explicitly given parameterized by a formula or in form of a numerical data set such that the problem can be implemented and solved numerically. This however leads to problems if the boundary of  $S$  has a complex shape, i.e. if  $S$  is *not* bound by a highly symmetric wall. Such geometric setups demand in general that all calculations must be carried out on a three dimensional grid space which makes the numerical solution very costly and usually at the same time inaccurate. In our approach we include the system  $S$  in the configuration of the fluid and aim to identify the thermodynamically relevant geometrical parameters. What are these parameters? One usually argues that  $\Omega[S]$  is as every other thermodynamic potential an extensive quantity, which means that it scales linearly with the “size” of the system  $S$ . For two disjoint systems  $S_1 \cap S_2 = \emptyset$  one demands that  $\Omega[S_1 \cup S_2] = \Omega[S_1] + \Omega[S_2]$ , i.e. that the grand potentials add up when two systems are considered as a single system. Note that the total volume  $V[S]$  of the system fulfills  $V[S_1 \cup S_2] = V[S_1] + V[S_2]$ , and so does every constant multiple  $\omega V[S]$ . One therefore assumes as a preliminary ansatz that  $\Omega[S] = \omega V[S]$ , where  $\omega$  is an intensive quantity that must not depend on  $S$ . In the case of the grand potential  $\Omega$ , it equals the negative of the pressure  $p$  in the system. This simple ansatz shows that  $V[S]$  is a thermodynamically relevant geometrical measure. It is possible to continue this analysis by noting that the surface area  $A[S]$  of the system also fulfills  $A[S_1 \cup S_2] = A[S_1] + A[S_2]$  for disjoint  $S_1 \cap S_2 = \emptyset$ . The respective conjugated quantity is conventionally denoted  $\sigma$  and is referred to as the surface tension of the system. It is also an intensive quantity and

depends, in contrast to the pressure  $p$ , also on the wall-particle interaction potential. With this term, a more extended ansatz for the grand potential is  $\Omega[S] = -pV[S] + \sigma A[S]$ . In principle one can continue to add further terms. If  $S$  is bound by a polyhedra, i.e. bound by sections of planes, one normally introduces line- and point-tensions of the fluid. Otherwise, an infinite expansion in integrated powers of the local curvatures of the wall is used to describe the full influence of the shape of  $S$  on  $\Omega[S]$ .

We perform a more systematic analysis of  $\Omega[S]$  by extending the conventional concept of extensivity. In particular we argue that the functional  $\Omega[S]$  should have certain mathematical properties. We impose the following three restrictions on the mapping  $\Omega[S]$ .

- (i) **Motion invariance:** The thermodynamic potential  $\Omega[S]$  should be independent of the location and orientation of the system  $S$  in space, i.e.  $\Omega[gS] = \Omega[S]$  for all translations and rotations  $g$  in 3 dimensions. This property requires that the total potential  $V(\mathbf{r}^N)$  in Eq. (3.1) is motion-invariant, which is the case if the external potential is considered to be part of  $S$  and is also affected by the action of  $g$ . Thus motion invariance is fulfilled for all types of *fluids*.
- (ii) **Conditional continuity:** If a sequence of convex sets  $S_n$  converges towards the convex set  $S$  for  $n \rightarrow \infty$ , then we demand that  $\Omega[S_n] \rightarrow \Omega[S]$ . Intuitively, this continuity property expresses the fact that an approximation of a convex domain by e.g. a convex polyhedra also yields an approximation of the thermodynamic potential  $\Omega[S]$  by  $\Omega[S_n]$ . This property is not necessarily fulfilled in all situations. It is shown in the context of scaled-particle theory (SPT) [51] that conditional continuity is violated if the system  $S$  is of comparable size to the fluid particles [20]. This is intuitively obvious as a small system can only hold a few particles due to the high spacial confinement. Even a small variation of  $S$  may increase or decrease the total number of particles allowed in the system by one, i.e. the number of particles may discontinuously depend on  $S$ . This discontinuity in the particle number affects also the grand potential  $\Omega$  and therefore violates conditional continuity. However, this effect becomes negligible if the number of particles in  $S$  is large, i.e. in the thermodynamic limit. Thus, in order to exclude “few-particle” effects, we demand that the container  $S$  must be sufficiently large. The typical radii of curvature must be large compared to the size of fluid particles. In this case the fluid can be viewed macroscopically and conditional continuity is fulfilled. The term “conditional” refers to the fact that

this property is only needed to be fulfilled for convex systems  $S$ . Note that this does not mean that all systems  $S$  for which our approach can be applied must necessarily be convex [52].

- (iii) **Additivity:** The functional of the union  $S_1 \cup S_2$  of two domains  $S_i$ ,  $i = 1, 2$ , should be the sum of the functional of the single domains subtracted by the intersection

$$\Omega[S_1 \cup S_2] = \Omega[S_1] + \Omega[S_2] - \Omega[S_1 \cap S_2]. \quad (3.2)$$

This relation generalizes the common rule for the addition of an extensive quantity for two disjunct domains  $S_1 \cap S_2 = \emptyset$ , as presented above. In the case of overlapping domains the grand potential of the double-counted intersection is subtracted from the sum. Similar to restriction (ii), namely conditional continuity, additivity also requires large systems  $S_1$  and  $S_2$ . This becomes evident when considering two systems which are made such that both cannot hold a particle on their own, although their union is large enough to do so. This gedankenexperiment leads to a violation of Eq. (3.2). Note that this is *not* due to our extensions of the concept of extensivity, but rather because extensivity assumes from the outset that a macroscopic view on the fluid is a valid description. This normally requires large systems  $S$  such that the thermodynamic limit is valid. Aside from these few-particle effects also long-ranged correlations in the fluid violate Eq. (3.2), as this equation implies that perturbations induced in the fluid by one part of the wall does not influence the formation of another interface due to another part of the wall. We therefore demand  $S$  to be large enough that e.g. for concave systems the typical distances between opposing parts of the wall are large compared to the correlation length. This excludes fluids with intrinsic long-ranged interactions or fluids near the critical point. We also exclude wetting or drying, which leads to long-ranged correlations parallel to the interface [53]. To summarize we demand that all systems  $S$  are large compared to any internal length scale of the fluid.

We assume that a macroscopic view of the fluid is a valid and that  $\Omega[S]$  therefore fulfills conditions (i)-(iii). We will refer to quantities with these properties as morphometric<sup>1</sup> quantities. It should however be pointed out that we cannot rigorously prove that the grand potential is morphometric for a specific non-trivial fluid. The

---

<sup>1</sup>The term “morphometric” is a synonym for “morphologic”. In this thesis we stick to the first expression.

three restrictions should rather be understood as more rigorous formulation of the concept of extensivity motivated by physical intuition and we will show in Section 3.3 that we find, based on this assumption, a consistent description for all systems we study. As already discussed above, there however *are* systems for which (ii) or (iii) is violated, namely small containers  $S$ , where “small” means that geometrical features of the container are comparable to the size of fluid particles, interaction length scales, correlation lengths, or wetting layer thicknesses. If on the other hand motion-invariance, conditional continuity and additivity are fulfilled, the question arises about the most general form of  $\Omega[S]$  which satisfies these three conditions. The Hadwiger theorem [52, 54] states that every functional in three dimensions with these properties can be written as a linear combination of the volume  $V[S]$ , the surface area  $A[S]$ , the integrated mean curvature  $C[S]$ , and the Euler characteristic  $X[S]$  of the container wall [for definitions see Eqs. A.9 and A.10]. Therefore we write

$$\Omega[S] = -pV[S] + \sigma A[S] + \kappa C[S] + \bar{\kappa} X[S], \quad (3.3)$$

as an ansatz for  $\Omega[S]$  and refer to this ansatz as the morphometric form of the grand potential [55]. The pressure  $p$ , the surface tension at the planar wall  $\sigma$ , and the two bending rigidities  $\kappa$  and  $\bar{\kappa}$  are independent of  $S$ , i.e. intensive parameters. They only depend on other intensive properties such as the type of fluid, the chemical potential  $\mu$ , the temperature  $T$ , and the wall-fluid interaction potential. The conjugated quantities to the intensive parameters in Eq. (3.3) are the four morphometric measures  $V$ ,  $A$ ,  $C$ , and  $X$ . They obey restrictions (i)-(iii) and are the only thermodynamically relevant variables associated with shape.

It is worthwhile to note that Eq. (3.3) provides a complete multiplicative separation of the grand potential in intensive and morphometric quantities. This is very favorable, both conceptually and practically.  $\Omega$  can be obtained even for complexly shaped systems  $S$ , as the geometry of  $S$  enters the thermodynamic potential only via four morphometric measures  $V$ ,  $A$ ,  $C$ , and  $X$ . The thermodynamic coefficients  $p$ ,  $\sigma$ ,  $\kappa$ , and  $\bar{\kappa}$  are independent of  $S$  and can hence be obtained from simple geometric setups. Note that similar quantities as we introduce in Eq. (3.3) are commonly used in the context of an effective Hamiltonian of an interface, the Helfrich Hamiltonian [56]. It is compatible with Eq. (3.3) on a length scale larger than the persistence length of the interface, where renormalized contributions proportional to  $H^2$  vanish due to thermal fluctuations.



## 3.2 Morphometric Form of Thermodynamic Quantities

The application of the morphometric form of  $\Omega[S]$  to a fluid in contact with a wall requires a closer look to the definition of  $S$ . As pointed out in Section 2.1 a clear distinction should be made between the physical and the effective wall for each component of the fluid. Each of these walls may serve as an alternative perimeter for a system  $S$ , which consequently leads to different morphometric measures. It is however an advantage of Eq. (3.3) that all descriptions for different definitions of the system  $S$  are equivalent. The grand potential is a well-defined quantity and therefore the choice of  $S$  must not influence actual value of  $\Omega[S]$ . It however determines how the grand potential is distributed among the four terms in Eq. (3.3). By using Eq. (A.14) one can show that only the thermodynamic coefficients  $\sigma$ ,  $\kappa$ , and  $\bar{\kappa}$  are affected by the choice of a different parallel surface as a wall for  $S$ , whereas the general form of Eq. (3.3) is conserved. Therefore the choice of the boundary of  $S$  is arbitrary and in this thesis we choose, unless otherwise stated, the effective wall for all monodisperse fluids.

The reason for this choice becomes evident when considering thermodynamic quantities associated with the interface as introduced in Sections 2.1 and 2.2. Inserting the morphometric form of  $\Omega$  in Eq. (2.2) yields

$$\begin{aligned}\gamma &= \frac{1}{A} ((-pV[S] + \sigma A[S] + \kappa C[S] + \bar{\kappa} X[S]) + pV) \\ &= \sigma + \kappa \bar{H} + \bar{\kappa} \bar{K},\end{aligned}\tag{3.4}$$

where we have introduced  $\bar{H} = C[S]/A$  and  $\bar{K} = X[S]/A$  as the averaged mean and averaged Gaussian curvature of the effective wall or the dividing interface respectively [for definitions see Eq. (A.8)]. As expected, the contribution proportional to the volume  $V[S]$  cancels because  $\gamma$  is an excess quantity. This is always the case, irrespective of the definition of the dividing interface. The reason for choosing our convention for the boundary of  $S$  and the dividing interface is that it allows us to identify  $V[S] = V$  and  $A[S] = A$ , which is essential in order to obtain a simple expression for  $\gamma$  such as in Eq. (3.4). According to this equation, the interfacial tension shows an analytic dependence on the radii of curvature of the wall which supports e.g. the ansatz used in SPT [51, 57, 50]. Here, the analytic dependence on the radii of curvatures is a direct consequence of the additivity of the grand potential. In contrast to earlier approaches with an infinite series expansion in the radii of curvature, our expansion

of  $\gamma$  in powers of  $H$  and  $K$  truncates already after the linear terms. We refer to this particular simple dependence of  $\gamma$  on the shape of the wall as the “morphometric form” of the interfacial tension. Its characteristic is that it does not require higher powers or derivatives of  $\bar{H}$  or  $\bar{K}$  to describe the influence of the curved wall.

The excess adsorption  $\Gamma$  of the interface is found by forming the derivative of Eq. (3.4) with respect to the chemical potential  $\mu$  for constant temperature and shape  $S$ . This yields by virtue of the Gibbs adsorption theorem, Eq. (2.3), for the excess adsorption

$$-\Gamma = \left( \frac{\partial \gamma}{\partial \mu} \right)_{T,S} = \frac{\partial \sigma}{\partial \mu} + \frac{\partial \kappa}{\partial \mu} \bar{H} + \frac{\partial \bar{\kappa}}{\partial \mu} \bar{K}. \quad (3.5)$$

It is important to realize that the derivative is taken at constant shape  $S$  and therefore the geometrical measures  $\bar{H}$  and  $\bar{K}$  are not affected by the derivative with respect to the intensive quantity  $\mu$ . We therefore find also for the excess adsorption  $\Gamma$  a morphometric form. There is only a linear dependence on both curvatures  $H$  and  $K$ .

In the case that the system  $S$  is bound by a *hard* wall we insert the morphometric form of the interfacial tension, Eq. (3.4), in the contact theorem Eq. (2.9). The normal derivatives of the geometric measures are summarized in Eq. (A.16) and the resulting relation is

$$\bar{\rho}^c = \beta p + 2\beta\sigma\bar{H} + \beta\kappa\bar{K}. \quad (3.6)$$

Therefore, also the average contact density  $\bar{\rho}^c$  at a hard wall has a morphometric form. This is remarkable insofar as Eq. (3.6) is derived using a normal derivative, i.e. a derivative with respect to a geometric quantity. Nonetheless only a linear dependence in both curvatures  $H$  and  $K$  is needed to describe  $\bar{\rho}^c[S]$ .

Equations (3.4), (3.5), and (3.6) provide very simple expressions for the dependence of  $\gamma$ ,  $\Gamma$ , and  $\bar{\rho}^c$  on the shape of the wall. We will refer to all quantities which feature such morphometric dependence on the shape of the wall as “thermodynamic quantities”. It should be noted that thermodynamic quantities are averages over the *whole* surface of  $S$ . This is in particular also the case for  $\bar{\rho}^c$ , indicated by a bar on top of the symbol. These three quantities are related to the *averaged* curvatures  $\bar{H}$  and  $\bar{K}$  via their morphometric forms. Therefore the morphometric expressions can, strictly speaking, only be used when one is interested in a thermodynamic description of a system as a whole and if one is not interested in microscopic details of the interface. If however the lateral variation of the curvatures  $H$  and  $K$  along the surface can be neglected, one can replace averaged quantities by their respective local counterparts. We term these relations *local* morphometric forms. They are exact if  $H$  and  $K$  are constant on the surface, which is the case for a planar, a cylindrical, and a spherical

walls. Otherwise, for walls with varying  $H$  and  $K$ , the local morphometric forms can be used as an approximation. We show numerically in the next section that the local forms of Eqs. (3.4), (3.5), and (3.6) provide good predictions when applied to surfaces with a smooth variation of the curvature.

### 3.3 Numerical Results

This section summarizes a large numerical study that we conducted in order to test the morphometric form of thermodynamic quantities. No violations are found, which means that the predictions of Section 3.1 provide an excellent numerical description for the studied fluids. We start our analysis by considering a fluid of monodisperse, hard spheres. Such a fluid features short-ranged interactions and has no critical point. In the fluid phase, which is stable for  $\eta \leq 0.494$ , the correlation length is in the order of the diameter  $2R$  of the fluid spheres. Due to these properties we expect that morphometry is fulfilled for this system. Another advantage of the hard-sphere fluid is that it is very well studied and excellent numerical methods exist to describe it. We use the Rosenfeld and the White-Bear functional which both support our conjecture and give qualitatively the same results in the following analysis. In the first subsection we do not test the morphometric hypothesis but rather assume that it is valid, which is justified numerically in the subsequent subsections. Based on this assumption, we present a numerical scheme that allows to calculate all four thermodynamic coefficients  $p$ ,  $\sigma$ ,  $\kappa$ , and  $\bar{\kappa}$  based on data obtained from DFT calculations or other numerical methods. We present our results and compare them to an approximate bulk theory. In the second subsection, we use the four thermodynamic coefficients to predict the thermodynamic quantities around various objects and find that the agreement between the morphometric hypothesis on the one hand and DFT or Monte-Carlo results on the other hand is excellent. In the third subsection we include for the analysis of our numerical data also terms of higher powers in  $H$  and  $K$  for thermodynamic quantities, which would be a contradiction to the morphometric forms. We then show numerically that the expansion coefficients corresponding to higher powers of  $H$  or  $K$  are numerically zero, i.e. very small which is in agreement with the overall accuracy of the DFT results. In the final subsection we verify that the results obtained for a hard-sphere fluid in contact with a hard wall are not an artifact of the pure hard interactions. We generalize the findings to soft walls and also discuss results obtained for a square-well fluid, which features a phase coexistence close to which the morphometric arguments fail due to drying effects, as expected.

### 3.3.1 Thermodynamic Coefficients

In order to apply the morphometric form of  $\Omega$  the four thermodynamic coefficients must be determined. For this we consider a fluid of hard spheres with radius  $R$  with a fixed bulk density  $\eta$ . Such a fluid is in contact with a spherical wall with radius  $R_S$ , where  $R_S$  denotes the radius of the *physical* wall. The effective wall, which is by our convention identical to the dividing interface, is therefore also a spherical surface but has a radius  $R_S + R$  with the corresponding dimensionless curvatures  $\bar{H} = H = R/(R_S + R)$  and  $\bar{K} = K = (R/(R_S + R))^2$ . According to the morphometric expressions Eq. (3.4) for the interfacial tension  $\gamma$  and Eq. (3.6) for the average contact density  $\bar{\rho}^c$ , the following relations apply for a wall with constant curvatures

$$\begin{aligned}\beta\gamma(R_S) &= \beta\sigma + \beta\kappa\frac{R}{R_S + R} + \beta\bar{\kappa}\frac{R^2}{(R_S + R)^2}, \\ \bar{\rho}^c(R_S) &= \beta p + 2\beta\sigma\frac{R}{R_S + R} + \beta\kappa\frac{R^2}{(R_S + R)^2}.\end{aligned}\tag{3.7}$$

If the interfacial tension and the contact density are known only for two different radii  $R_S$ , Eq. (3.7) provides four linear equations which can be solved for all four thermodynamic variables  $p$ ,  $\sigma$ ,  $\kappa$ , and  $\bar{\kappa}$ . It must however be noted that such an approach is very sensitive to numerical errors. Therefore it can only be applied if the numerical values for  $\gamma(R_S)$  or  $\bar{\rho}^c(R_S)$  are known very accurately. Results found by means of DFT are sufficiently reliable, which does not mean that they are exact but merely that they can be reproduced with very high accuracy and not affected by statistical noise. In this case we use data obtained for two arbitrary values of  $R_S$  to find the thermodynamic coefficients as described above. The results are independent of the choice of  $R_S$ , as long as  $R_S$  is not too large such that too many significant digits of the numerical data cancel.

If only noisy data is available, which may for instance be the case for thermodynamic quantities obtained from MD or MC simulations, the thermodynamic coefficients can be obtained by choosing a large set of various values of  $R_S$ . For each value of  $R_S$ ,  $\gamma$  and  $\bar{\rho}^c$  are needed and the results are fitted for the thermodynamic coefficients using Eq. (3.7) as an ansatz. This scheme is more stable under the influence of numerical noise than the previous approach. When using DFT results, the coefficients we find by the second scheme agree with those found by the previous one very accurately. This already indicates that the morphometric hypothesis yields a consistent description of  $\gamma$  and  $\bar{\rho}^c$  for the hard-sphere fluid at a spherical wall.

We repeat the analysis as described above for various bulk packing fractions  $\eta$ .

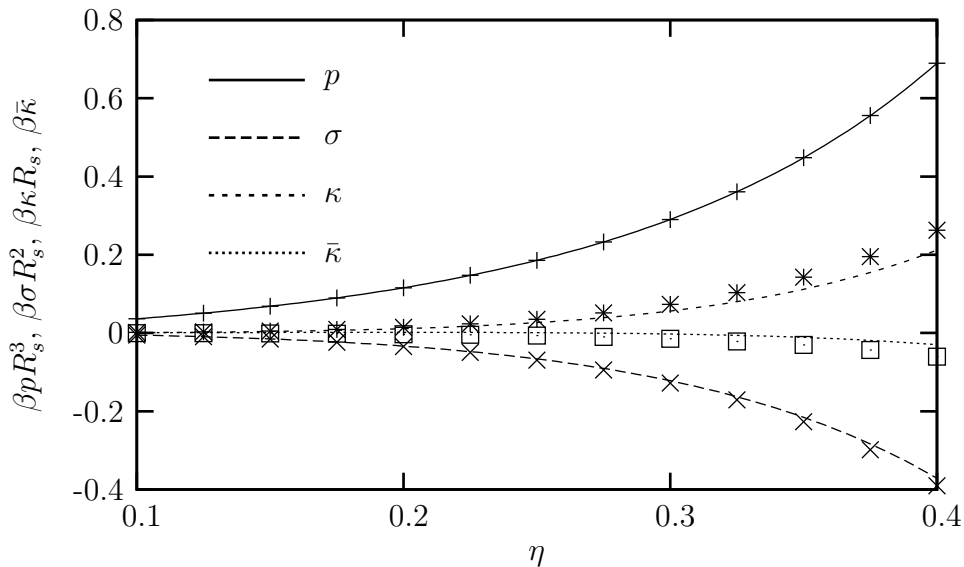


Figure 3.1: Thermodynamic coefficients for a fluid of hard spheres versus the bulk packing fraction  $\eta$  modeled via the Rosenfeld functional. The lines show the results of the approximate bulk theory, Eq. (3.11), while the points are obtained using DFT results of simple geometries. For the pressure  $p$  a perfect agreement is observed, because the Rosenfeld functional is built on the scaled particle differential equation. The other thermodynamic coefficients are only reproduced qualitatively by the bulk theory.

The symbols in Fig. 3.1 and Fig. 3.2 show the results for the Rosenfeld and the White-Bear functional, respectively. In these figures the numerical data is compared with the results of an approximate bulk theory (lines), which predicts analytical expressions for the thermodynamic coefficients based on the special form of FMT-based density functionals. For this theory one considers the bulk state of the fluid for which the thermodynamic quantities should be calculated. In this bulk fluid a big particle  $B$  is inserted that excludes the particles of the fluid from a certain volume. Hence, particle  $B$  acts as a wall to the fluid and defines a system  $S$ . According to Section 1.4 the change  $\Delta\Omega$  in the grand potential upon insertion is

$$\Delta\Omega = \lim_{\rho_B \rightarrow 0} \frac{-c_B^{(1)}}{\beta} = \lim_{\rho_B \rightarrow 0} \frac{\delta\mathcal{F}_{ex}[\rho_s, \rho_B]}{\delta\rho_B}, \quad (3.8)$$

where  $\mathcal{F}_{ex}[\{\rho_i\}]$  is an excess free energy density functional that describes the mixture of a hard-sphere component with density  $\rho_s$  and a big particle  $B$  component with density  $\rho_B$ . If  $\mathcal{F}_{ex}[\{\rho_i\}]$  is a FMT-based functional given by Eq. (1.14) a description of the mixture is always available, because FMT itself provides a framework to treat

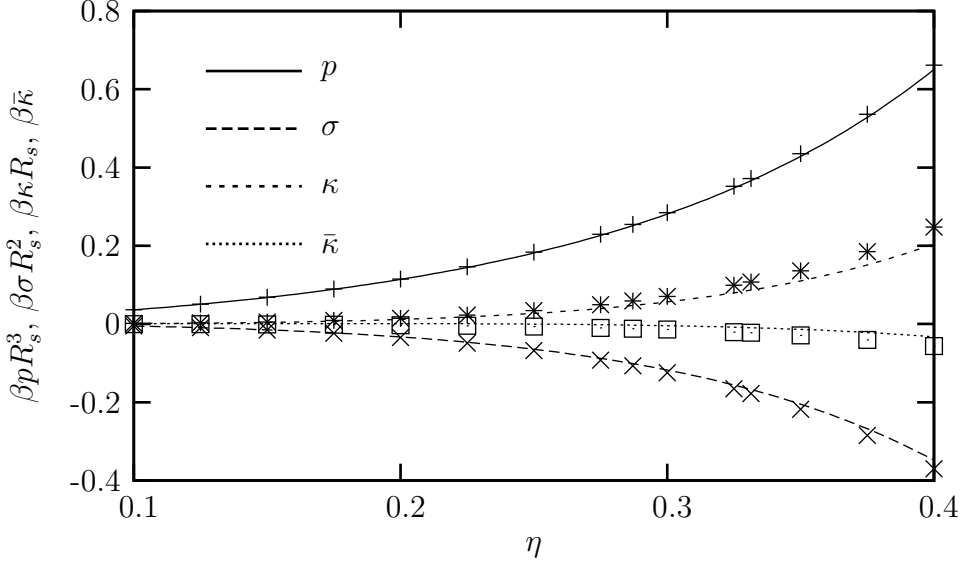


Figure 3.2: Same as in Fig. 3.1, except that the White-Bear version of FMT was used as a model. Although the pressure  $p$  is reproduced quite accurately by the bulk theory, the other thermodynamic coefficients are only qualitatively reproduced. We find that the numerically determined coefficients of this functional provide an excellent predictions for quasi-exact MC simulation data, see Fig. 3.4.

fluid mixtures, see Eq. (1.20). With these assumptions we write the change in  $\Omega$  upon insertion of  $B$  in the bulk fluid as

$$\begin{aligned} \Delta\Omega = & \frac{\delta\phi}{\delta n_3} \int w_B^{(3)}(\mathbf{r}) d\mathbf{r} + \frac{\delta\phi}{\delta n_2} \int w_B^{(2)}(\mathbf{r}) d\mathbf{r} + \\ & + \frac{\delta\phi}{\delta n_1} \int w_B^{(1)}(\mathbf{r}) d\mathbf{r} + \frac{\delta\phi}{\delta n_0} \int w_B^{(0)}(\mathbf{r}) d\mathbf{r}. \end{aligned} \quad (3.9)$$

The partial derivatives with respect to the vector-weighted densities  $n_1$  and  $n_2$  are zero in the bulk. For the weight functions  $w_B^{(\alpha)}$  of the particle of species  $B$  we use the expressions provided by the approximate FMT for convex hard particles, Eq. (1.21). One can evaluate the integrals over the weight functions analytically

$$\begin{aligned} \int w_B^{(3)}(\mathbf{r}) d\mathbf{r} = V_B, \quad \int w_B^{(2)}(\mathbf{r}) d\mathbf{r} = A_B, \\ \int w_B^{(1)}(\mathbf{r}) d\mathbf{r} = \frac{C_B}{4\pi}, \quad \int w_B^{(0)}(\mathbf{r}) d\mathbf{r} = \frac{X_B}{4\pi}. \end{aligned} \quad (3.10)$$

$V_B$ ,  $A_B$ ,  $C_B$ , and  $X_B$  denote the respective geometrical measures of particle  $B$  which was inserted in the bulk fluid and now acts as a physical wall. Under the assumption that the thermodynamic coefficients for the physical wall are sought, we readily identify  $p' = \partial\phi/\partial n_3$ ,  $\sigma' = \partial\phi/\partial n_2$ ,  $4\pi\kappa' = \partial\phi/\partial n_1$ , and  $\bar{\kappa}' = \partial\phi/\partial n_0$ . Note that there

is no minus-sign in the definition of the pressure. It cancels because of our definition of the system  $S$ , which comprises all points in space that are accessible to the small particles of the fluid. Thus  $S$  is the whole space *less* the points of particle  $B$ .

Our convention is to calculate the thermodynamic coefficients for the effective wall. Therefore we write the geometric measures of the effective wall as a function of the measures of particle  $B$ , the physical wall. This is done using Eq. (A.14) and leads to a linear combination of the  $\partial\phi/\partial n_\alpha$ -terms. For the original Rosenfeld functional we obtain

$$\begin{aligned}\beta p &= \rho \frac{1 + \eta + \eta^2}{(1 - \eta)^3}, & \beta \sigma &= -\frac{3\rho}{2} \frac{1 + \eta}{(1 - \eta)^3}, \\ \beta \kappa &= 3\rho \frac{\eta^2}{(1 - \eta)^3}, & \beta \bar{\kappa} &= \frac{\rho(-2 + 7\eta - 11\eta^2)}{6(1 - \eta)^3} - \frac{1}{4\pi} \ln(1 - \eta).\end{aligned}\tag{3.11}$$

Similarly we derive for the White-Bear version of FMT that

$$\begin{aligned}\beta p &= \rho \frac{-1 + 6\eta - 3\eta^2}{(1 - \eta)^3} - \frac{3}{2\pi} \ln(1 - \eta), & \beta \sigma &= \rho \frac{3 - 9\eta - 4\eta^2}{(1 - \eta)^3} + \frac{9}{4\pi} \ln(1 - \eta), \\ \beta \kappa &= \rho \frac{-4 + 10\eta - 4\eta^2}{(1 - \eta)^3} + \frac{3}{\pi} \ln(1 - \eta), & \beta \bar{\kappa} &= \frac{\rho(4 - 9\eta + 3\eta^2)}{3(1 - \eta)^3} - \frac{1}{\pi} \ln(1 - \eta).\end{aligned}\tag{3.12}$$

Note in particular that the pressure  $p = p' = \partial\phi/\partial n_3$  in the case of the White-Bear functional does not yield the MCSL-EoS for one component, Eq. (1.18). This is due to the fact that the functional does not respect the SPT differential equation. Figure 3.1 shows these results for various bulk densities and compares the results of the approximate bulk theory, Eq. (3.11), to the data obtained from direct minimization of the Rosenfeld functional. In Fig. 3.2 we show the respective comparison for the White-Bear functional.

Although the general trend is the same when comparing bulk theory and direct DFT data it is obvious that the bulk theory only yields approximate expressions for the thermodynamic coefficients. The reason for this is twofold: FMT-based functionals are approximate and cannot exactly produce all correlations between the fluid particles and particle  $B$  which would be needed to apply the insertion method exactly. Additionally, FMT for nonspherical particles introduces approximations even in the low density limit, which are however recovered exactly in the spherical case. In the following we will therefore use the numerically determined thermodynamic coefficients. Their dependence on the bulk packing fraction  $\eta$  is well fitted via the

following relations. For the Rosenfeld functional we obtain

$$\begin{aligned}\frac{\beta\sigma(1-\eta)^3}{\rho^2} &\approx -\frac{3}{2}\eta - 1.871\eta^2 - 0.022\eta^3 + 0.673\eta^4, \\ \frac{\beta\kappa(1-\eta)^3}{\rho^2} &\approx 3.979\eta^2 + 0.242\eta^3 + 0.452\eta^4 - 4.348\eta^5, \\ \frac{\beta\bar{\kappa}(1-\eta)^3}{\rho^2} &\approx \frac{1}{3}\eta - 1.778\eta^2 - 3.001\eta^3 + 7.948\eta^4.\end{aligned}\tag{3.13}$$

We determine the terms up to  $\mathcal{O}(\eta)$  from the bulk theory presented above, which is exact in the low density limit  $\eta \rightarrow 0$ . The decimal fractions in Eq. (3.13) are fitting constants obtained for a range of packing fractions between  $\eta = 0.05$  and  $\eta = 0.4$ . Note that the pressure  $p$  obtained from DFT very accurately reproduces the PY-EoS, Eq. (1.16). Similarly, for the White-Bear version of FMT, we find

$$\begin{aligned}\frac{\beta\sigma(1-\eta)^3}{\rho^3} &\approx -\frac{3}{2}\eta - 1.883\eta^2 + 0.377\eta^3 + 1.578\eta^4, \\ \frac{\beta\kappa(1-\eta)^3}{\rho^3} &\approx 4.010\eta^2 - 0.032\eta^3 + -1.200\eta^4 - 4.703\eta^5, \\ \frac{\beta\bar{\kappa}(1-\eta)^3}{\rho^3} &\approx \frac{1}{3}\eta - 1.819\eta^2 - 2.609\eta^3 + 7.469\eta^4.\end{aligned}\tag{3.14}$$

The pressure of this model is given by the CS-EoS, Eq. (1.18) and agrees very accurately with the numerical data obtained by direct minimization of the functional.

### 3.3.2 Applications

We calculate thermodynamic quantities for a fluid in contact with an arbitrarily shaped hard wall based on the four thermodynamic coefficients determined in the previous section. Figure 3.3 shows the interfacial tension  $\gamma$  and the excess adsorption  $\Gamma$  for a cylindrical ( $C$ ) and a spherical ( $S$ ) wall for various radii  $R_\alpha$ ,  $\alpha = C, S$ . The results obtained by direct DFT calculations are compared to the predictions of the morphometric conjecture, for which we use the numerically determined thermodynamic coefficients of the Rosenfeld functional as displayed in Fig. 3.1.

We observe an excellent agreement between direct DFT data and the morphometric prediction as displayed in Fig. 3.3. The figure shows a typical example, for other values of the bulk packing fraction and for the White-Bear version of FMT the agreement is similarly excellent. In addition to  $\gamma$  and  $\Gamma$ , also the average contact density  $\bar{\rho}^c$  is predicted accurately by the morphometric form, as we show in Fig. 3.4 below. These findings show that DFT results of a hard-sphere fluid in contact with



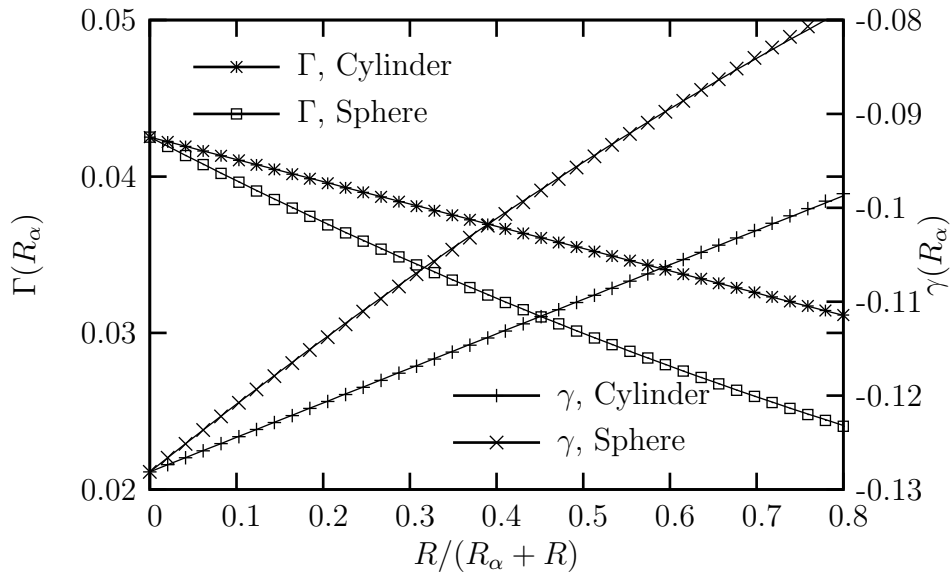


Figure 3.3: Thermodynamic quantities for a hard-sphere fluid in contact with a hard cylindrical and spherical wall of radius  $R_\alpha$ . The lines are predictions based on the morphometric approach. For the interfacial tension we use Eq. (3.4), for the excess adsorption  $\Gamma$  we use Eq. (3.5). The agreement to direct DFT data, shown as symbols, is excellent. For this figure we use the Rosenfeld functional and a bulk packing fraction of  $\eta = 0.3$ . We verified that other  $\eta$  and the White-Bear version of FMT give similar results. Note that for  $R_\alpha \rightarrow \infty$ , i.e. for  $R/(R_\alpha + R) \rightarrow 0$  the results for both cylinder ( $\alpha = C$ ) and sphere ( $\alpha = S$ ) must coincide with the ones for a planar wall.

hard cylindrical or spherical walls are compatible with the morphometric forms for thermodynamic quantities.

We emphasize that the morphometric form of a thermodynamic quantity is not a truncated power series in the inverse radii of curvatures. It can therefore be used to predict thermodynamic quantities of fluids at walls with very high curvatures without the loss of accuracy. As an illustration, Fig. 3.4 shows the average contact density  $\bar{\rho}^c$  at a spherical wall with radius  $R_S$ .

Even for  $R_S \rightarrow 0$  the agreement between direct DFT results and morphometric prediction is excellent. As already mentioned, DFT yields results that are in full agreement to the morphometric prediction. This is remarkable insofar as a very small wall leads inevitably to “few-particle” effects as discussed in the context of SPT [51]. We excluded such effects when deriving the morphometric form of the grand potential  $\Omega$  in Section 3.1. Therefore an agreement as good as shown in Fig. 3.4

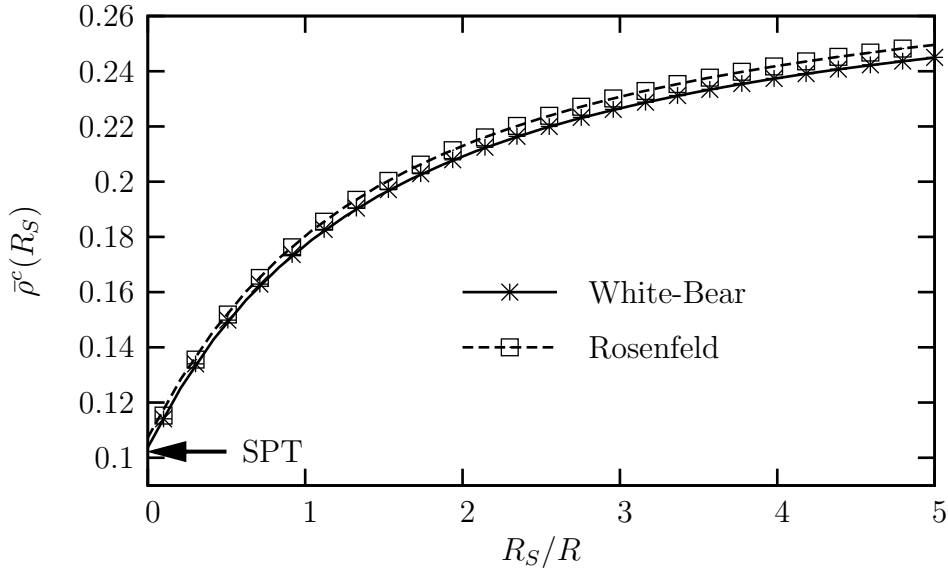


Figure 3.4: Contact density of a hard sphere fluid with  $\eta = 0.3$  in contact with a hard spherical wall of radius  $R_S$ . DFT results are shown as symbols, the morphometric prediction is shown as a line. We display results for both the original Rosenfeld functional and the White-Bear version of FMT. The agreement between morphometric prediction and direct DFT calculations is excellent for all values of  $R_S$ . In order to estimate the influence of “few-particle” effects as discussed in Section 3.1, the arrow indicates the exact SPT result, Eq. (3.15), for  $R_S = 0$ . For both density functionals the agreement is surprisingly good. We verified that a similar good agreement is also observed for other bulk packing fractions  $\eta$ .

cannot be expected from the outset. One may argue that DFT, as the morphometric approach, does not respect “few-particle” effects either and that therefore the numerical values both for the morphometric form and direct DFT minimization are practically meaningless. It is however possible to independently check both predictions, as SPT provides an *exact* expression for the contact density of a hard-sphere fluid at a point-like wall, i.e. a spherical wall with radius  $R_S = 0$

$$\bar{\rho}^c(R_S = 0) = \frac{\rho}{1 - \eta}. \quad (3.15)$$

We show this result as an arrow in Fig. 3.4. The agreement to the results of DFT and morphometry is surprisingly good. For a bulk packing fraction of  $\eta = 0.3$ , the relative error for the Rosenfeld functional is  $1.1 \times 10^{-2}$ , for the White-Bear functional even  $2.2 \times 10^{-3}$ . We find that the relative error increases with increasing bulk packing fraction  $\eta$ , however it is e.g. for the White-Bear functional below 0.5% for  $\eta \leq 0.42$ .

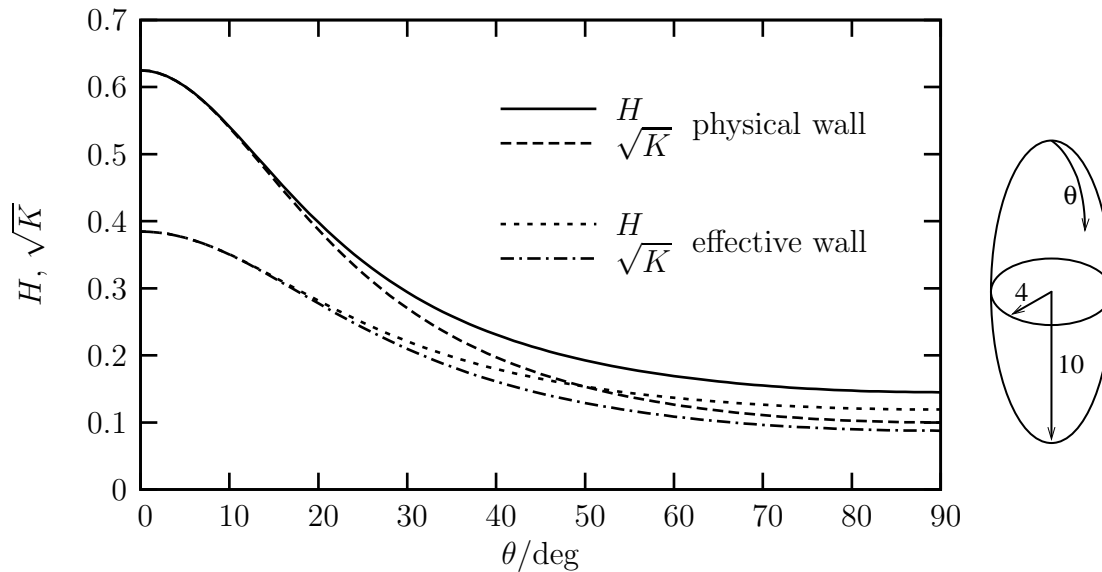


Figure 3.5: Local curvatures of a biaxial ellipsoid with half axes  $(4, 4, 10)R$  (prolate ellipsoid). The physical wall is given by Eq. (A.21) with  $a = b = 4R$  and  $c = 10R$  and the curvature of the physical wall are calculated from Eq. (A.22). For the effective wall with parallel distance  $u = R$  we use Eq. (A.12) to obtain the local curvatures. For small  $\theta$ , the curvatures  $H$  and  $K$  are the largest and also their lateral derivatives are maximal. Note that for  $\theta \rightarrow 0$  the surface of the biaxial ellipsoid locally looks like a sphere, i.e.  $H^2 \approx K$ . The thermodynamically relevant morphometric measures of the *physical* wall are  $V = 640\pi/3R^3$ ,  $A \approx 418.43R^2$ ,  $C \approx 80.018R$ , and  $X = 4\pi$ . The measures for the effective wall can be obtained using Eq. (A.14) with  $u = R$ .

Obviously the influence of the “few-particle” effects discussed in SPT on the contact density is not very strong and we therefore conclude that the morphometric forms for thermodynamic quantities at highly curved objects are not exact, but very good approximations.

Up to now we tested thermodynamic properties at walls with constant curvatures. In order to furthermore substantiate the morphometric approach we also consider more complexly shaped solutes. As a first system we study an ellipsoid immersed in a sea of hard spheres. The surface of the ellipsoid is given by Eq. (A.21) and the curvatures can be calculated using Eq. (A.22). In Fig. 3.5 we display the local mean and Gaussian curvatures  $H$  and  $K$  of the ellipsoid we consider here.

The data is shown for the physical wall, the surface of biaxial ellipsoid itself, and additionally for the effective wall which is a parallel surface with distance  $u = R$  for

fluid particles with radius  $R$ . The latter wall is by our convention also the dividing interface of the system. When we use morphometric forms in order to calculate local thermodynamic quantities, the influence of lateral variations of the curvatures is neglected. For positions with a parameter  $\theta$  near 90 deg, Fig. 3.5 shows that the lateral variations of the curvatures are minimal and we therefore expect that the local morphometric form yields the best predictions near the symmetry plane of the biaxial ellipsoid at  $\theta \approx 90$  deg.

It is important to realize that it is very costly from the numerical point of view to obtain accurate density distributions of particles around an object which does not feature a high spacial symmetry. DFT calculations for a hard-sphere fluid in contact with a planar, cylindrical, or spherical wall can analytically be mapped on an effective one-dimensional system and thus be solved very efficiently. This is not possible for an ellipsoidal geometry which would make the application of DFT methods very complicated. We use Monte-Carlo (MC) simulations of a hard-sphere fluid instead which are easier to implement for complexly shaped walls but nonetheless require a considerable calculation effort. A further advantage of simulation data is that this allows us to compare the morphometric predictions based on *approximate* DFT data with Monte-Carlo results which do not involve any approximation. For the actual implementation of the system the special type of symmetry of the problem suggests one should evaluate the density profile using a grid space generated by the normal coordinates of the physical wall, i.e. by the prolate ellipsoid. Such a procedure eliminates potential problems concerning the accurate evaluation of the local contact value  $\rho^c$  of the density profile that would arise e.g. on a Cartesian grid. The fact that the biaxial ellipsoid has rotational symmetry allows us to average the gathered statistics over the azimuthal angle  $\phi$ . Note that due to this averaging we expect the largest statistical error for  $\theta \rightarrow 0$ , where the Jacobi determinant of the normal coordinate system is minimal. The whole simulation comprises a total number of  $70 \times 10^9$  Monte-Carlo steps, and we determined the bulk packing fraction to be approximately  $\eta = 0.3314$ . In Fig. 3.6 we show the contact density versus the parameter  $\theta$  for a biaxial ellipsoid.

The general agreement between MC simulation data and morphometry is very good. Note that in particular no fitting parameter is used in Fig. 3.6. We determine the bulk packing fraction from the density  $\rho(\mathbf{r})$  at a large normal distances from the wall and obtain with this value for  $\eta$  in a second step the thermodynamic coefficients based on the analysis of independent DFT results, which are shown in Fig. 3.2. Aside from these thermodynamic coefficients, only the local curvatures of the effective wall are needed, which we obtain from Eq. (A.22). Note that the numerical effort for the

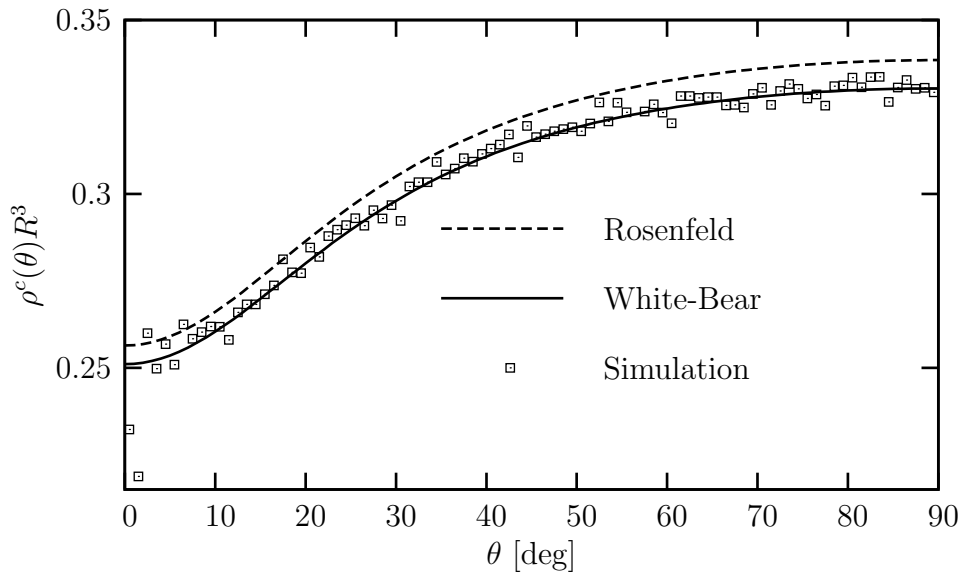


Figure 3.6: The contact density of a hard-sphere fluid around a biaxial prolate ellipsoid with half axes  $(4, 4, 10)R$ . Results from a grand canonical Monte-Carlo simulation for a bulk packing fraction of  $\eta = 0.3314$  are shown as symbols [58], the local morphometric prediction as lines. For the dashed line, the coefficients of the Rosenfeld functional, as shown in Fig. 3.1, are used. The solid curve shows a prediction based on the coefficients of the White-Bear functional, as displayed in Fig. 3.2. In particular the results for the latter functional are in excellent agreement with the numerical data. The statistical error of the simulation data is largest for  $\theta \rightarrow 0$ , as expected.

whole morphometric prediction is negligible compared to the numerical cost of a MC simulation.

Strictly speaking, the morphometric hypothesis applies only for averaged quantities of the whole system. In order to test it, we calculate from the local contact densities displayed in Fig. 3.6 the *average* contact density  $\bar{\rho}^c$  by integrating the (smoothed) simulation data over the effective wall. For the MC data the result is  $R^3\bar{\rho}^c = 0.318972$  which is in excellent agreement to the morphometric prediction,  $R^3\bar{\rho}^c = 0.318483$ . For this prediction the data obtained from the White-Bear functional for  $\eta = 0.3314$  is used. The agreement is remarkable insofar as we compare quasi-exact MC data with the morphometric results based on DFT data of an approximate functional. Furthermore the bulk packing fraction of the MC fluid can only be determined approximately in a grand canonical simulation such that an agreement within a relative error of  $1.6 \times 10^{-3}$  fully supports the morphometric conjecture.

The error bars of the simulation shown in Fig. 3.6 are relatively large, in particular for the data points close to the pole of the ellipsoid ( $\theta \rightarrow 0$ ). It would however be interesting to obtain also a good estimate for the contact density near the pole where the lateral variations of the curvature are largest and hence the largest deviation from the local morphometric form is expected. Instead of running an even larger simulation we consider a slightly different geometry instead. The reason for this is that the relatively poor statistics is due to the use of an ellipsoid as a physical wall. Such an object has relatively complicated effective surface and it must be checked repeatedly during the simulation whether the centers of the particles are outside this complicated effective wall or not. Therefore the simulation is very costly from a numerical point of view. The fact that we are not particularly interested in ellipsoidal walls suggests to consider a “shrunk ellipsoid” as a physical wall instead [see Eq. (A.23)]. It is defined such that the effective wall is a generic ellipsoid and for such a geometry it is much easier to determine whether a center of a fluid sphere lies within the effective wall or not. Therefore the MC steps consume significantly less CPU time and statistics can be gathered more efficiently. Figure 3.7 shows results obtained after  $500 \times 10^9$  MC steps and a shrunk ellipsoid with  $a = b = 4R$  and  $c = 10R$ .

Again, the agreement for larger values of  $\theta$  is very good, in particular for the morphometric results based on the White-Bear version of FMT. For  $\theta \rightarrow 0$  however there is a small discrepancy between the simulation results and the locally applied morphometric prediction, Eq. (3.6). The deviation is probably due to lateral variations in the curvature, which are the largest for  $\theta \rightarrow 0$  (see Fig. 3.5). However, when we integrate the data shown in Fig. 3.7 in order to obtain the average contact density  $\bar{\rho}^c$ , the result is  $R^3 \bar{\rho}^c = 0.239789$ . This is again in perfect agreement with the morphometric prediction  $R^3 \bar{\rho}^c = 0.239085$  based on the thermodynamic coefficients obtained from the White-Bear version of FMT and  $\eta = 0.3$ . The small relative error of  $3.0 \times 10^{-3}$  is due to the approximate nature of the density functional, the numerically measured bulk packing fraction, and the statistical error of the MC simulation. The morphometric form of  $\bar{\rho}^c$  is therefore also supported by these results.

The morphometric form of thermodynamic quantities applies also to objects which have discontinuities in the local curvatures along their surface. A commonly studied object with such properties is a spherocylinder. It is a joint object of a cylinder with radius  $R_{SC}$  and length  $L_{SC}$  and two half-spheres with the same radius  $R_{SC}$  attached to the end of the cylinder. A spherocylinder therefore discontinuously changes its shape from cylinder-like to sphere-like. Although the surface seems smooth, both the mean and the Gaussian curvature  $H$  and  $K$  feature a discontinuous jump at the

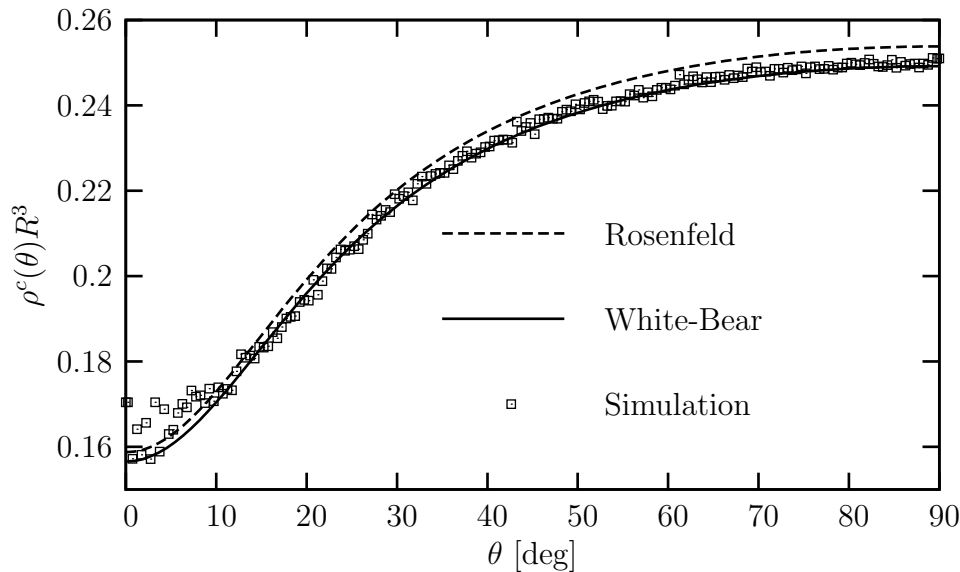


Figure 3.7: The contact density of a hard sphere fluid around a shrunk ellipsoid. The *effective* wall is a biaxial ellipsoid with half axes  $(4, 4, 10)R$ . Such an object is algorithmically easier to implement as the setup for Fig. 3.6 and therefore more statistics can be gathered. The symbols show MC simulation data, the lines are obtained from the morphometric form of the contact density, Eq. (3.6), applied locally. The dashed line is based on the Rosenfeld FMT, the solid line on the White-Bear version of FMT. In particular the latter functional provides a good description of the contact density, provided that lateral variations of the curvature are not too large as it is the case for  $\theta \rightarrow 0$ . The bulk packing fraction is approximately  $\eta = 0.300$ .

touching line between the cylinder and the spherical cap. The lateral variations of the curvatures diverge. In this situation it is obviously impossible to predict the local contact density  $\rho^c$  by use of a local morphometric form. The average mean  $\bar{H}$  and average Gaussian  $\bar{K}$  curvatures however are well-defined and finite quantities and we therefore use them to predict the average contact density  $\bar{\rho}^c$ . For this we consider a spherocylindrical solute with  $R'_{SC} = 3R$  and  $L'_{SC} = 10R$ , which has as an effective wall a spherocylinder with  $R_{SC} = R'_{SC} + R = 4R$  and  $L_{SC} = L'_{SC} = 10R$ . For a bulk packing fraction of  $\eta = 0.3$  and the White-Bear data we obtain  $R^3\bar{\rho}^c = 0.241586$  as the morphometric prediction. The corresponding simulation yields

$$R^3\bar{\rho}^c = 0.241335, \quad (3.16)$$

which represents a relative error of  $1.1 \times 10^{-3}$ . Hence this data also supports the morphometric conjecture. In Fig. 3.8 we show the dependence of the contact density

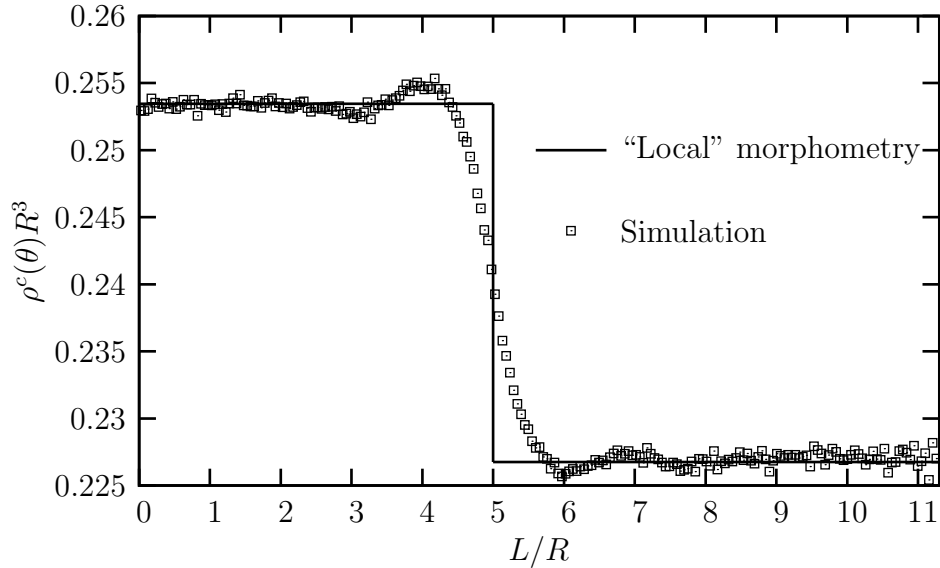


Figure 3.8: Contact density of a hard-sphere fluid around an effective spherocylinder with  $L_{SC} = 10R$  and  $R_{SC} = 4R$ . The parameter  $L$  on the abscissa parameterizes the distance of the contact position to the symmetry plane of the spherocylinder measured on its effective surface. For  $L < L_{SC}/2$ , the spherocylinder locally looks like a cylinder, for  $L_{SC}/2 < L < L_{SC}/2 + \pi/2 R_{SC}$  like a sphere. The symbols show the results of a MC simulation for a bulk packing fraction  $\eta = 0.300$ , the line shows the prediction based on the locally applied morphometric form of  $\bar{\rho}^c$ , Eq. (3.6). Only the averaged contact density  $\bar{\rho}^c$  shown in Eq. (3.16) is in perfect agreement with the prediction. For this figure, the thermodynamic coefficients of the White-Bear functional were used.

versus the position on the surface together with the local morphometric prediction, which does not reproduce the continuous transition between the cylinder and the sphere. Therefore, for discontinuous  $H$  and  $K$ , the morphometric form of thermodynamic quantities should only be applied to globally averaged quantities, where it provides a very accurate description.

So far, thermodynamic quantities have been shown for a fluid *outside* a hard wall and the question arises whether the morphometric approach can be extended also to fluids inside a concave cavity. The three conditions we impose on the grand potential do not limit the walls that bound  $S$  to be convex surfaces and we therefore predict thermodynamic quantities inside an object by using negative curvatures  $\bar{H}$  or  $\bar{K}$ . Such an approach can however only be valid as long as the cavity  $S$  is not too small. The wall that makes up the cavity introduces correlations in the fluid that decay for



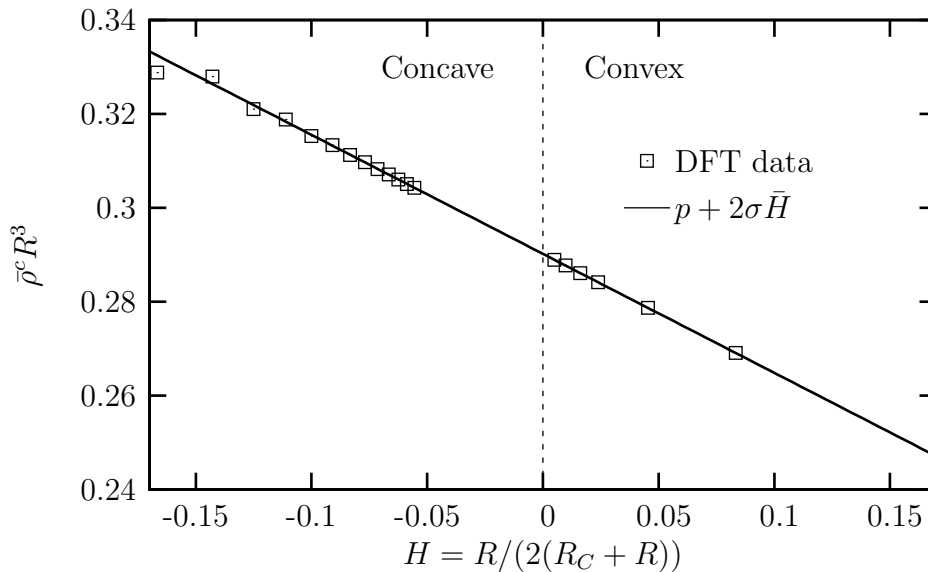


Figure 3.9: Contact density  $\bar{\rho}^c$  of a hard sphere fluid with a bulk packing fraction of  $\eta = 0.3$ . The fluid is in contact with a cylinder either from outside (convex,  $R_C > 0$ ) or inside (concave,  $R_C < 0$ ). The symbols [59] are results of the direct minimization of the Rosenfeld functional while the line is calculated using the morphometric approach and the coefficients of the Rosenfeld functional shown in Fig. 3.1. If the concave cylinder is sufficiently large, the morphometric from Eq. (3.6) provides an excellent approximation for the actual DFT results. Only for  $H \rightarrow -\infty$ , i.e. very narrow cavities, small deviations can be observed.

large normal distance from the wall. If however two opposing segments of a wall are sufficiently close, correlations introduced by both segments “interfere” and thermodynamic properties of the interface will therefore deviate from the values predicted by morphometry. This is in particular the case when correlations are still significant near caustic points. The reason for the failure of the morphometric prediction is the fact that the insertion of the second segment of the wall cannot be considered independently from the insertion of the first segment. This represents a violation of the additivity property of  $\Omega$ . If however the cavity is large enough, the morphometric forms of thermodynamic quantities provide an excellent approximation. As an illustration, Fig. 3.9 shows the contact density of a fluid of hard spheres inside and outside a cylinder for various values of  $R_C$ , including results for  $R_C < 0$ , a concave cavity.

According to the figure, thermodynamic coefficients obtained from the analysis of a fluid *outside* a hard wall can indeed be used to predict thermodynamic properties of

a fluid in a concave object. This can however only be done as long as no caustic effects occur, i.e. the density at the symmetry axis of the cylinder must be close to the bulk density  $\rho_b$ . Otherwise, if the cylinder is small, the influence of caustic effects yields DFT results that oscillate around the morphometric prediction for different values of  $R_C$ . For a bulk packing fraction of  $\eta = 0.3$  and a radius of curvature of the physical wall of  $R_C = -4R$ , the relative error between morphometric results and direct DFT minimization is below  $1.1 \times 10^{-2}$ . It increases with increasing bulk packing fraction  $\eta$ , because the decay length of correlations increases.

### 3.3.3 Accuracy and Error Estimates

Here we show that for the shape-dependence of the grand potential  $\Omega[S]$  as stated in Eq. (3.3) and the morphometric expressions for the related thermodynamic coefficients cannot be improved by adding additional higher order terms of the local curvatures. For this we include for the analysis of our numerical data additional terms which scale with higher powers of  $H$  and  $K$ . Such terms are not morphometric. Their numeric coefficients to the thermodynamic quantities  $\gamma$ ,  $\Gamma$ , and  $\rho^c$  must therefore all vanish according to the morphometric conjecture presented in Section 3.2. To this end we introduce the ‘‘curvature expansion’’ of an arbitrary quantity, which reads, e.g. for the contact density  $\rho^c$

$$\bar{\rho}^c = \rho_P^c + \rho_H^c H + \rho_K^c K + \rho_{H^2}^c H^2 + \rho_{HK}^c HK + \rho_{H^3}^c H^3 + \mathcal{O}(R_{1,2}^{-4}). \quad (3.17)$$

The curvature expansion coefficients  $\rho_\xi^c$  for  $\xi = P, H, K, H^2, HK, H^3, \dots$  can be determined by analyzing the curvature dependence of the contact density for simple geometries as obtained e.g. by direct minimization of a density functional. A numerical scheme for such an analysis is described in Appendix B. Based on DFT data for a hard-sphere fluid we obtain the expansion coefficients as displayed in Fig. 3.10.

This figure shows that irrespective of the bulk density only morphometric terms, i.e.  $\rho_P^c$ ,  $\rho_H^c$ , and  $\rho_K^c$  contribute to  $\bar{\rho}^c$ . Note that in particular the morphometric term  $\rho_K^c$  contributes to the contact density whereas the non-morphometric term  $\rho_{H^2}^c$  does not although both coefficients  $K$  and  $H^2$  feature a quadratic dependence on the radii of curvature. This suggests that the expansion of thermodynamic quantities in  $H$  and  $K$  should not be considered as a truncated power series. The higher order terms in the curvatures have virtually vanishing coefficients. Note that the numerically determined coefficients are not exactly zero due to numerical inaccuracies. We however observe that they decrease when the resolution of the DFT calculation is increased which is

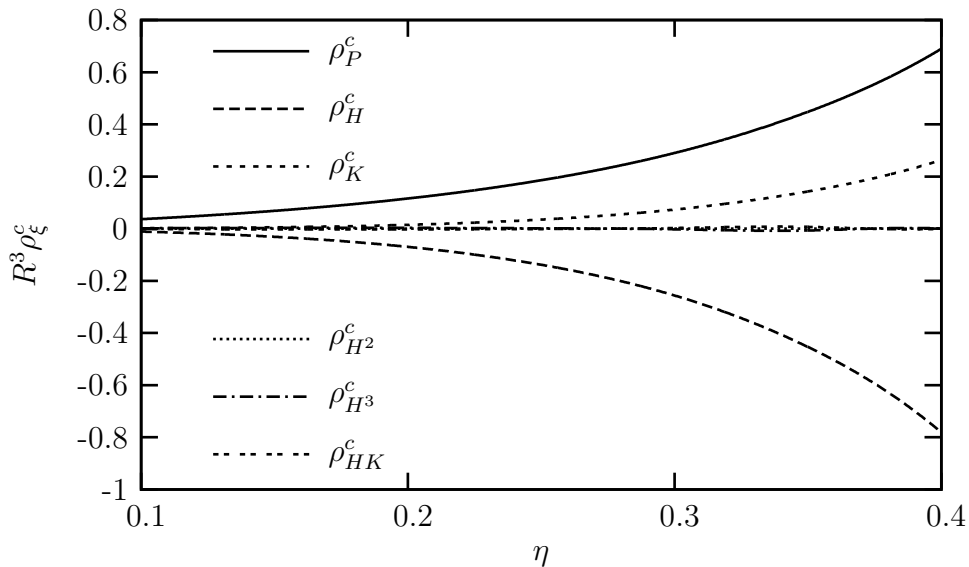


Figure 3.10: Curvature expansion coefficients of the contact density  $\rho^c$  as defined in Eq. (3.17) for various values of the bulk packing fraction  $\eta$ . Here we display the results of a hard-sphere fluid modeled via the Rosenfeld functional. The morphometric ansatz predicts that only the coefficients  $\rho_P^c$ ,  $\rho_H^c$ , and  $\rho_K^c$  of additive terms contribute to  $\rho^c$ . Our data confirms this numerically as non-additive terms are numerically zero for all values of the packing fraction  $\eta$ . In addition to the results shown here, we verified that also the results obtained from the White-Bear version of FMT and the Tarazona Mark I functional [60] show this behavior and hence confirm the morphometric form of the average contact density. This is analogously the case for the surface tension  $\gamma$  and the excess adsorption  $\Gamma$ .

a strong evidence for a parasitic effect. For the data shown in Fig. 3.10, the ratio  $\rho_K^c/\rho_{H^2}^c$  is above  $10^3$  for all packing fractions  $\eta$ .

With the curvature expansion coefficients  $\rho_\xi^c$  it is also possible to calculate the contact density around a curved wall. In contrast to the morphometric form which needs only three parameters, the full curvature is based on in principle an infinite number of coefficients. It is however important to realize that these additional parameters do not improve the prediction of  $\bar{\rho}^c$ , as we show in Fig. 3.11. The non-morphometric terms are obviously unnecessary and we therefore conclude that no higher than linear powers in the curvatures  $H$  or  $K$  are needed to fully describe the influence of the hard curved wall on a thermodynamic quantity.

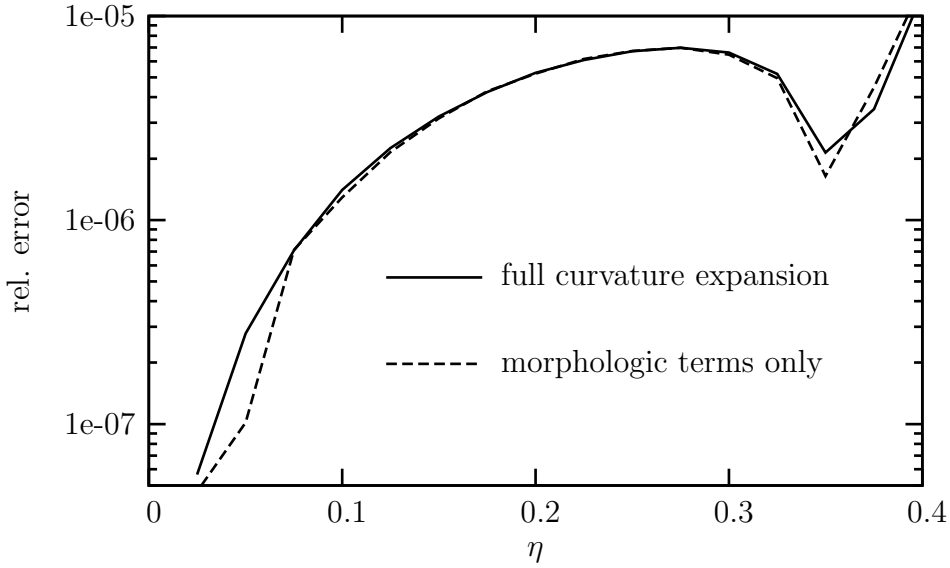


Figure 3.11: Relative error for the prediction of the contact density of a hard-sphere fluid in contact with a spherical wall with  $R_S = 5R$ . We consider the results obtained by a direct minimization of the Rosenfeld functional as a reference system. By the solid line we show the relative error compared to the prediction of the full curvature expansion of the contact density using the coefficients of Fig. 3.10. The dashed line shows the relative error of the morphometric ansatz, Eq. (3.6). In both cases, the result is nearly the same for all packing fractions  $\eta$  which shows that higher order terms do not improve the prediction of  $\bar{\rho}^c$ . The error is in both cases due to numerical inaccuracies of the DFT calculation and decreases for a higher resolution in the DFT program.

### 3.3.4 Beyond Pure Hard-Core Interactions

In the previous subsections we showed that thermodynamic properties of a fluid of hard spheres in contact with a hard curved wall can very accurately be explained using a morphometric approach. Our ansatz can however also be applied if the interactions are non purely hard. In order to show this we introduce a soft tail to the wall-particle interaction. For normal distances  $u > 0$  we choose a potential of the form

$$\beta V_{soft}(u) = \beta V_0 \exp(-u/\lambda). \quad (3.18)$$

$V_0$  measures the strength and  $\lambda$  the decay length of the soft potential. For  $V_0 = 0$  the situation of a pure hard wall is recovered. Otherwise, the wall is either attractive for  $V_0 < 0$ , or repulsive for  $V_0 > 0$ . We bring a fluid of hard spheres with radius  $R$  in contact with such a wall and analyze the dependence of thermodynamic

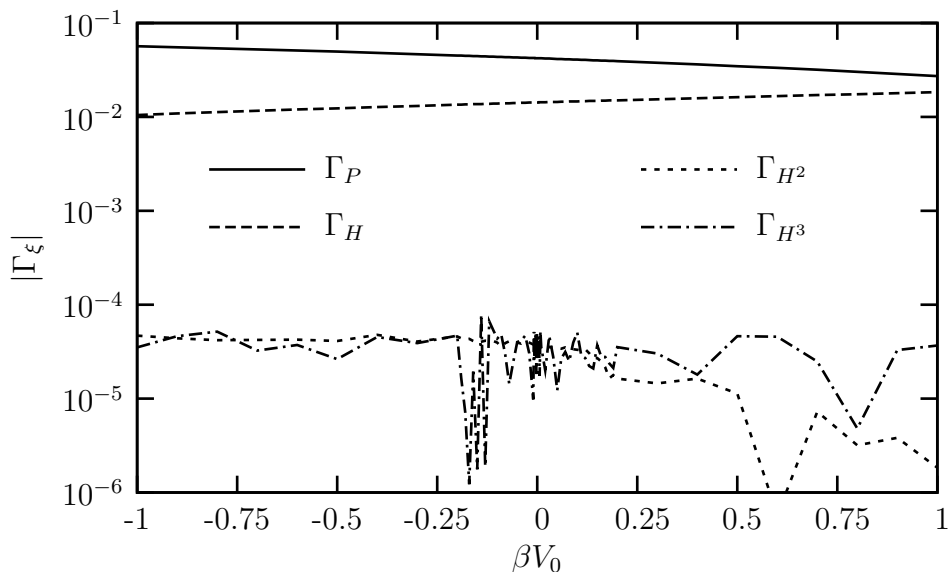


Figure 3.12: Curvature expansion coefficients of the excess adsorption  $\Gamma$ . As a system we use a hard-sphere fluid modeled via the Rosenfeld functional in contact with a hard-core cylindrical wall with a *soft* tail. The interaction potential is given by Eq. (3.18) with  $\lambda = R$ . The morphometric terms,  $\Gamma_P$  and  $\Gamma_H$  are large for all values of  $V_0$  which means that they are necessary to describe the influence of the curved wall. This is in contrast to the non-morphometric terms  $\Gamma_{H^2}$  and  $\Gamma_{H^3}$ , which are very small for all values of  $V_0$  and thus do not contribute to  $\Gamma$ . The non-morphometric terms are not exactly zero because of numerical inaccuracies. The bulk packing fraction is  $\eta = 0.3$ .

quantities on the shape. In order to estimate whether a morphometric form is sufficient to describe the influence of thermodynamic quantities on the shape we use the full curvature expansion as introduced in Eq. (3.17), which is more general than a morphometric expression. With this expansion we test numerically whether the coefficients of the non-morphometric terms vanish. In Fig. 3.12 we show some curvature expansion coefficients of the excess adsorption  $\Gamma$  as obtained from the minimization of the Rosenfeld functional at a hard-core cylindrical wall with a soft tail. In such a geometry the Gaussian curvature  $K = 0$  and we therefore obtain only the coefficients which belong to terms that scale with a pure power of the mean curvature  $H$ .

The excess adsorption  $\Gamma$ , as well as the interfacial tension  $\gamma$  are both thermodynamic quantities independent of the value  $V_0$  and hence can be described by morphometric forms. In contrast to this, the average contact density  $\bar{\rho}^c$  is only a thermodynamic quantity for  $V_0 = 0$  by virtue of the contact theorem. For nonzero  $V_0$

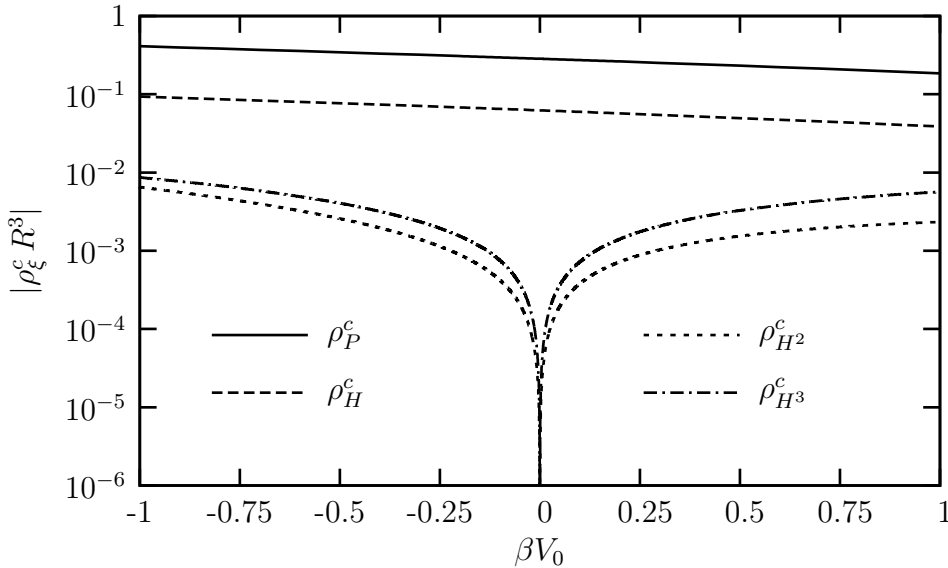


Figure 3.13: Identical setup as in Fig. 3.12, but here we show curvature expansion coefficients for the contact density  $\bar{\rho}^c$ . For  $\beta V_0 = 0$  the morphometric form of  $\bar{\rho}^c$ , Eq. (3.6), is sufficient but even for relatively small values of  $\beta V_0 \neq 0$  also higher powers of the curvatures are needed to fully describe the influence of the curved wall.

the contact theorem, Eq. (2.7), cannot be applied in this form any more. For walls with a soft potential also densities  $\rho(u)$  at normal distances  $u \neq 0$  contribute to the normal derivative of the grand potential  $\Omega$ , as shown in Eq. (2.8). This means that, although the morphometric form of  $\Omega$  is conserved independently of the value of  $V_0$ , one cannot expect that the morphometric form of  $\bar{\rho}^c$  is sufficient to describe the influence of the curved wall. Higher terms of the curvature expansion are needed. We show in Fig. 3.13 the expansion coefficients for  $\bar{\rho}^c$ .

Aside from non-hard wall-particle interactions we also consider non-hard inter-particle interactions. To this end we employ the perturbation theory as reviewed in Section 1.3 in order to calculate thermodynamic properties of a square-well fluid. Such a fluid features a binodal for sufficiently large attractive interactions  $\beta\epsilon$  and we expect from the discussion of the additivity constraint for  $\Omega[S]$  in Section 3.1 that morphometry of thermodynamic quantities is only fulfilled if neither wetting nor drying occurs. In order to study this, we consider a square-well fluid with a fixed potential width  $R_\epsilon = 2R$  and variable  $\beta\epsilon$ , i.e. variable temperature or potential depth respectively. The bulk density of the fluid will be held constant at  $\eta = 0.3$ . For the bulk fluid we show the corresponding phase diagram in Fig. 1.1. The line with the

arrow-head marks the thermodynamic states of the fluid under consideration when the potential depth  $\beta\epsilon$  is varied. The bulk fluid is brought in contact with a spherical hard wall of radius  $R_S$ . For sufficiently negative  $\beta\epsilon$  drying occurs, i.e. a film of finite thickness and reduced density wets the hard spherical wall. The quantitative extend of this effect is strongly influenced by the shape of the wall. It has been shown that there are non-analytical contributions to all thermodynamic quantities [40]. However, for sufficient “distance”  $\delta\mu$  from phase coexistence, no drying occurs and we therefore expect that the morphometric arguments are valid. In order to test this we consider an expansion of the contact density  $\bar{\rho}^c$  in powers of the inverse radius  $R_S$

$$\bar{\rho}^c = \sum_{i=0} \rho^{(i)} \left( \frac{R}{R_S + R} \right)^i, \quad (3.19)$$

where  $\rho^{(i)}$  ( $i = 0, 1, \dots$ ) are expansion coefficients. If the morphometric form of  $\bar{\rho}^c$  is fulfilled,  $\rho^{(i)}$  must be zero for all  $i \geq 3$ . We display our result in Fig. 3.14 for various values of the potential depth  $\beta\epsilon$ .

It can be seen that the morphometric arguments are valid for a large interval of  $\epsilon$ , however close to the binodal the prediction fails due to drying. Evans *et. al.* introduced a length scale  $R_c$  that determines the crossover from analytic to non-analytic behavior of thermodynamic quantities [53]. They derived that

$$R_c = \frac{2\gamma_{gl}^\infty}{\Delta\rho \delta\mu}, \quad (3.20)$$

where  $\gamma_{gl}^\infty$  is the interfacial tension of the free planar interface,  $\Delta\rho = \rho_{liquid} - \rho_{gas}$  the difference in the bulk densities of the coexisting phases, and  $\delta\mu$  the distance of the state of the fluid to the binodal. In order to obtain the coefficients for the expansion in Eq. (3.19) we use DFT data of spherical walls with  $R_S \geq 100R$ . We expect non-morphometric behavior when  $R_c$  is larger than the smallest radius  $R_S$  used. The system under consideration approaches the binodal along the path shown in Fig. 1.1 with a constant bulk packing fraction  $\eta = 0.3$ . Given these figures, the crossover radius  $R_c$  exceeds  $100R_S$  for  $|\beta\epsilon - \beta\epsilon_{gl}| < 0.00343$ , where  $\beta\epsilon_{gl} = -0.96557$  is the perturbation parameter for which a fluid phase with  $\eta = 0.3$  coexists with a gas phase. The right end of the range where non-analytic terms dominate the system is shown in Fig. 3.14 as a vertical dotted line and approximately determines the interval where  $\rho^{(3)}$  is larger than the other expansion coefficients. This is an indirect observation for non-analytic behavior of the contact density. The morphometric form can only be applied if the radii of curvatures are large compared to  $R_c$ .

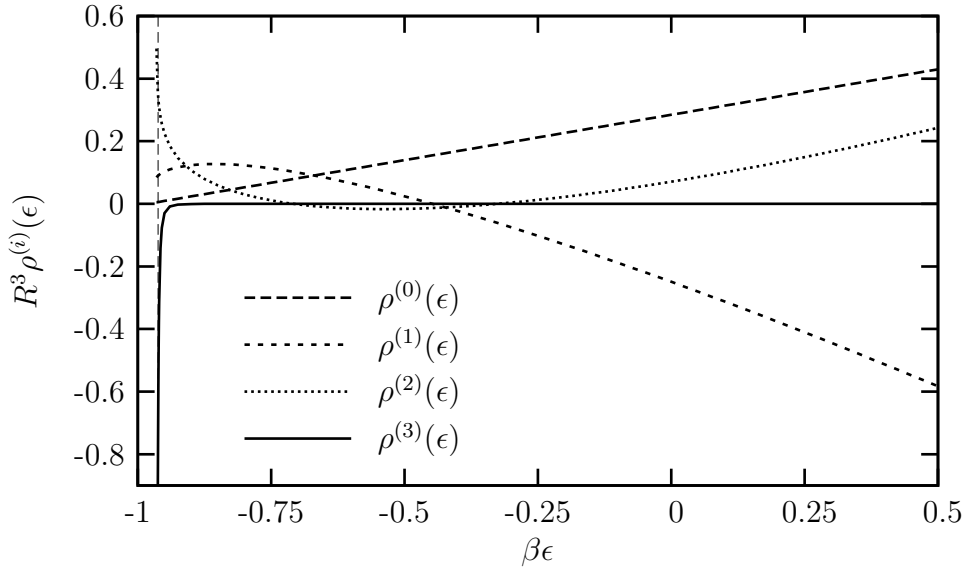


Figure 3.14: Radius expansion of the contact density of a square well fluid adsorbed at a hard spherical wall according to Eq. (3.19). The expansion is performed for various well-depths  $\epsilon$  with constant  $R_\epsilon/R = 2$  and  $\eta = 0.3$ . For sufficient separation from the binodal at  $\beta\epsilon_{gl} = -0.96557$ , the coefficient  $\rho^{(3)}$  vanished numerically as expected by virtue of morphometric arguments. This is in contrast to the behavior close to phase separation where  $\rho^{(3)}$  increases sharply. The vertical dashed line estimates the crossover to non-analytical behavior of the contact density according to Eq. (3.20).

We also verified that the breakdown of the morphometric form does not occur when the binodal is approached from the gas-phase. In this case neither drying nor wetting occurs and the contact density  $\bar{\rho}^c$  has a morphometric form even very close to phase coexistence. This shows that the morphometric arguments do not necessarily fail near a two-phase region, their breakdown is rather due to the long-ranged parallel correlations associated with drying or wetting [53].

### 3.4 Summary

We showed numerical evidence that the thermodynamic quantities as obtained by direct DFT calculations can be very accurately predicted using a morphometric form. Obviously DFT calculations yield a grand potential that is consistent with the three restrictions we impose on an extensive quantity. It is however important that this result is not an artifact of the approximations involved in the density functionals we



use. Although the bulk theory for FMT-based functionals predicts a morphometric  $\Omega$  it is important to realize that by a minimization of the density functional the resulting thermodynamical quantities can deviate significantly from predictions based on underlying bulk theories [50, 40, 61]. To completely rule out that the morphometric form of  $\Omega$  is implied by the use of FMT-based functionals we verified our conjecture additionally by using the Tarazona Mark I functional [60], which has a completely different structure. For this functional we also find an agreement with the morphometric prediction.

Furthermore we verified the predictions of the morphometric forms with quasi-exact simulation data - both globally and locally. In particular the morphometric predictions based on the White-Bear version of FMT provide an excellent description of the average contact density for various complex objects. The local form of the morphometric prediction constitutes a good approximation when the lateral variations of curvatures are small.

The morphometric form of  $\Omega$  is not an artifact of the pure hard interactions. We verified that thermodynamic quantities of a hard-sphere fluid in contact with a wall with a *soft* potential also have a morphometric form. Non-morphometric terms in the full curvature expansion are numerically zero for various parameters of the wall-particle potential. This behavior of thermodynamic quantities is distinctively different to the contact density which loses its direct connection to the grand potential when a non-zero soft tail is added to the wall-particle potential. In this situation it cannot be considered as a thermodynamic quantity any more. Consequently, non-morphometric terms contribute to the curvature dependence of  $\bar{\rho}^c$ .

We also studied a square-well fluid at a hard wall. The interparticle interaction has a hard core but additionally a *soft* contribution. The thermodynamic quantities are found to have a morphometric form, as long as no drying occurs. In the latter case, the full curvature expansion in terms of powers of the curvatures  $H$  and  $K$  is not an appropriate description of the influence of the shape of the wall. Non-analytic contributions become significant and yield a more complex curvature dependence.

These results are relevant because the expansion of thermodynamic quantities in powers of the curvatures is a commonly used approach to treat the influence of curvature on interfaces. For example, the well-established Helfrich Hamiltonian [56] uses  $H$  and  $K$  to empirically quantify the energy cost for bending of an interface and is in agreement with our ansatz on a length scale larger than the persistence length of the interface. Furthermore the idea that the grand potential depends solely on four fundamental measures [62] has been successfully applied in the context of

porous media [63, 64, 65, 66], biological cells [67], or to predict phase diagrams of complex fluids such as microemulsions [68].

# Chapter 4

## Shape Dependence of Density Profiles

In the previous Chapter 3 we study how interfacial properties are influenced by the shape of a wall and find morphometric forms for thermodynamic quantities. It is common to all thermodynamic quantities that they are *averaged* over the surface of the wall, i.e. they are of particular interest when one is interested in a thermodynamic description of the wall-fluid interface as a whole. In contrast to this we study in this chapter the influence of curvatures on a *local* quantity, namely the density of particles at a given point  $\mathbf{r}$  outside a hard wall. Similar as in the case for thermodynamic quantities, the density distribution  $\rho(\mathbf{r})$  around highly symmetric walls can usually be found efficiently using conventional numerical approaches, but little is known concerning the density distribution of fluid particles around more complexly shaped objects. Such an information is however very useful as it is connected to other interesting structural properties of the fluid such as correlation functions or depletion potentials between two complexly shaped particles.

In the first section we introduce the concept of a curvature expansion of the density profile, which describes the influence of the local curvatures on the density. It enables us, based on the accurate knowledge of the density profiles of a hard-sphere fluid in *simple* geometries, to accurately predict density distributions around complexly shaped objects. This includes in particular the contact density, for which we already found a morphometric form in Section 3.2. Other thermodynamic quantities can also be derived from the curvature expansion of the density profile and we elucidate the connection of the curvature expansion to morphometry in the second section. Finally, in section three, we present a general theory for the asymptotic form of

density profiles in a fluid at arbitrarily shaped walls. This furthermore substantiates our curvature expansion approach and provides some deep insight concerning the influence of geometry on the decay of correlation functions.

## 4.1 Curvature Expansion of the Density Profile

The morphometric form of *thermodynamic* quantities predicts a curvature dependence that is at most linear in the mean and Gaussian curvature  $H$  and  $K$ . This is a peculiar feature of these quantities and we cannot expect that such a remarkably simple dependence is sufficient for the density profile to fully describe the influence of a curved wall. As an indication of this fact we quote the results presented in Section 3.3.4, where the contact density at a hard-core wall with a *soft* potential loses its direct connection to the grand potential  $\Omega$  and hence gains a curvature dependence which must be described by a infinite curvature expansion which includes also higher powers in  $H$  and  $K$ . We apply this concept of a full curvature expansion also to the density profile  $\rho(\mathbf{r})$ .

To this end we consider a big hard particle as a wall for the surrounding fluid and introduce the normal coordinates generated by its effective surface [69, 70], see Fig. 4.1. With these definitions we write for the curvature dependence of the density profile

$$\begin{aligned} \rho(\mathbf{r}) = & \rho_P(u) + \rho_H(u)H + \rho_K(u)K + \rho_{H^2}(u)H^2 + \\ & + \rho_{H^3}(u)H^3 + \rho_{HK}(u)HK + \mathcal{O}(R_{1,2}^{-4}), \end{aligned} \quad (4.1)$$

where  $\rho_P(u)$  is the density profile at a planar wall and  $\rho_\xi(u)$  for  $\xi = H, K, H^2, H^3, HK, \dots$  are expansion coefficient functions. These functions are intensive. They depend in general on the type of fluid, its temperature and thermodynamic state and on the wall-fluid interaction potential, but are independent of the shape of the wall described by  $H$  and  $K$ . Note that there are infinitely many expansion coefficients because the density at an arbitrary normal distance  $u$  is not a thermodynamic quantity in the sense we define in Sec. 3.1. There are two fundamental assumptions involved in Eq. (4.1). The first is that the density  $\rho(\mathbf{r})$  is only influenced by the *local* properties of the wall, which are described by the local mean and local Gaussian curvature. Therefore the curvature expansion assumes that the lateral variations of  $H$  and  $K$  can be neglected and we therefore expect that it is best fulfilled for surfaces with slowly varying curvatures. The second assumption is that the density profile can be *analytically* expanded around the planar density profile. This assumption is

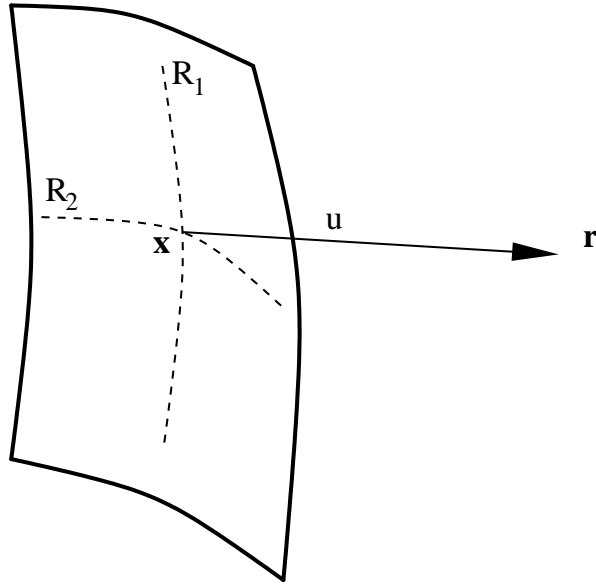


Figure 4.1: Normal coordinates generated by a segment of a convex wall. Any point  $\mathbf{r}$  outside the wall can be reached starting from  $\mathbf{x}$ , the point closest to  $\mathbf{r}$  on the surface. The difference vector  $\mathbf{r} - \mathbf{x}$  is parallel to the local surface normal  $\mathbf{n}(\mathbf{x})$  at position  $\mathbf{x}$  and we denote  $u = |\mathbf{r} - \mathbf{x}|$  as the normal distance of  $\mathbf{r}$ . The principal radii of curvature of the wall at  $\mathbf{x}$  are  $R_1$  and  $R_2$ , the local mean curvature  $H(\mathbf{x}) = (R/R_1 + R/R_2)/2$  and the Gaussian curvature  $K(\mathbf{x}) = R^2/(R_1 R_2)$ . For more details see Appendix A.

non-trivial as we point out in Section 4.2. It can however be motivated by the finding for thermodynamic quantities in section 3.1, which feature an analytic dependence on  $H$  and  $K$ . As however already mentioned there it is known that e.g. drying destroys the analytic behavior of the contact density [53]. We therefore restrict the application of the curvature expansion to systems with a morphometric grand potential.

In analogy to the morphometric ansatz, Eq. (3.3), the curvature expansion of the density profile as shown in Eq. (4.1) multiplicatively separates geometric and fluid properties. Therefore the problem of obtaining the density profiles around complexly shaped objects is shifted to the problem of determining the coefficient functions  $\rho_\xi(u)$ . In order to demonstrate the practicability of our ansatz we study a fluid of hard spheres with radius  $R$  in contact with a hard wall. For each normal distance  $u$ , we analyze the dependence of the density  $\rho(u)$  of the fluid at a cylindrical and a spherical wall and evaluate the coefficient functions  $\rho_\xi(u)$  as described in Appendix B. The results are shown in Fig. 4.2.

Note that, with the knowledge of the density profile around cylindrical and spher-

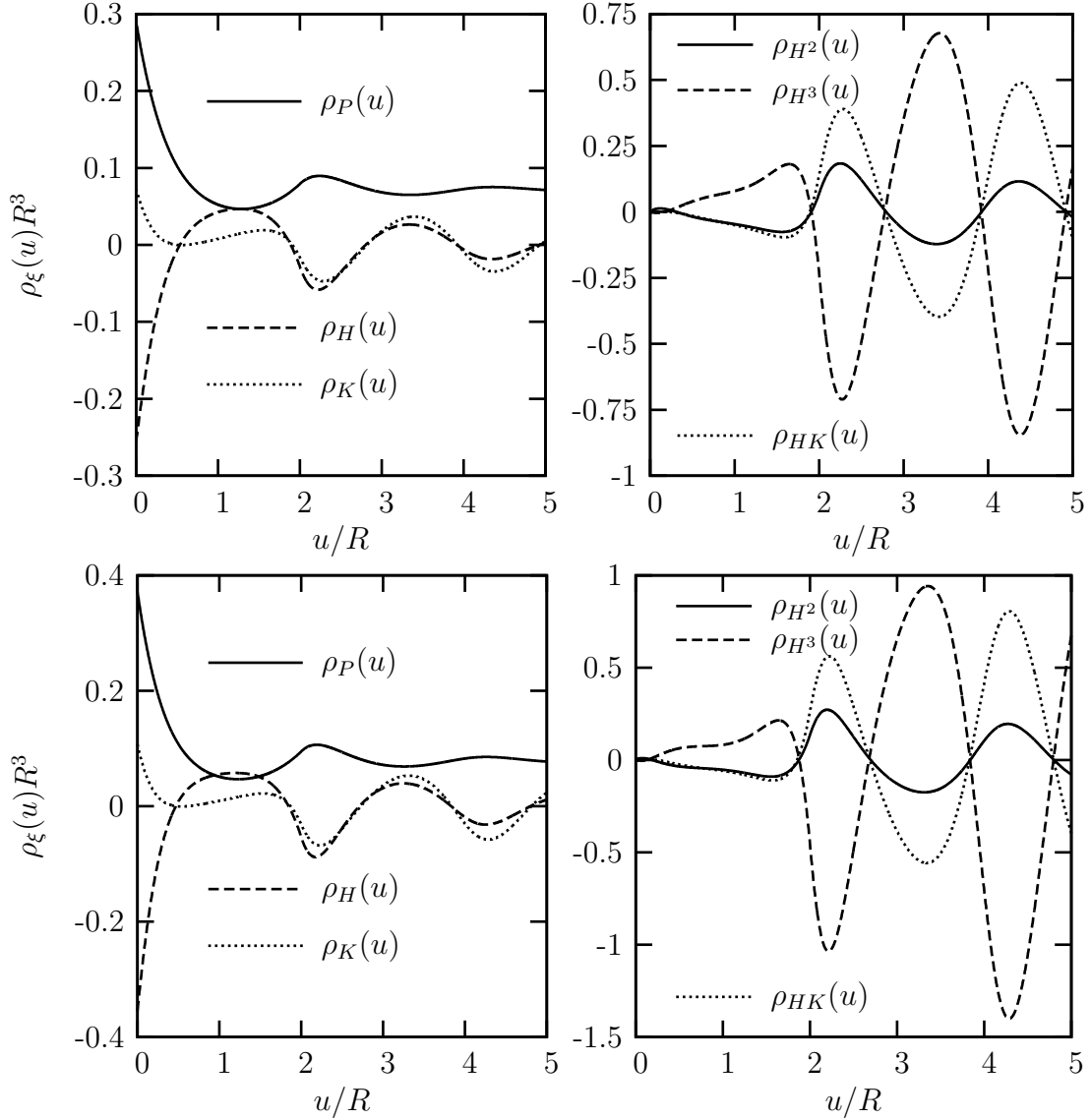


Figure 4.2: Typical curvature expansion coefficient functions  $\rho_\xi(u)$  as defined in Eq. (4.1). The upper two figures show the results for the original Rosenfeld functional and a bulk packing fraction of  $\eta = 0.3$ , the lower to show results for the White-Bear version of FMT and a higher bulk packing fraction of  $\eta = 0.3314$ . For this system we compare DFT results with MC data in Fig. 4.3. Common to the coefficient functions  $\rho_\xi(u)$  in the left column with  $\xi = P, H, K$  is the finite contact value for  $u = 0$ , which is in contrast to the functions in the right column with  $\xi = H^2, H^3, HK$ . We verified that this behavior and the characteristic oscillatory structure is also observed for other bulk packing fractions  $\eta$  and elucidate this issue in detail in Sections 4.2 and 4.3.

ical walls, the curvature expansion coefficient functions can only be determined up to the third order in the inverse radii of curvature (see Appendix B). For higher order coefficient functions, the accurate knowledge of density profiles around more complexly shaped walls would be needed, which is normally not available. For this practical reason we truncate the curvature expansion after the third order terms and use only the terms that are explicitly shown in Eq. (4.1). In contrast to thermodynamic quantities, where higher order terms vanish and thus a truncation does not represent a problem, the situation for the density profile is different. The neglected terms inevitably lead to an error which is the largest when the absolute value of the curvatures  $H$  and  $K$  are large. This is not a conceptual problem but due to practical limitations and we restrict the application of the curvature expansion to walls with small  $H$  and  $K$ . This corresponds to objects which are large compared to the particles in the surrounding fluid.

We test the practicability of the ansatz in Eq. (4.1) by considering a hard-sphere fluid in contact with a prolate ellipsoidal wall a half axes  $(4, 4, 10)R$ . We compare MC simulation data and the results of the curvature expansion. From the simulation we determined the bulk packing fraction of the small spheres to be  $\eta = 0.3314$  and already verified in Section 3.3.2 that the contact density  $\rho^c = \rho(u)|_{u=0}$  can be predicted very accurately by means of a morphometric expansion, as displayed in Fig. 3.6. The full curvature expansion reproduces these results for  $u = 0$ , as it also includes “morphometric” terms proportional to  $H$  and  $K$ . Hence it is a more stringent test for the curvature expansion to predict the density profile for all  $u$ , because this requires also the knowledge of higher order coefficient functions  $\rho_\xi(u)$ ,  $\xi = H^2, H^3, HK, \dots$ . Selected typical cuts through the density profile are shown in Fig. 4.3.

Within the error bars of the simulation the agreement between the prediction of the curvature expansion and the direct simulation data is excellent for all values of  $u$  and  $\theta$ . For  $\theta = 0$  the curvatures are the largest for a prolate ellipsoid, see Fig. 3.5. Note that at this position the Jacobi determinant close to the surface is very small and therefore the statistics is relatively poor. We verified that the higher order coefficient functions contribute to the density profile and it is not sufficient to consider only the “morphometric” terms  $\rho_P(u)$ ,  $\rho_H(u)$ , and  $\rho_K(u)$ .

We also analyzed the density profile around the shrunk ellipsoid and the spherocylinder as obtained by the simulation presented in Section 3.3.2. As expected from the analysis of the contact density in Section 3.3.2 we find a very good agreement between simulation data and curvature expansion as long as the influence of lateral variations in the curvatures can be neglected. We therefore conclude that the curva-

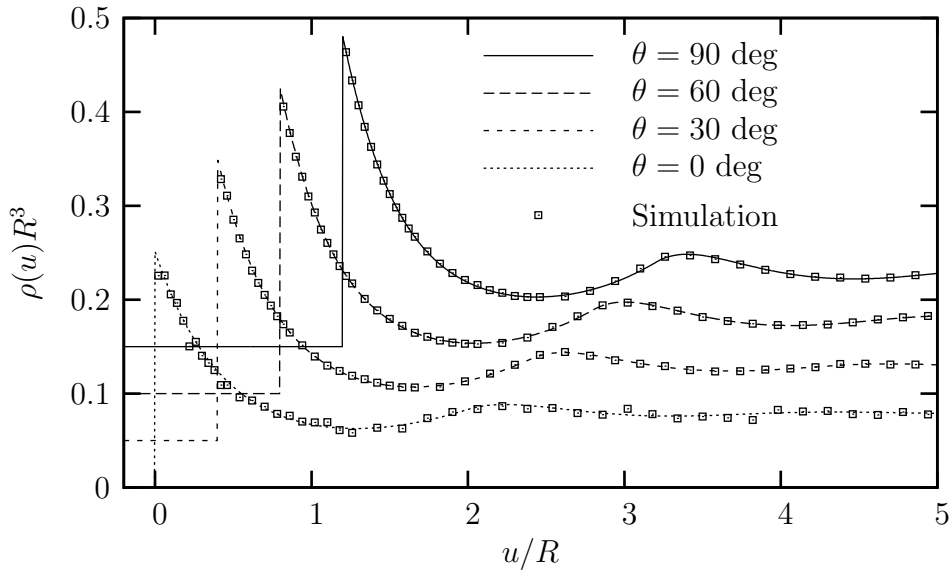


Figure 4.3: Cuts through the density profile  $\rho(\mathbf{r})$  of a fluid of hard spheres with radius  $R$  around a biaxial ellipsoid with half axes  $(4, 4, 10)R$  [58]. The bulk packing fraction is  $\eta = 0.3314$ . We show the density along paths that start perpendicular from the effective surface of ellipsoid, which we parameterize by  $\theta$  and  $\phi$  [see Eq. (A.21)]. The normal coordinate  $u$  denotes the distance to the effective wall. Monte-Carlo results (symbols) are compared with the results of the curvature expansion, Eq. (4.1), based on data obtained from the White-Bear version of FMT (lines). We already verified the accurate prediction of the contact density ( $u = 0$ ) in Fig. 3.6. The agreement shown here is typical also for other cuts through the density profile.

ture expansion of the density profile represents a good approximation to the actual density profile if the curvatures  $H$  and  $K$  are small and vary slowly along the surface.

## 4.2 Implications

By using the curvature expansion approach presented in the previous section it is possible to determine the density distributions around complexly shaped interfaces and with this knowledge, in a second step, thermodynamic quantities associated with the interface can be obtained. These thermodynamic quantities have, as we discuss in Chapter 3, a morphometric form which represents a more restricted dependence on the shape of the wall than a full curvature expansion. We show in this section that the morphometric form of thermodynamic quantities is not a priori implied by



the full curvature expansion of the density profile, Eq. (4.1), and hence the expansion coefficient functions  $\rho_\xi(u)$  must satisfy sum-rules that ensure that the derived thermodynamic quantities are morphometric.

The most obvious connection between the curvature expansion and the morphometric approach is obtained by noting that the curvature expansion coefficients functions  $\rho_\xi(u)$  at  $u = 0$  are identical to the expansion coefficients  $\rho_\xi^c$  used in Eq. (3.17) for a full curvature expansion of the contact density  $\rho^c$ . We showed numerically in this context that  $\rho_\xi^c \approx 0$  for all  $\xi = H^2, HK, H^3$ , as predicted by the morphometric form. This result can also be observed in Fig. 4.2, where the higher order expansion coefficients in the right column vanish numerically for  $u = 0$ . This is in contrast to other normal distances  $u$ , where the higher order expansion functions contribute to the density  $\rho(\mathbf{r})$ . It is particularly striking that the non-morphometric term  $\rho_{H^2}(u)$  vanishes for  $u \rightarrow 0$  while the morphometric term  $\rho_K(u)$  does not, although both feature a quadratic dependence on the principal curvatures and are of the same order of magnitude for other values of  $u$ .

Another prediction of the morphometric ansatz for  $\Omega$  is that the excess adsorption  $\Gamma$  is a morphometric quantity. The excess adsorption is defined in Eq. (2.1) and can be calculated using for the density profile  $\rho(\mathbf{r})$  the curvature expansion formula provided by Eq. (4.1). Assuming a constant  $H = \bar{H}$  and  $K = \bar{K}$  we obtain

$$\Gamma = \int du (1 + 2Hu + Ku^2) \cdot \left( \rho_P(u) - \rho_b + \sum_{\xi} \rho_\xi(u) \xi \right). \quad (4.2)$$

The factor  $(1 + 2Hu + Ku^2) = J(u)$  represents the Jacobi determinant of the normal coordinate system generated by the effective wall. By comparing the two expressions for  $\Gamma$  in Eq. (3.5) and Eq. (4.2) we find that the following integrals must vanish

$$\begin{aligned} \int du (2u\rho_H(u) + \rho_{H^2}(u)) &= 0, \\ \int du (2u\rho_{H^2}(u) + \rho_{H^3}(u)) &= 0, \\ \int du (2u\rho_K(u) + u^2\rho_H(u) + \rho_{HK}(u)) &= 0. \end{aligned} \quad (4.3)$$

There are in principle further restrictions for higher order coefficients  $\rho_\xi(u)$ . They however involve expansion coefficients that are not accessible by our numerical data analysis and we therefore do not consider them here. We verify that all integrals in Eq. (4.3) vanish for various bulk packing fractions and different DFT models for the hard-sphere fluid. We furthermore found that Eqs. 4.3 are *not* fulfilled because the

integrands vanish for all  $u$ , which would represent an even stronger restriction for the coefficient functions. Note that the conditions presented in Eq. (4.3) are necessary to obtain a morphometric form for the excess adsorption  $\Gamma$ , what we already verified in Section 3.3.

The richest set of restrictions on the coefficients functions is obtained by considering the sum rule in Eq. (2.11), which relates a local quantity, the contact density  $\bar{\rho}^c$ , to a global quantity, the excess adsorption  $\Gamma$ . For a spherical wall the sum rule was already analyzed in Ref. [53], here however we generalize the arguments to arbitrarily shaped hard walls. By inserting the curvature expansion of the density profile, Eq. (4.1) in the sum-rule, we find by comparing the terms with the same powers in  $\bar{H}$  and  $\bar{K}$  that

$$\partial\bar{\rho}_P^c/\partial\beta\mu = \rho_b, \quad (4.4)$$

$$\partial\bar{\rho}_H^c/\partial\beta\mu = -2\Gamma_P, \quad (4.5)$$

$$\partial\bar{\rho}_K^c/\partial\beta\mu = -\Gamma_H, \quad (4.6)$$

$$\partial\bar{\rho}_{H^2}^c/\partial\beta\mu = 0, \quad (4.7)$$

$$\partial\bar{\rho}_{H^3}^c/\partial\beta\mu = 2\Gamma_{H^2}, \quad (4.8)$$

$$\partial\bar{\rho}_{HK}^c/\partial\beta\mu = -2\Gamma_{H^2}, \quad (4.9)$$

$$\partial\bar{\rho}_{H^4}^c/\partial\beta\mu = 4\Gamma_{H^3}, \quad (4.10)$$

$$\partial\bar{\rho}_{H^2K}^c/\partial\beta\mu = 2\Gamma_{HK} - 3\Gamma_{H^3}, \quad (4.11)$$

$$\partial\bar{\rho}_{K^2}^c/\partial\beta\mu = -\Gamma_{HK}. \quad (4.12)$$

These differential equations are valid for all fluids in contact with a hard wall provided that an analytic curvature expansion of  $\bar{\rho}^c$  and  $\Gamma$  exists. The first relation, Eq. (4.4), can be rewritten using the result of the planar hard wall contact theorem which states that  $\bar{\rho}_P^c = \beta p$ . This yields  $\partial p/\partial\mu = \rho_b$ , which follows also from the Gibbs-Duhem relation and is hence fulfilled by all numerical approaches which are consistent with thermodynamics. The relation in Eq. (4.5) is identical to the Gibbs adsorption theorem, Eq. (2.3), provided one identifies  $\bar{\rho}_H^c$  with the planar surface tension  $\beta\gamma$ . We do this in the morphometric ansatz, which hence fulfills Eq. (4.5). It is also in agreement with Eq. (4.6) as we use  $\bar{\rho}_K^c = \beta\kappa$  and  $\Gamma_H = -\partial\kappa/\partial\mu$  in the respective morphometric forms (3.6) and (3.5).

A very remarkable relation is obtained from the differential equation (4.7). As it is valid for all values of  $\mu$ , one can integrate it with respect to  $\mu$ . We use as a starting condition that  $\bar{\rho}_{H^2}^c = 0$  for  $\mu \rightarrow -\infty$ , which means  $\rho_b \rightarrow 0$ . According to this rigorous argument we obtain  $\bar{\rho}_{H^2}^c = 0$ . This result agrees with the findings of Stillinger and

Cotter in Ref. [57], where they used SPT arguments to analyze molecular distribution functions. It is furthermore implied by the morphometric form of the contact density, Eq. (3.6) and therefore furthermore substantiates the approach presented in Section 3. Note that this relation is fulfilled for *all* fluids that allow a curvature expansion of the density profile, i.e. for which one can write down an analytic expansion of the density profile in terms of the curvatures of the wall. This class of fluids is very large, however we already pointed out that e.g. wetting or drying layers at a wall destroy the analytic form of curvature expansion of thermodynamic quantities and consequently also of the density profile [53].

All further relations, Eqs. (4.8) - (4.12) are trivially fulfilled by the morphometric approach that states  $\bar{\rho}_\xi^c = 0 = \Gamma_\xi$  for all  $\xi = H^2, H^3, HK, \dots$ . However, the vanishing of these higher order expansion coefficients is not *implied* by the existence of the curvature expansion. By adding Eqs. (4.8) and (4.9) and integrating the result with respect to  $\mu$  we merely find that  $\bar{\rho}_{HK}^c = -\bar{\rho}_{H^3}^c$ . This result is nonetheless useful in a spherical geometry, where  $HK = H^3 = (R/(R + R_S))^3$ . It states that the third order term in a power-series expansion of the contact density in  $R/(R + R_S)$  vanishes for all fluids that allow an analytic curvature expansion. This result was derived earlier not assuming any morphometric arguments for the special case of a pure hard-sphere fluid in the limit of small curvatures [71] and generalized later to arbitrary fluids in Ref. [57]. Similarly, by combining Eqs. (4.10), (4.11), and (4.12), we derive that  $8\bar{\rho}_{K^2}^c + 4\bar{\rho}_{H^2K}^c + 3\bar{\rho}_{H^4}^c = 0$  for all  $\mu$  and  $\beta$ .

### 4.3 Asymptotic Form of Density Profiles

One of the striking features of the curvature expansion coefficient functions  $\rho_\xi(u)$  is that they all seem to oscillate around common zeros. These zeros seem to coincide with those of  $\rho_P(u) - \rho_b$ . As far as the curvature expansion ansatz in Eq. (4.1) is concerned this would imply that there is a set of normal distances  $u$  where the density  $\rho(u) = \rho_b$ . This set of values for  $u$  would be independent of  $H$  and  $K$ , i.e. the same for differently shaped walls. This is indeed approximately the case, large normal distances from the wall. We discuss this so-called asymptotic limit by analytic means later in this section. In order to show the accuracy of our assumption, we consider a fluid of hard spheres with radius  $R$  in contact with a big sphere of radius  $R_S$ . By means of DFT calculations we obtain for each  $R_S$  a density profile  $\rho(u)$  and label the normal positions where  $\rho(u) = \rho_b$  as  $u_n(R_S)$ , where  $n = 1, 2, \dots$  labels the index of the zero. Figure 4.4 shows the positions  $u_n(R_S)$  at the spherical wall relative to the

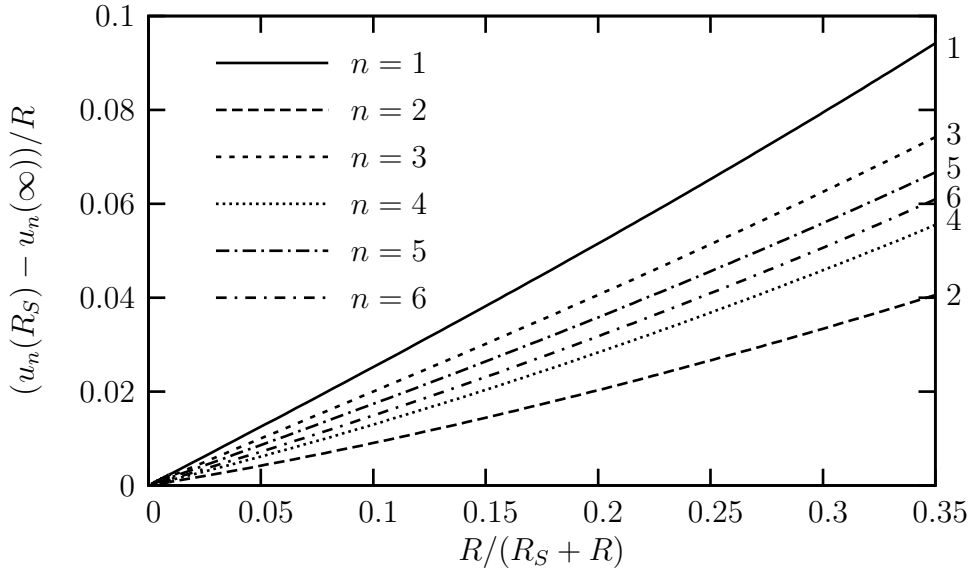


Figure 4.4: Deviation of the normal position of the zeros  $u_n(R_S)$  of a density profile  $\rho(u) - \rho_b = 0$  at a hard spherical wall to the positions  $u_n(\infty)$  of a profile at a planar wall. The results are obtained for a hard-sphere fluid modeled via the Rosenfeld functional with a packing fraction  $\eta = 0.3$ . We verified that the White-Bear functional gives similar results and that all deviations have the same sign, i.e. the position  $u_n(R_S) \geq u_n(\infty)$  for all  $n$ . The deviations for small index  $n$  depend on  $R_S$  in a complicated manner, however for large index  $n$  the deviations can be described by a single curve which means that all zeros are shifted by the same amount as compared to the zeros of the planar density profile. The absolute value of the shift depends on the bulk packing fraction  $\eta$ .

positions  $u_n(\infty)$  at a planar wall.

The assumption that all curvature expansion coefficient functions  $\rho_\xi(u)$  have the same zeros implies that  $\rho(u) - \rho_b = 0$  is fulfilled for the same  $u_n(R_S)$  independent of  $R_S$ . In this case all functions shown in Fig. 4.4 must vanish. This is obviously not strictly the case. Note however that it represents a relatively good approximation as the absolute values for the deviations shown in Fig. 4.4 are small compared to the wavelength of the oscillations in the density profile  $\rho(u)$ . The latter equals approximately  $2R$  for the hard-sphere fluid. Therefore the approximation that the zeros are at the same positions for all  $R_S$  is fulfilled with a relatively good accuracy. Furthermore, for large  $n$ , the deviations  $u_n(R_S) - u_n(\infty)$  fall on the same curve. This means that for large normal distance  $u$  all zeros are shifted by the same small distance, which weakly depends on the radius of curvature  $R_S$ . We discuss this point

further in this section below. Under the approximation that all curvature expansion coefficient functions have common zeros we write as an ansatz

$$\rho_\xi(u) = (\rho_P(u) - \rho_b) \cdot f_\xi(u), \quad (4.13)$$

where  $\rho_P(u)$  is the density profile at a planar wall. The first factor in Eq. (4.13) is responsible for the oscillations and the exponential decay of the expansion functions  $\rho_\xi(u)$  while the newly defined function  $f_\xi(u)$  in the second factor is a non-oscillatory function and describes the variation of the amplitude of the respective curvature expansion function  $\rho_\xi(u)$ . It turns out later in our analysis that the functions  $f_\xi(u)$  are *independent* of the bulk packing fraction and the fluid, i.e. they are purely defined by geometric means. What does this imply? We can use the curvature expansion of the density profile, Eq. (4.1) and insert Eq. (4.13) as an ansatz for  $\rho_\xi(u)$  which yields

$$\rho(\mathbf{r}) = \rho_b + (\rho_P(u) - \rho_b) \cdot \left( 1 + \sum_{\xi} f_\xi(u) \xi \right). \quad (4.14)$$

This equation suggests that the geometric functions  $f_\xi(u)$  and the density profile at a *planar* wall are sufficient to calculate the density profile around even complexly shaped objects. This is indeed possible, however only accurately in the asymptotic limit. This limit is characterized by a large normal distance  $u$  from the wall. The meaning of “large” normal distance is discussed in more detail below.

The geometric coefficients can in principle be determined from numerical data, however their functional form can also be analytically obtained using the Ornstein-Zernike equation [13, 72]. For this we follow some arguments of the general theory of the asymptotic decay [73, 74, 75, 76, 77] and consider a general fluid with short-ranged interactions and an isotropic bulk phase. This excludes for instance fluids that feature a spontaneous symmetry breaking as it occurs e.g. in nematic phases. If the bulk phase is isotropic, the particle-particle direct correlation function  $c_{pp}(\mathbf{r})$  depends only on the mutual distance of the centers of two particles, which is essential for the following derivation.

We consider a mixture of fluid particles (labeled  $p$ ) with an additional component  $w$ , which constitutes the wall. We are interested in the total correlation function  $h_{wp}(\mathbf{r})$  between a wall-particle  $w$  and a fluid particle  $p$ . This correlation function is connected to the density distribution  $\rho(\mathbf{r})$  of fluid particles around the wall via  $h_{wp}(\mathbf{r}) = (\rho(\mathbf{r}) - \rho_b) / \rho_b$ . In order to suppress wall-wall correlations we consider the dilute limit of component  $w$ , i.e. a bulk density of wall particles  $\rho_w \rightarrow 0$ . The bulk density  $\rho_b$  of the fluid particles is kept constant at a non-zero value. We describe this

quasi two-component bulk mixture by use of the Ornstein-Zernike equation,

$$h_{ij}(\mathbf{r}) = c_{ij}(\mathbf{r}) + \sum_k \rho_k \int c_{ik}(\mathbf{r}') h_{kj}(\mathbf{r}' - \mathbf{r}) d\mathbf{r}', \quad (4.15)$$

where  $c$  denotes the direct and  $h$  the total correlation function. The indices  $i, j$ , and  $k$  label the different components  $i, j, k \in p, w$ . The integral is a three-dimensional convolution which suggest to solve Eq. (4.15) in Fourier space. Taking the explicit limit  $\rho_w \rightarrow 0$  we find formally for the Fourier transformed of  $h_{wp}$

$$\hat{h}_{wp}(\mathbf{k}) = \frac{\hat{c}_{wp}(\mathbf{k})}{(1 - \rho_p \hat{c}_{pp}(\mathbf{k}))}. \quad (4.16)$$

Here, the hat denotes the respective Fourier transforms of the correlation functions. By providing explicit analytical expressions for the Fourier transforms of the two direct correlation functions  $\hat{c}_{wp}$  and  $\hat{c}_{pp}$ , Eq. (4.16) can in principle be solved. However, in particular for  $c_{wp}$ , no closed analytical expression is known. To proceed, we transform Eq. (4.16) back to real space and use the Fourier representation of  $\hat{c}_{wp}(\mathbf{k})$ ,  $\hat{c}_{wp}(\mathbf{k}) \propto \int d\mathbf{r}' c_{wp}(\mathbf{r}') \exp(-i\mathbf{k} \cdot \mathbf{r}')$ . This transforms Eq. (4.16) to

$$h_{wp}(\mathbf{r}) \propto \int d\mathbf{r}' c_{wp}(\mathbf{r}') \underbrace{\int d\mathbf{k} \frac{e^{i\mathbf{k} \cdot (\mathbf{r} - \mathbf{r}')}}{1 - \rho_p c_{pp}(\mathbf{k})}}_{G(\mathbf{r} - \mathbf{r}')}, \quad (4.17)$$

where the overall constant proportionality factor is not important for this analysis and is therefore suppressed. This equation shows that in real space  $h_{wp} = c_{wp} * G$ , where  $G$  can be interpreted as a Greens function of a certain linear differential operator, which will be determined later. Here we simplify  $G(\mathbf{r} - \mathbf{r}')$  further by using that for an isotropic bulk phase  $c_{pp}(\mathbf{k}) = c_{pp}(|\mathbf{k}|)$ . Defining  $s = |\mathbf{r} - \mathbf{r}'|$  and introducing spherical coordinates for  $\mathbf{k}$  leads us to a spherically symmetric Greens function  $G(\mathbf{r} - \mathbf{r}') = G(s)$ , where

$$G(s) \propto \frac{1}{s} \int_0^\infty dk \frac{k \sin(ks)}{1 - \rho_p c_{pp}(k)}. \quad (4.18)$$

We extend the integration to a closed contour in the complex plane and apply the residue theorem. Note that for short-ranged interactions the positions of *all* poles with finite  $k$  are given by the complex zeros of the denominator  $1 - \rho_p c_{pp}(k)$  [78]. Each pole with position  $k$  contributes to the total correlation function a term proportional to  $\exp(iku)$ , i.e. an oscillation that is exponentially damped. An analogue argument holds also for the more general case of polydisperse particles  $p$ , where the denominator is a lengthy expression but analogously yields a set of zeros which contribute to the total pair correlation function [79, 80].

No assumptions have been made so far, except of the applicability of the bulk Ornstein-Zernike equations, Eq. (4.15) and the assumption that the interactions in the fluid are short-ranged. Now however we employ the asymptotic limit. This means that we consider  $s = |\mathbf{s}|$  to be sufficiently large in the sense that the contributions of all poles except the one of the leading order pole at position  $k_0$  can be neglected [81, 74, 82, 80]. This can be done as the contributions of all other poles decay exponentially on a shorter length scale than the contributions of the leading order pole. The decay length of the contributions of each pole is determined by the inverse of the imaginary part of the position of the pole. Therefore, the pole with the smallest imaginary part dominates for large values of  $s$ . Experience tells the asymptotic regime sets in already for relatively small values of  $s$ , in particular in the case of a monodisperse hard-sphere fluid. With this assumption, Eq. (4.18) simplifies from a sum over all poles to a single term

$$G(s) \propto \frac{k_0}{s} \sin(k_0 s), \quad (4.19)$$

where the residue of the leading order pole is, being a constant with respect to  $s$ , absorbed in the proportionality factor. At this point we come back to the interpretation of  $G(s)$  as a Greens function. The same Greens function  $G$  as in Eq. (4.19) is found for the  $\phi^2$ -model with the Lagrangian  $\mathcal{L} = (\nabla\phi)^2 + k_0^2\phi^2$  which has the extremal condition  $(\Delta + k_0^2)\phi = 0$ . Both for the Ornstein-Zernike equation and for the  $\phi^2$ -model the complex scalar  $1/k_0$  is interpreted as a (complex) correlation length which determines the wave- and decay length of total correlation functions and other structural properties of the fluids. Therefore, to “leading order pole approximation”, the solution Eq. (4.17) of the Ornstein-Zernike equation is equivalent to the solution of the linear differential equation

$$(\Delta + k_0^2)h_{wp}(\mathbf{r}) = c_{wp}(\mathbf{r}). \quad (4.20)$$

Note that the equation does not explicitly contain  $c_{pp}(\mathbf{r})$ . Its properties enter only implicitly through the position of the leading order pole  $k_0$ . We continue to analyze the asymptotic decay of  $h_{wp}$  further and assume that  $\mathbf{r}$  is sufficiently far away from the wall such that the inhomogeneity of the differential equation (4.20) vanishes, i.e.  $c_{wp}(\mathbf{r}) = 0$ . One can show with the help of a cluster expansion that for large  $|\mathbf{r}|$   $c_{wp}(\mathbf{r}) \approx -\beta V_{wp}(\mathbf{r})$ , where  $\beta V_{wp}(\mathbf{r})$  denotes the wall-particle interaction potential. In the asymptotic limit,  $\mathbf{r}$  lies far outside the wall, such that a neglect of  $c_{wp}(\mathbf{r})$  represents a very good approximation for walls with an interaction potential that decays fast. Note that this in particular includes hard walls. For the next step we

introduce normal coordinates [see Eq. (A.17)] and assume a multiplicative separation of the total correlation function  $h_{wp}(\mathbf{r}) = h(\alpha, \beta)h(u)$ . Using  $\Delta = J(u)^{-1}\partial_u J(u)\partial_u$  for the  $u$ -coordinate and the Jacobi-determinant  $J(u) = 1 + 2Hu + Ku^2$  [see Eq. (A.13)] yields for the  $u$ -dependence  $h(u)$  of  $h_{wp}(\mathbf{r})$

$$\frac{1}{J(u)}\partial_u J(u)\partial_u h(u) + k_0^2 h(u) = 0. \quad (4.21)$$

This differential equation can be simplified using the ansatz  $h(u) = f(u)/\sqrt{J(u)}$

$$\partial_u^2 f(u) + \underbrace{\left(k_0^2 + \frac{H^2 - K}{J(u)^2}\right)}_{\mathcal{O}(u^{-4})} f(u) = 0. \quad (4.22)$$

The solution of this differential equation gives the exact functional form of the correlation function in the asymptotic limit. Unfortunately, for general  $J(u)$ , Eq. (4.22) cannot be solved in closed form. Nonetheless, for particular choices of  $H$  and  $K$ , Eq. (4.22) can be integrated. These are planar, cylindrical, or spherical walls. For other geometric setups, Eq. (4.22) must either be solved numerically or approximated by neglecting the underbraced term which, for large  $u$ , decays as  $1/u^4$  for nonzero<sup>1</sup> Gaussian curvature  $K$ . With this approximation the solution of the differential equation Eq. (4.22) is  $f(u) \propto \exp(ik_0 u)$ , which eventually leads to the final expression for  $h(u)$  for the limit of large  $u$

$$h(u) \propto \frac{\exp(ik_0 u)}{\sqrt{J(u)}}. \quad (4.23)$$

The asymptotic functional form of the correlation function is therefore given by an exponentially damped oscillation according to the real and imaginary part of the position  $k_0$  of the leading order pole and a purely geometrical factor, which becomes  $1/\sqrt{J(u)}$  for large values of  $u$ . This geometrical factor is independent of the type of fluid, as long as it features an isotropic bulk phase and short-ranged interaction potentials. However in order to fully obtain the asymptotic form of the correlation function, the proportionality factor in Eq. (4.23) must be determined. It is in principle given by the properties of the direct wall-particle correlation function  $c_{wp}(\mathbf{r})$  according to Eq. (4.20). Unfortunately, in case of a generally shaped wall, no closed expressions for  $c_{wp}(\mathbf{r})$  are known. We therefore write

$$h_{wp}(u) = \frac{A \exp(-i\Im(k_0)u) \sin(\Re(k_0)u + \theta)}{\sqrt{J(u)}}, \quad (4.24)$$

<sup>1</sup>This excludes cylinders, which are inventions of the devil [78].



where the denominator denotes the asymptotic decay of the correlation function at a planar wall. The amplitude  $A$  and the phase  $\theta$  do not depend on the normal distance  $u$  and are determined by the direct wall-particle correlation function  $c_{wp}(\mathbf{r})$  and the value of  $k_0$ . We find numerically for a hard-sphere fluid that they depend strongly on the bulk density  $\rho_b$ , but only weakly on the shape of the wall. It would be interesting to study this issue in more detail, for this thesis however we assume that  $A$  and  $\theta$  are constants of the curvatures  $H$  and  $K$ .

This assumption provides us with an analytic expression for the correlation function in the asymptotic limit, Eq. (4.24). Hence we obtain the density profiles of a fluid around an arbitrary wall for large  $u$  via

$$\rho(\mathbf{r}) = \rho_b + (\rho_P(u) - \rho_b)/\sqrt{J(u)}, \quad J(u) = 1 + 2Hu + Ku^2. \quad (4.25)$$

This equation is very remarkable. It allows to determine the asymptotic form of density profiles around *arbitrarily* shaped convex walls based on the knowledge of the density profile  $\rho_P(u)$  at a planar wall. The latter is normally relatively easy to obtain by numeric means. Equation (4.25) also implies that the positions of the zeros  $u_n(R_S)$  shown in Fig. 4.4 are independent of  $H$  and  $K$ , which we find to be approximately fulfilled.

With the knowledge of an analytic expression for the asymptotic form of density profile we can find the asymptotic form of curvature expansion coefficients by expanding Eq. (4.25) in a power series in terms of both  $H$  and  $K$ . The convergence and the implications of such an expansion are discussed below, here we merely note that all resulting curvature expansion coefficient functions  $\rho_\xi(u)$  for  $\xi = H, K, H^2, \dots$  are products, as we guessed in Eq. (4.13)

$$\rho_\xi(u) = (\rho_P(u) - \rho_b)f_\xi(u). \quad (4.26)$$

The first factor on the right hand side,  $(\rho_P(u) - \rho_b)$ , is determined exclusively by the properties of the fluid at a planar wall, while the second factor  $f_\xi(u)$  for  $\xi = H, K, H^2, \dots$  stems from the series expansion of  $1/\sqrt{J(u)}$  and is thus the same for all thermodynamic states and all types of fluids. The geometric factors  $f_\xi(u)$  are therefore determined by purely geometric considerations. The lowest order factors  $f_\xi(u)$  can be written as

$$\begin{aligned} f_H(u) &= -u, \\ f_K(u) &= -u^2/2, \quad f_{H^2}(u) = 3u^2/2, \\ f_{H^3}(u) &= -5u^3/2, \quad f_{HK}(u) = 3u^3/2. \end{aligned} \quad (4.27)$$

We test Eq. (4.26) and the functions shown in Eq. (4.27) by considering the expansion coefficients which we obtained for a hard-sphere fluid. The results are shown in Fig. 4.5.

The multiplicative decomposition between fluid properties and geometry, Eq. (4.26) is indeed valid for a hard-sphere fluid, in particular the zeros of the expansion functions  $\rho_\xi(u)$  are all nearly at the same position in the asymptotic limit. The agreement to the analytically predicted geometric coefficient functions in Eq. (4.27) is excellent.

We study the convergence of the curvature expansion by using the approximate expressions for  $\rho_\xi(u)$  as provided by Eq. (4.26). These are in very good agreement to the actual coefficient functions for large  $u$  (see Fig. 4.5). From dimensional considerations we find for the higher order expansion coefficients that  $\rho_\xi(u) \propto (\rho_P(u) - \rho_b)u^{a+2b}$  what raises the question whether the convergence of the curvature expansion series is assured also for large  $u$ . Higher order coefficient functions for  $a, b \gg 1$  become very large. Luckily, despite of the increase of the powers in  $u$ , the curvature expansion coefficient functions  $\rho_\xi(u)$  as a whole always converge by virtue of the *exponential* decay of  $(\rho_P(u) - \rho_b) \propto h_P(u)$ , see Eq. (4.23). Therefore the correct bulk properties are always recovered for  $u \rightarrow \infty$ . However the functional form of the decay is not reproduced correctly. The reason for this is that for *very* large distances  $u$  all walls look either like a plane ( $H = 0 = K$ ), a line ( $K = 0$ ), or a point. These three different “topologies” result in density profiles that decay asymptotically according to Eq. (4.25) as

$$\rho(u) - \rho_b \propto \exp(ik_0u) \left\{ \begin{array}{l} 1 \\ \sqrt{1/u} \\ 1/u \end{array} \right\}. \quad (4.28)$$

The curvature expansion series, which always includes the density profile at a planar wall as the lowest order term, can therefore not reproduce the asymptotic decay of the latter two topologies. The curvature expansion should consequently only be used in an intermediate range where  $u$  is smaller than the typical size of the wall object. If one is interested in large- $u$  behavior, one should use Eq. (4.25) instead of the curvature expansion. Note that for most practical purposes these issues should not represent a problem, as the for large values of the normal distance  $u$  the density profile can be replaced by the bulk density very accurately.

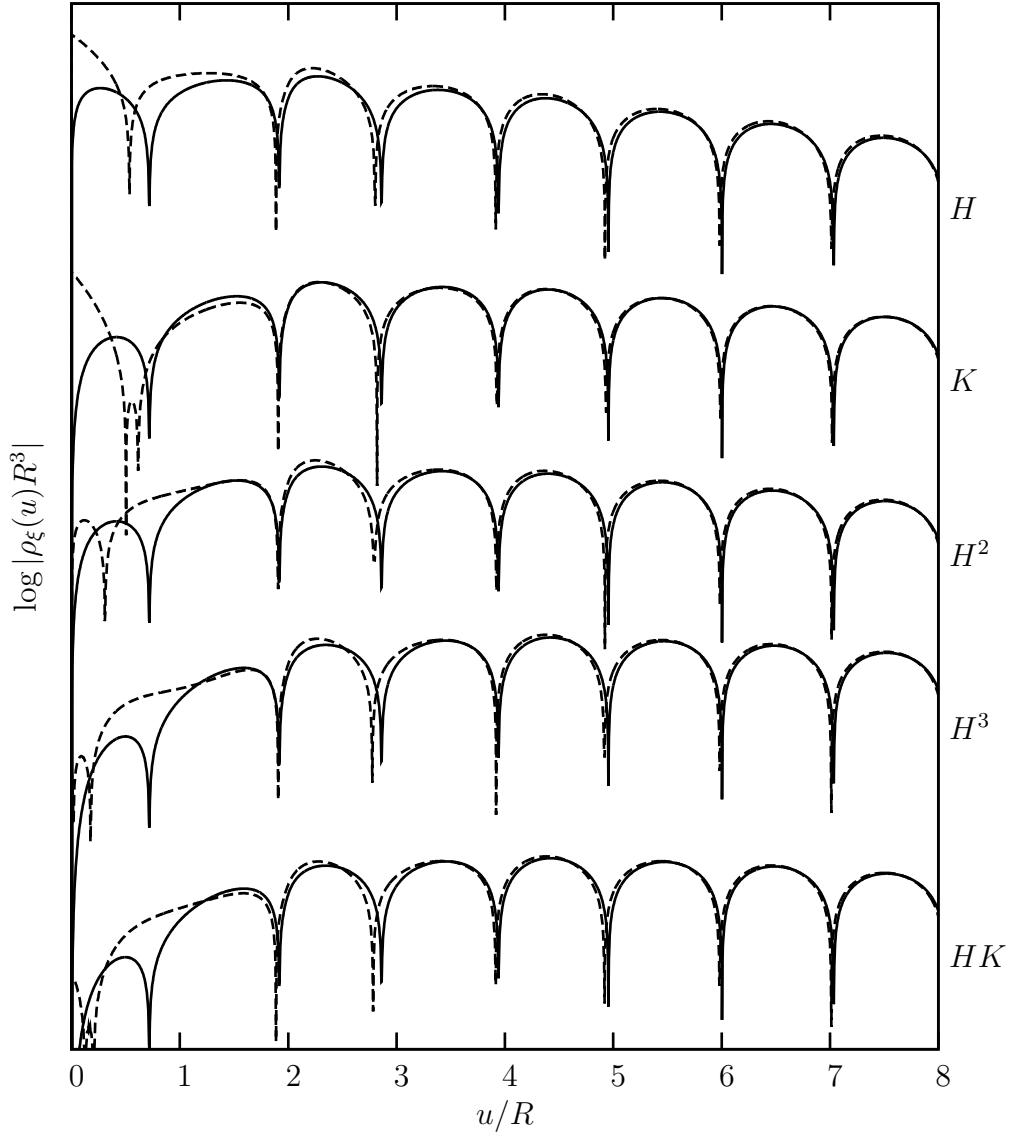


Figure 4.5: Curvature expansion coefficient functions  $\rho_\xi(u)$  for various  $\xi$  in a logarithmic plot. For large  $u$ , the agreement between the prediction based on the asymptotic theory (full line) agrees perfectly with the numerical results based on DFT (dashed line). The plot shows results for a hard sphere fluid with a bulk packing fraction of  $\eta = 0.3$  modeled via the original Rosenfeld functional. We verified that other bulk packing fractions and the White-Bear version of FMT give similar results. The signs of the functions in Eq. (4.27), which cannot be observed in this plot, are also correctly predicted, what can be verified in Fig. 4.2.

# Chapter 5

## Depletion Potentials

Depletion potentials arise when two big colloidal particles are immersed in a fluid of smaller particles. In such a situation it is often favorable to describe the behavior of the big particles using an effective picture, where the internal degrees of freedom of the small particles are integrated out and the big particles interact via an effective two-body potential. In the case of big hard particles, the two-body interaction potential is called depletion potential as it can be associated with the depletion of the excluded volume around two big colloidal particles [7]. Such an effective picture is very useful from a practical point of view. It allows for example to understand the phase behavior and the structure of asymmetric colloidal mixtures [83, 82, 84, 85]. Furthermore, effective potentials play an important role in biophysical processes, which are often controlled by the interaction between involved macromolecules [1, 2, 3]. Considering that the cytoplasm of a cell is a densely packed suspension of other molecules and ions [86, 87, 88, 89, 90], any realistic description of the behavior of big macromolecules must necessarily include the effects due to the presence of other particles in a cell.

A versatile method to calculate depletion potentials within FMT-based DFT is developed in Ref. [47]. This theory uses the equilibrium density distribution of small particles around one big particle and then inserts a second big particle in order to obtain the mutual depletion potential. It has been successfully applied to systems where the big particles are either planar walls or spheres [44, 48, 91, 92, 93, 47]. More recent works obtain depletion interactions also if one of the big objects has a more complex shape [94, 95, 96]. Common to these studied geometric setups is that at least one of the objects is sufficiently simple such that the calculation of the density distribution of small particles around it can be done by means of direct DFT techniques. We are however interested in biological key-lock systems, which

are characterized by the property that both the key and the lock particle are too complexly shaped to apply standard DFT methods directly. One way to proceed would be the use of more approximate theories and large-scale computer calculations. Kinoshita *et. al.* for example solved integral equations on a three-dimensional cubic grid in order to obtain depletion potentials between discs, rectangular solids and a simple key-lock systems [2, 97, 3].

In this chapter we however follow the approach developed in Ref. [47] and combine it with the curvature expansion technique we present in the previous section. This allows us to efficiently obtain depletion potentials between arbitrarily shaped big objects. In the first section of this chapter we present our approach in detail. Then, in section two, we test the accuracy of the involved curvature expansion by considering the depletion interaction between a sphere and a biaxial ellipsoid. The results displayed there support our approach and show that it is very accurate provided that the lateral variations of the curvatures of one big object are small. Section three generalizes the approach to account also for depletion interactions between two convex, nonspherical particles. We present depletion potentials and depletion torques between two ellipsoids immersed in a sea of hard spheres. Finally, in section four, a simple model for a biological key-lock system is proposed and the influence of the depletion interaction concerning the bonding of key and lock particle is discussed.

## 5.1 Preparatory Considerations

Depletion potentials can be calculated within the framework of DFT using the insertion method [47] reviewed in Section 1.4. According to this theory, the total change of the grand potential  $\Omega[\rho]$  upon adding one big particle  $B$  into an inhomogeneous fluid of small particles is given for an FMT-based functional by

$$c_B^{(1)}(\mathbf{r}) = - \sum_{\alpha} \int \frac{\partial \beta \phi}{\partial n_{\alpha}}(\mathbf{r}') w_B^{(\alpha)}(\mathbf{r} - \mathbf{r}') d\mathbf{r}'. \quad (5.1)$$

In this equation,  $c_B^{(1)}(\mathbf{r})$  denotes the one-body direct correlation function of the inserted big particle for an equilibrated density distribution of the depletion agent (small particles) around the fixed big particle. The sum on the right hand side of Eq. (5.1) extends over all weight functions  $w_B^{(\alpha)}(\mathbf{r})$  of the big particle, i.e.  $\alpha = 0, 1, 2, 3, \mathbf{1}, \mathbf{2}$ .  $\phi = \phi(\{n(\mathbf{r})\})$  denotes the excess free energy density as provided by an FMT functional. The actual depletion potential  $W(\mathbf{r})$  is defined as the amount of free energy associated with moving the second big particle from an infinite separation to a finite

position  $\mathbf{r}$  relative to the first particle. It is the energy difference between a configuration where a big particle is added at infinite position and configuration where it is added at position  $\mathbf{r}$ . According to Eq. (5.1) this energy is given by a difference of direct correlation functions

$$-\beta W(\mathbf{r}) = \lim_{\rho_B \rightarrow 0} \left( c_B^{(1)}(\mathbf{r}) - c_B^{(1)}(\infty) \right). \quad (5.2)$$

Note that the depletion potential is defined in the absence of other big particles, the so-called dilute limit, where the bulk density  $\rho_B$  of the big particles vanishes. The second term in the definition,  $c_B^{(1)}(\infty)$ , is the energy cost for the insertion of the second particle at infinite separation in a bulk fluid and equals the excess chemical potential  $\mu_{ex,B}$  of particle  $B$  in the dilute limit. If the four morphometric measures of the inserted particle are known, it can be calculated using Eq. (3.9). The inhomogeneous one-body direct correlation function  $c_B^{(1)}(\mathbf{r})$  is more complicated to obtain. Based on the special form of Eq. (5.1), we use for its evaluation a scheme that consists of two steps. First we fix one of the two particles at the origin of the coordinate system and calculate the density profile of the depletion agent around it. From the density profile we derive subsequently the weighted densities and the six fields  $\psi^\alpha(\mathbf{r}) = \partial\beta\phi/\partial n_\alpha(\mathbf{r})$ . Then, in a second step, we “insert” the second big particle in the system at a position  $\mathbf{r}$  and calculate the direct correlation function by evaluating the convolution integrals in Eq. (5.1) and summing all six contributions. It is interesting to note that the influence of both big particles on the depletion potential is separated among the two factors of the convolutions in Eq. (5.1). The fields  $\psi^\alpha(\mathbf{r})$  are, in the dilute limit, exclusively determined by the properties of the first particle while the weight functions  $w_B^\alpha(\mathbf{r})$  are determined by the shape of the second particle only. The fact that each of the convolution factors is influenced only by the properties of one of the two big particles makes Eq. (5.1) very efficient for a numerical evaluation of direct correlation functions.

If the first big particle is not simple, i.e. if it does not have a high spacial symmetry, the density distribution of the depletion agent around it and consequently the fields  $\psi^\alpha(\mathbf{r})$  can for practical reasons not be determined by direct DFT methods. In order to proceed, we use the curvature expansion which we successfully tested for the density profile  $\rho(\mathbf{r})$  in the previous chapter. Instead of using the curvature expansion of the density profile we directly expand all six fields  $\psi^\alpha(\mathbf{r})$  in terms of the curvatures  $H$  and  $K$  of the wall. Unfortunately we can only show for simple walls that the existence of a curvature expansion of the density profile implies also the existence of a curvature expansion for all six fields, however there exists no argument that this is not the case

in general. We additionally verified numerically for simple walls that such a curvature expansion describes the influence of the curved wall on the fields  $\psi^\alpha(\mathbf{r})$  accurately. With this assumption the curvature expansion coefficients can also be used to predict the six fields for various geometric setups. It must however be pointed out that the curvature expansion involves approximations - in analogy to the curvature expansion of the density profile. It considers only the influence of the *local* curvatures and we showed e.g. for the contact density in Fig. 3.7 that this assumption requires smooth lateral variations of curvatures  $H$  and  $K$ . In addition to this approximation the curvature expansion must for practical reasons be truncated after the third order terms, as discussed in Appendix B. For the density profile we show in Fig. 4.3 that the predictions are nonetheless very good if the big object is large. This is the limit we are interested in concerning the depletion potentials in key-lock systems and we therefore expect accurate results using this approach. One additional subtlety which is unique to the curvature expansion of the *fields*  $\psi^\alpha(\mathbf{r})$  is that the vector-valued weight functions  $w_B^\alpha(\mathbf{r})$  for  $\alpha = \mathbf{1}, \mathbf{2}$  are strictly parallel to the surface normal in all simple geometries due to the spacial symmetry of the problem. As we use this data to obtain the curvature expansion coefficients, the curvature expansion technique cannot be used to determine eventual lateral components of the vector-valued  $\psi^{\mathbf{1}}(\mathbf{r})$  or  $\psi^{\mathbf{2}}(\mathbf{r})$ . We therefore assume that these fields are always parallel to the surface normal even for complexly shaped objects. This approximation will be justified numerically in Section 5.2.

Once all six fields are determined, we insert the second particle by evaluating the convolution integrals of the type  $\psi^\alpha(\mathbf{r}) * w_B^\alpha$  for all  $\alpha$  in Eq. (5.1). Formally, these convolutions are all three-dimensional volume integrals, however the special functional form of the weight functions  $w_B^\alpha$  for nonspherical convex particles [see Eq. (1.21)] restricts most of the volume integrals to two-dimensional integrals over the surface of the inserted big particle. Only for  $\alpha = 3$  an actual volume integration must be performed. Concerning the numerical cost of evaluating the integrals, the convolution for  $\alpha = 3$  thus takes by far the longest and therefore determines the time to evaluate a depletion potential.

## 5.2 Spherical-Nonspherical Setup

In this section we calculate the depletion potential between a sphere and a nonspherical particle. We follow the insertion method and fix one of the big particles at the origin and then insert the other particle at position  $\mathbf{r}$ . The result should obviously

not depend on the choice which of the particles has been fixed and therefore there exist two alternative approaches to obtain the mutual depletion potential.

- (1) If the sphere is fixed at the origin one can easily calculate the density distribution of the solvent particles by means of standard DFT techniques because of the high spacial symmetry of the problem. The density profile is therefore known very accurately. This is also the case for the weighted densities and all fields  $\psi^\alpha(\mathbf{r})$  which need to be determined in the first step. We therefore continue with step two and insert the second, nonspherical particle at position  $\mathbf{r}$  in the equilibrated fluid. According to Eq. (5.1) this is done by calculating the convolution integrals with the weight functions of a nonspherical particle as given in Eq. (1.21). Note that, concerning the accuracy of this approach, for the FMT an expression for the decomposition of the Mayer- $f$  bond is used [Eq. (1.10)] which is only exact in the case of two spheres. For nonspherical particles it is approximate and we therefore expect a small systematic error when pursuing this approach.
- (2) For the second approach we fix the nonspherical particle at the origin. The density distribution of small particles around this object is now more complex to obtain, as in general no spacial symmetry can be used and the application of direct methods is not practical any more. As indicated above, we use the curvature expansion to determine the six fields  $\psi^\alpha(\mathbf{r})$  around the fixed particle. This yields accurate results provided that the lateral variations of the curvatures along the surface of the fixed particle are small. We however discussed in the previous section that the curvature expansion leads to small systematic errors. This limitation consequently leads to an error in the depletion potential, which is calculated by the insertion of a sphere at position  $\mathbf{r}$ . Note that in contrast to approach (1), we use the FMT for *spheres* here, which is based on an exact decomposition of the Mayer- $f$  bond. Nonetheless, the result will be affected by the systematic error in the fields  $\psi^\alpha(\mathbf{r})$  due to the curvature expansion.

Both approaches involve a certain approximation - (1) because of the application of FMT to nonspherical objects and (2) because of the curvature expansion of the fields  $\psi^\alpha(\mathbf{r})$ . It is however obvious from general physical consideration that the mutual interaction must not depend on the approach chosen and therefore both (1) and (2) should yield the same result. Due to systematic approximations in both cases we however expect a small discrepancy between both results. It is crucial to note



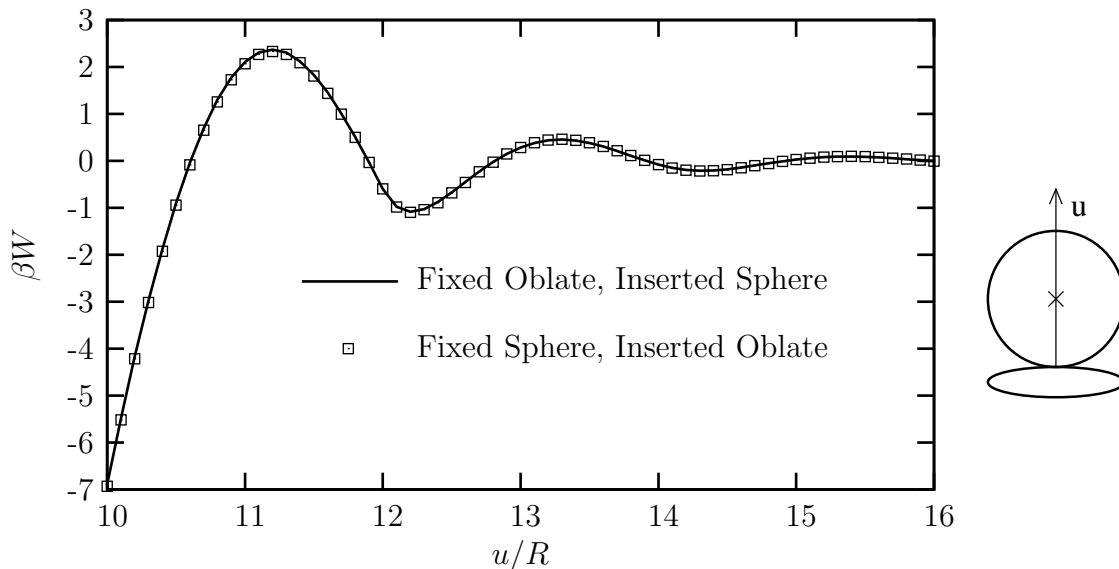


Figure 5.1: Depletion interaction between an oblate ellipsoid with half-axes  $(10, 10, 4)R$  and a sphere with  $R_S = 10R$ . The center of the inserted sphere approaches the north pole of the fixed ellipsoid normal to the surface. Both particles touch if  $u = R_S$ . The symbols denote results obtained by approach (1), for which we employ FMT for convex objects, and the line denotes corresponding results from approach (2), for which we used the curvature expansion. As both approaches involve approximations of very different nature, the excellent agreement is very likely to be due to the fact that the systematic error is very small in both approaches. We verified this observation also for various other setups. For this data the depletion agent is a hard-sphere fluid modeled via the White-Bear version of FMT. The bulk packing fraction is  $\eta = 0.3$ .

that the source of error in both approaches is of a completely different nature and there is no reason that the respective approximations involved in both approaches influence the resulting depletion potential in the same way. Therefore a discrepancy between approach (1) and (2) can be used to quantify the accuracy of the involved approximations. For both approaches we show in Fig. 5.1 the depletion interaction between an oblate ellipsoid and a sphere. Figure 5.2 shows analogue results for a prolate ellipsoid and a sphere. In the latter setup, the involved curvatures are larger.

If the curvatures vary only slowly parallel to the surface the results of the curvature expansion are in excellent agreement with the results using FMT for convex particles, as it can be seen for the oblate setup in Fig. 5.1. For this setup we conclude that both approaches, (1) and (2), yield very accurate results. If however the curvatures

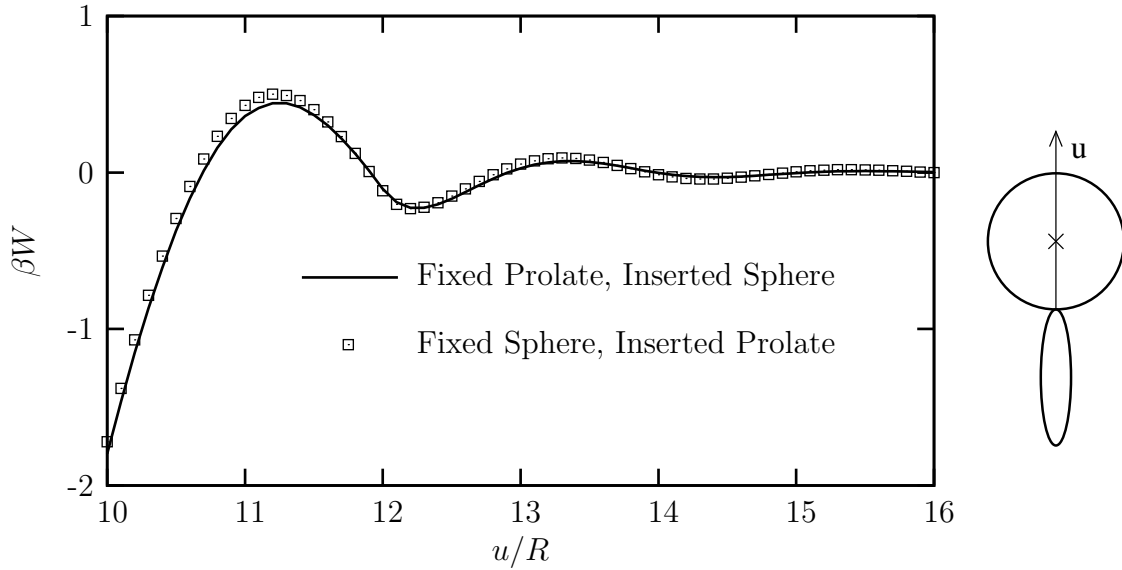


Figure 5.2: Depletion interaction between a prolate ellipsoid with half-axes  $(4, 4, 10)R$  and a sphere with  $R_S = 10R$ . The sphere approaches the north pole of the ellipsoid like in Fig. 5.1. In this geometry, the curvatures are the same as shown in Fig. 3.5. Note that near the north pole at  $\theta = 0$ , the curvatures and additionally the lateral variation of the curvatures along the ellipsoid are relatively high, such that one expects a larger error from the curvature expansion as compared to the oblate setup, Fig. 5.1. A comparison also shows that the contact value and the amplitude of the oscillations of the depletion potential are much smaller.

and their lateral variations are large, as for the prolate ellipsoid used for Fig. 5.2, the results obtained from both approaches differ. This is an indication that the accuracy of at least one approach deteriorates slightly. We know from the curvature expansion of the contact density shown in Fig. 3.7 that lateral effects play an increasing role near the pole of an prolate where the curvatures are the largest and change quickly (see Fig. 3.5). Therefore we expect that also the fields  $\psi^\alpha(\mathbf{r})$  obtained from a curvature expansion are affected by a small systematic error. We verified that the agreement between both methods (1) and (2) is very good if the sphere approaches the prolate on the “flat” side in the symmetry plane where the curvatures and their lateral variations are smaller. We therefore demand that fixed big object must be large compared to the fluid particles in order allow an accurate application of the truncated curvature expansion. Note that this does not restrict the size of the inserted particle, which may be of any size.

If one of the particles is a sphere, there is a third alternative (3) to calculate the depletion potential, namely by a direct curvature expansion of the depletion potential itself. For this we consider the *inserted* big spherical particle as a diluted component of the solute, i.e. a component with a bulk density  $\rho_B \rightarrow 0$ . Although this means that the density profile of big particles  $\rho_B(\mathbf{r})$  also vanishes one can show that the ratio  $\rho_B(\mathbf{r})/\rho_B$  stays finite. It is connected to the depletion potential via

$$\exp(-\beta W(\mathbf{r})) = \lim_{\rho_B \rightarrow 0} \frac{\rho_B(\mathbf{r})}{\rho_B}. \quad (5.3)$$

Assuming that an analytic curvature expansion is possible for the density profile  $\rho_B(\mathbf{r})$  independently of the bulk state of the fluid we find that also  $\exp(-\beta W(\mathbf{r}))$  can be expanded in powers of the curvature. We obtain the respective curvature expansion coefficients by similar means as the coefficients for the density profile by a numerical analysis of the curvature dependence of the depletion potential between a sphere of fixed size and cylindrical or spherical particles of variable size. These potentials can be obtained very accurately using DFT. The numerical analysis is described in Appendix B. With the expansion coefficients we can obtain  $\exp(-\beta W(\mathbf{r}))$  between a sphere of the given radius and an arbitrarily shaped object and consequently also the depletion potential  $\beta W(\mathbf{r})$ . In Fig. 5.3 we use this expansion to calculate the contact value of the depletion potential between an oblate ellipsoid with half-axes (10, 10, 4) and a sphere with radius  $5R$ .

The general agreement between approach (2) and (3) is very good for small  $\theta$  where the curvatures are low for the oblate ellipsoid. This supports our approach. If however  $\theta$  is near 90 deg, the curvatures are maximal and lateral variations become increasingly important. Note that the insertion of a big sphere is done by a three dimensional integration over the fields  $\psi^\alpha(\mathbf{r})$ . The fields must therefore be evaluated for multiple positions  $\mathbf{r}$ , which are reached following the normal from multiple points  $\mathbf{x}$  on the surface of the ellipsoid (see Fig. 4.1). Therefore the integration averages over a finite area on the surface of the ellipsoid such that one can expect that lateral variations influence the curvature expansion of the depletion potential more than it is the case for the density profile of the fields  $\psi^\alpha(\mathbf{r})$ .

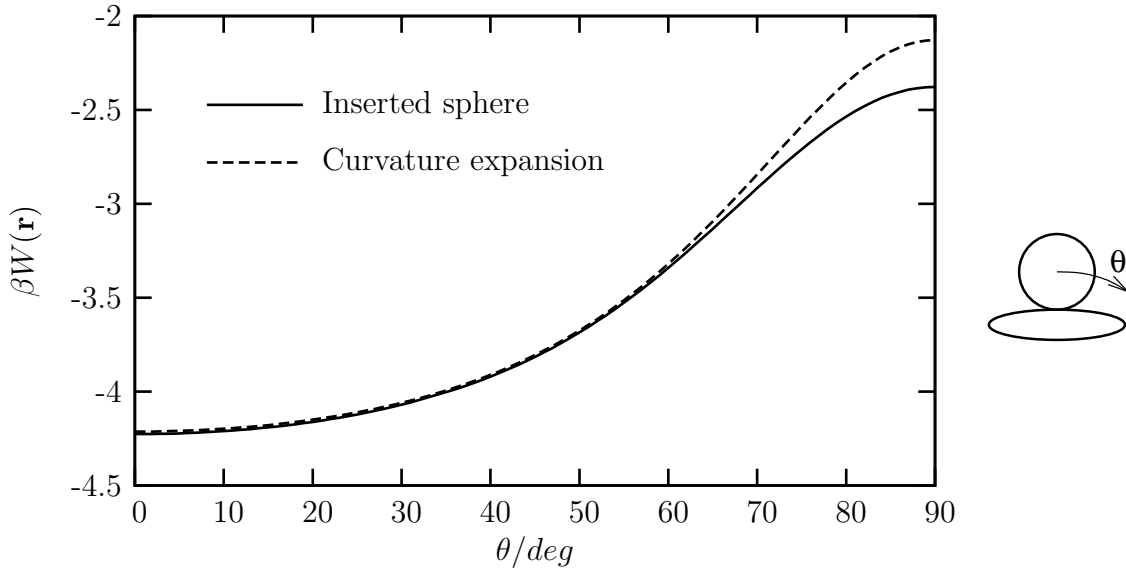


Figure 5.3: Contact density of the depletion potential between an oblate ellipsoid with half-axes  $(10, 10, 4)R$  and a sphere with radius  $R_S = 5$ . Both objects are immersed in a sea of hard spheres with a packing fraction of  $\eta = 0.3$ . The parameter  $\theta$  is one of the normal coordinates of the center of the sphere in the coordinate system generated by the ellipsoid, see Eq. (A.21). The line shows results based on the insertion of a sphere according to approach (2), the dots give the results from a direct curvature expansion, approach (3).

### 5.3 Depletion Potential Between Two Convex Objects

In this section we combine the approximations of approach (1) and (2) which we employ and successfully test in the previous section. This allows us to obtain the depletion potential also between two colloids of arbitrary shape. Unfortunately it is, in contrast to the previous section, not possible for generally shaped objects to independently check the accuracy of the results of our approach, however the agreement between of the two routes as illustrated in Fig. 5.1 shows that the approximations we use are very accurate. We obtain the interaction potential by evaluating the direct correlation function, Eq. (5.1). As described in Section 5.1, we use for the first step the curvature expansion of the fields  $\psi^\alpha(\mathbf{r})$  around the fixed nonspherical object as already employed in approach (2). For the second step we use the insertion of a nonspherical object from approach (1). Both methods have been found to be accurate, provided that the particle which is used for the curvature expansion has curvatures

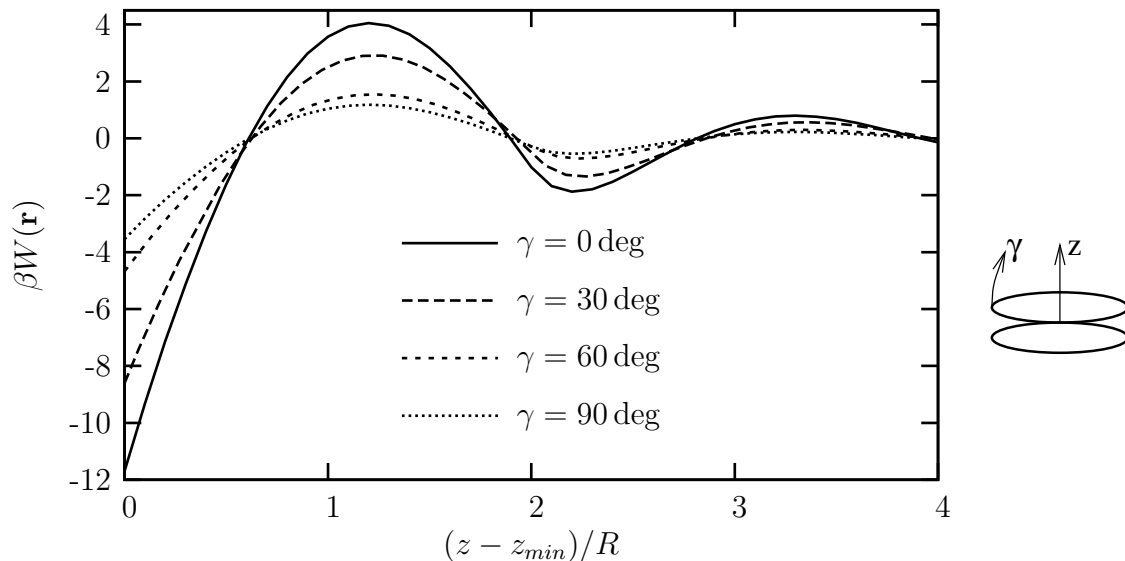


Figure 5.4: Depletion interaction between two oblates with half axes  $(10, 10, 4)R$ . The inserted particle approaches the north pole of the first ellipsoid perpendicular to the surface.  $\gamma$  denotes the angle between the main axes of the two biaxial ellipsoids. If both ellipsoids are aligned, i.e.  $\gamma = 0$ , the minimal separation of the centers is then  $z_{min} = 8R$ , while for  $\gamma = 90$  deg it is  $z_{min} = 14R$ . The solute is a hard-sphere fluid with  $\eta = 0.3$  and is modeled via the White-Bear functional.

which vary smoothly along the surface. For practical purposes we also demand that the particle is large to account for the truncation of the curvature expansion.

With this method it is possible to evaluate depletion potentials between a large class of differently shaped objects and to study the influence of various geometrical parameters on the depletion potential. Additionally, as the loss of symmetry in the problem removes the degeneracy of angular and lateral degrees of freedom, one-dimensional cuts through the depletion potential  $W(\mathbf{r})$  contain only a limited amount of information. We do not want to give a broad overview over depletion potentials between various objects here and therefore limit the presentation to the typical examples shown in Figs. 5.4 and 5.5, where we display depletion potential between two hard oblate ellipsoids immersed in a sea of hard spheres.

The depletion interaction between nonspherical colloid depends not only on the separation of the particles, but also on the mutual orientation. The derivative of the depletion potential with respect to an angular degree of freedom of one particle is referred to as the entropic torque on this particle. In Ref. [96], Roth *et al.* analyzed the torque of a spherocylinder near a planar wall. As the planar wall has a simple geometry, the density profiles and the  $\psi^\alpha(\mathbf{r})$  were obtained without using the ap-

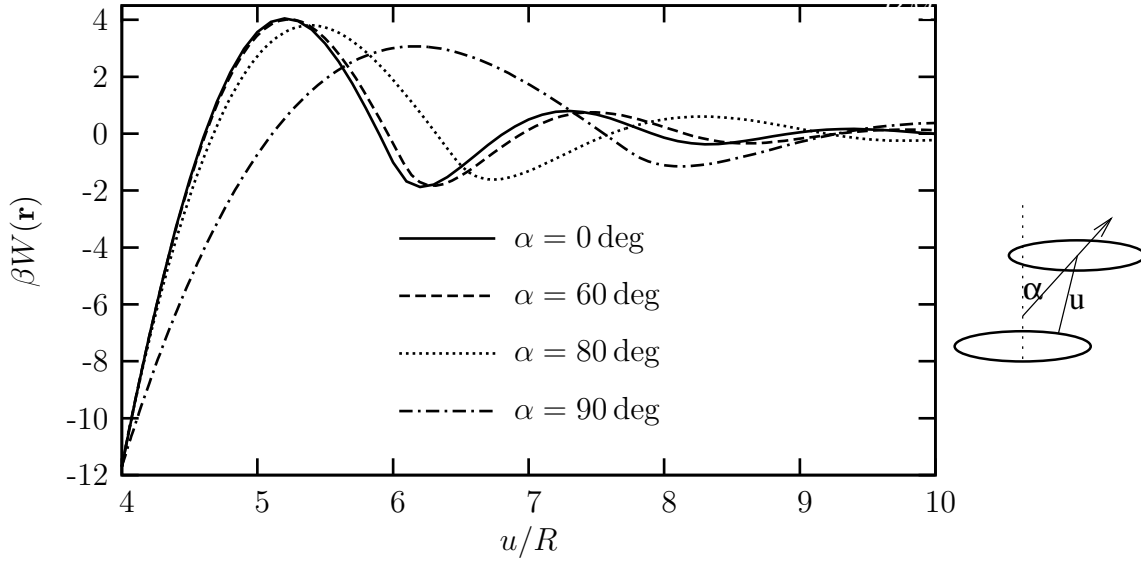


Figure 5.5: Same setup as in Fig. 5.4 with fixed  $\gamma = 0$ . The angle  $\alpha$  parameterizes in what angle the inserted ellipsoid is moved away from its contact position (see sketch to the right hand side). The abscissa shows the normal distance  $u$  of the center of inserted ellipsoid to the surface of the fixed one. For small  $\alpha$  the curves almost coincide due to the oblate shape of the fixed ellipsoid.

proximate curvature expansion. Here we apply the concept of entropic torque to two non-simple objects by using the curvature expansion technique. In Fig. 5.6 we show the entropic torque between two biaxial ellipsoids immersed in a sea of a hard-sphere fluid with  $\eta = 0.3$ .

Due to the symmetry of the problem, the torque  $M$  vanishes always for  $\gamma = 0$  and  $\gamma = 90$  deg. In between these highly symmetric configurations the ellipsoid experiences a torque with alternating signs. If the torque vanishes the system is in a mechanical equilibrium. Note that a stable orientation requires  $\partial^2 W / \partial \gamma^2 > 0$  in addition which means a negative slope of the curves in Fig. 5.6.

## 5.4 Depletion Potential in Key-Lock Systems

We discuss in the introduction of this chapter that a biological cell contains a dense mixture of various macromolecules. The presence of other molecules requires for a realistic model that it includes also the effective interactions between key and lock particles. We present a simple model here, however emphasize that we do *not* aim to model a specific key-lock system very accurately. It is rather interesting to study a

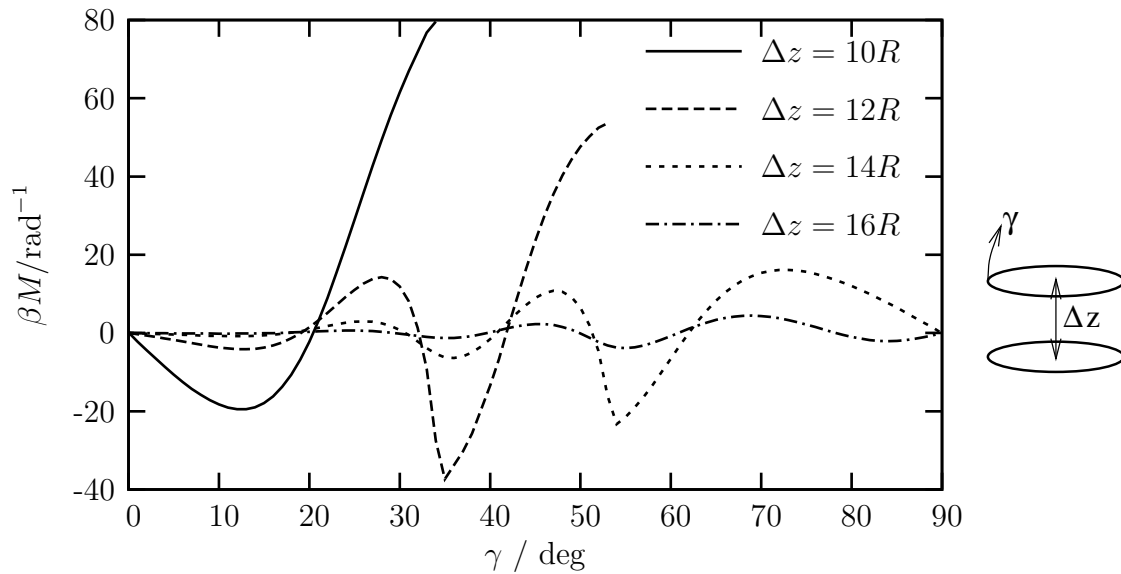


Figure 5.6: Entropic torque between two biaxial ellipsoids with half axes  $(10, 10, 4)R$  as sketched to the right. The angle  $\gamma$  parameterizes the rotation of the inserted ellipsoid and  $\Delta z$  its separation to the fixed ellipsoid. In such a setup an entropic torque  $M$  can be defined via  $M = -\partial W / \partial \gamma$  [96]. If  $\Delta z > 8R$ , the inserted ellipsoid can however be rotated and experiences an entropic torque. Positive values of  $M$  mean that the ellipsoid is pushed clockwise towards larger values of  $\gamma$ . The curves end when the two ellipsoids overlap. Note that the discontinuities in the first derivative of the curves with parameters  $\Delta z = 12R$  and  $\Delta z = 14R$  is not an artifact. They occur when both ellipsoids come so close that only one small sphere with radius  $R$  can be fit in between.

simplified model that still captures the relevant physics of the system. We therefore consider only hard-core interactions here, which brings as an advantage that the findings are not chemically specific, i.e. they apply at least qualitatively to a large class of actual key-lock systems. Furthermore such an approximation is justified by the fact that *intrinsic* interaction potentials are usually shielded on a short lengthscale due to the high physiological salt concentrations in the cytoplasm. We find that geometric aspects of the key and the lock are very important for the role of effective interactions in such systems and we therefore propose a versatile model as sketched in Fig. 5.7.

We calculate depletion potentials between these two objects by determining in a first step the six fields  $\psi^\alpha(\mathbf{r})$  around the lock particle. For this we use the curvature expansion technique that was successfully tested in Secion 5.2 using approach (2).

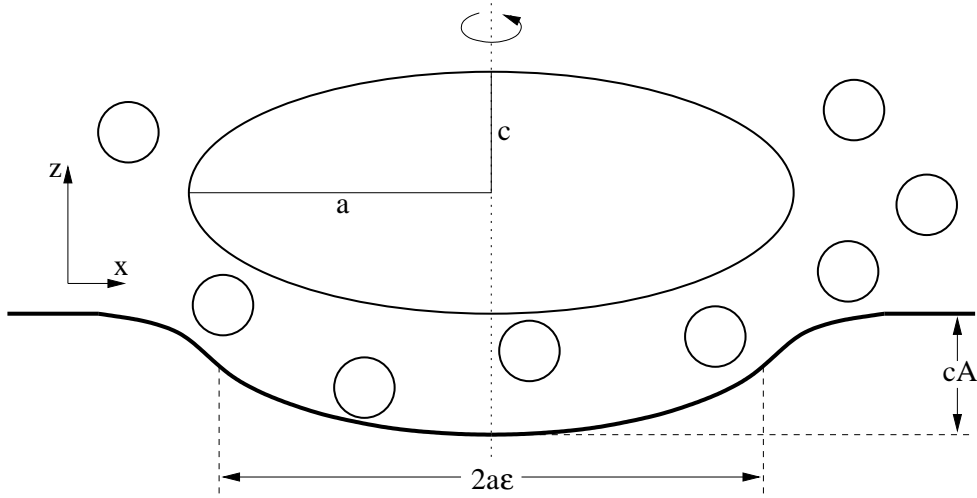


Figure 5.7: A model of a key-lock system. The lock is a hard wall which is rotationally symmetric around the  $z$ -axis. It is constructed in two steps. In the first step a biaxial ellipsoid with half-axes  $(a, a, c)$  is cut out of the half-space  $z \leq 0$ . The center of the ellipsoid is at  $(0, 0, (1 - A)c)$ , where we refer to  $A$  as the penetration parameter which describes the depth of the resulting cavity. Its values range between  $A = 0$  for a planar wall and  $A = 1$  for half an ellipsoid cut out of the half-space. Such a construction would yield a edge. As the curvature expansion cannot be applied to edges, we round them off in a second step. For all  $|x| \geq a\epsilon$  the lock is replaced by a polynomial in  $1/x$  with coefficients such that for  $x = a\epsilon$  the curve and its first and second derivative with respect to  $x$  are continuous. We will set  $\epsilon = 0.9$  unless otherwise stated. For smaller  $|x|$ , the lock keeps its ellipsoidal shape. This yields a smooth surface, in particular the mean and the Gaussian curvature  $H$  and  $K$  depend continuously on the surface. For large  $x$  the surface becomes a planar wall at  $z = 0$ . The other particle, the key, is a biaxial hard ellipsoid given via its half-axes. We parameterize its rotation using the usual three Euler angles. The first, denoted  $\Theta$ , parameterizes a rotation around the  $z$ -Axis. This does not affect the *biaxial* ellipsoid, but rotates the direction of the  $x$ -axis to a new  $x'$ -axis. The second angle  $\Psi$  is used to rotate the object around this new  $x'$ -axis. The third Euler angle, which would rotate the ellipsoid around  $z''$  does not affect the biaxial ellipsoid. It is not considered here. The depletion agent is a fluid of hard spheres with radius  $R$  and a bulk packing fraction  $\eta$  modeled via the White-Bear version of FMT. Note that the sketched walls are hard and considered to be physical walls.



One important difference to the previous geometric setups however is that the lock is partially concave which means that the values of  $H$  or  $K$  may become negative. We however showed in Fig. 3.9 for the contact density  $\bar{\rho}^c$  that results, obtained with the curvature expansion based on results of convex geometries, can also be used for concave systems as long as no caustic effects occur. We expect this analogously also for the fields  $\psi^\alpha(\mathbf{r})$ . To prevent caustic effects we chose the lock large compared to the size of the small hard spheres with radius  $R$ .

Another issue concerning concave walls is that the normal coordinates of some points are not unique, i.e. the same point  $\mathbf{r}$  can be reached starting from multiple points  $\mathbf{x}$  on the surface (see Fig. 4.1). In such a case we chose the point  $\mathbf{x}$  with the minimal normal distance  $u$ , which is usually much smaller than alternative normal distances  $u'$  obtained for a different point  $\mathbf{x}'$ . Our approximation should therefore yield accurate predictions. Only if  $\mathbf{r}$  is at a large normal distance  $u$  to the surface, two or more values for the normal distances may become comparable. This however also does not represent a practical problem, as for these points  $\mathbf{r}$  the fluid assumes bulk properties with high accuracy and the curvature expansion is not needed at all. When all fields  $\psi^\alpha(\mathbf{r})$  can be determined for all positions  $\mathbf{r}$ , we insert the ellipsoidal key-particle as described in Section 5.1 by integrating the convolution integrals between the fields and the fundamental measures  $w_B^{(\alpha)}(\mathbf{r})$  of the inserted ellipsoid.

We begin our study with a system that was proposed as a key-lock system in Ref. [97] and is sketched as setup (a) in Fig. 5.8. It consists of a *spherical* key and a lock, which is a plane with a hemispherical cavity. Note that such a setup features an edge such that the curvature expansion technique cannot be applied. We therefore alter the geometry slightly by considering a system which is sketched as setup (b) in Fig. 5.8. It has a rounded “edge” and is a special case of the more general setup we present in Fig. 5.7. It is designed such that the curvature expansion can be applied for all points  $\mathbf{r}$  and we expect accurate predictions for the six fields  $\psi^\alpha(\mathbf{r})$  if the cavity of the lock is sufficiently large. In order to be able to compare the data with Ref. [97], we consider a lock with a radius of  $5R$  and keys with three different radii  $R_{key}$ . Both are immersed in a hard-sphere fluid with a bulk density of  $\eta = 0.367$  which we model using DFT. The corresponding depletion potential is shown in Fig. 5.8.

As the two setups are not completely identical, the results agree only qualitatively. Furthermore, hypernetted-chain integral equations neglect bridge functions which lowers the accuracy of the results of setup (a). Considering the small radius of cavity of the lock and the relatively high packing fraction  $\eta$  of the depletion agent we can for our approach not exclude that caustic effects affect the results obtained

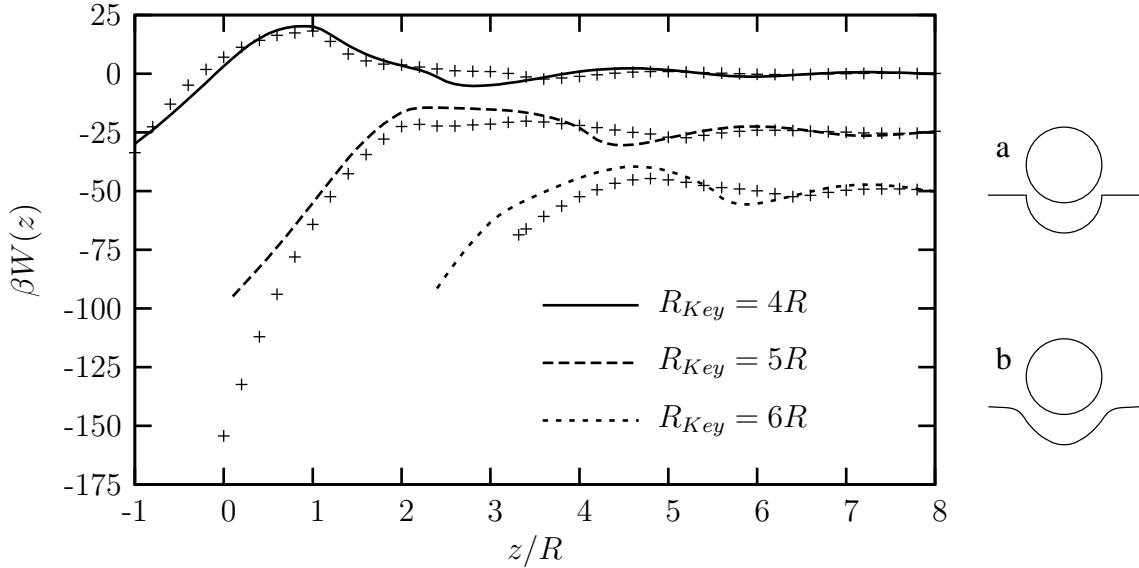


Figure 5.8: Depletion potential between a hemispherical cavity of radius  $5R$  (“lock”) and a spherical key with variable radius  $R_{key}$ . We compare two slightly different geometric setups. On the one hand the symbols are obtained for setup (a) by solving the hypernetted-chain equation on a 3D grid [98]. On the other hand we obtain the data shown as lines for setup (b) by employing the curvature expansion technique. There are, as expected, quantitative differences between the two approaches/geometries. However both results agree insofar as the contact value of the depletion potential is most negative for  $R_{key} = 5R$ , i.e. for the case when the key fits best into the lock. For our data shown as lines the contact values of the depletion potential are  $\beta W^c \approx -30, -70, -41$  for  $R_{key} = 4R, 5R, 6R$ , respectively. Note also that both approaches predict a high free-energy barrier for the key upon approaching the lock. The bulk packing fraction of the hard-sphere fluid is  $\eta = 0.367$  in both setups.

for setup (b). Nonetheless, important qualitative features can be observed in either model. The contact value of the depletion potential, which is the stabilization free energy for touching, is always negative. The touching of key and lock is therefore entropically favored compared to any other configuration and effective interactions therefore indeed contribute to the efficiency of the key-lock-system. In addition to this observation, the key with the most “compatible” shape with respect to the lock has the highest stabilization free energy and it is therefore most likely that this compatible key binds to the cavity of the lock. This observation suggests an interesting mechanism concerning the selectivity of enzymes.

We investigate this observation further and consider another system which consists of a nonspherical key particle and a compatible lock. This system is drawn to scale in Fig. 5.7. The half-axes of the biaxial “key”-ellipsoid are  $(10, 10, 4)R$  and the lock is a plane with a cavity with the shape of an identical ellipsoid. In this setup we vary the penetration parameter  $A$  between  $A = 0$  (planar wall) and  $A = 1$  (full half-elliptical cavity with rounded edge). Figure 5.9 shows the results for the contact value of the depletion potential using our approach and compares the results with data obtained by employing the Asakura-Oosawa approximation (AOa) [7].

Both models agree insofar that the stabilization free energy is most negative if  $A$  is the largest, i.e. if the key and the lock particle have the most compatible shape. This can be understood to some extent geometrically within the AOa which states that the depletion interaction is proportional to the overlap of the excluded volumes around the key and the lock. The overlap volume increases if both particles touch on a larger part of their surface. Aside from this qualitative trend we however observe that the predictions of the AOa fail quantitatively if the depleted excluded volume becomes large. This is unexpected because it was reported commonly in the past that the contact value of the depletion potential between the AOa and more elaborate theories agrees surprisingly well. For  $A = 0$ , there is indeed a relatively good agreement (see Fig. 5.9), otherwise however the AOa underestimates the absolute contact value of the depletion potential by far. This effect was recently also reported by Kinoshita in Ref. [97].

As far as the behavior of the contact value of the depletion potential is concerned, effective interactions offer a very interesting mechanism to explain the efficiency and the selectivity of an enzyme. One important issue however, which we did not consider so far, is the free-energy barrier which the key-particle experiences when approaching the lock. It can be seen in all potentials shown in Fig. 5.8 and is due to correlation effects of the depletion agent in the system. Note that the AOa neglects

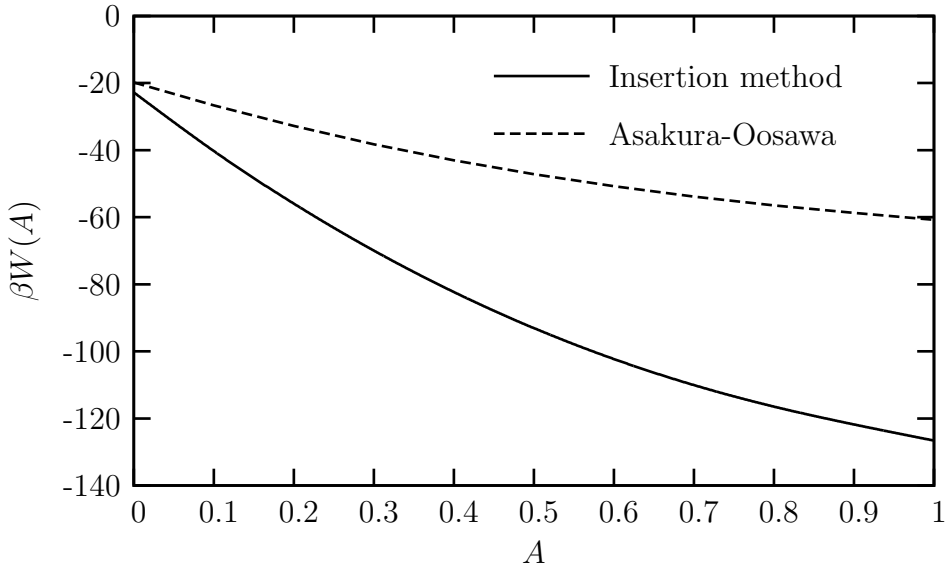


Figure 5.9: Contact value of the depletion interaction between a key and a lock particle as sketched in Fig. 5.7. The full line gives the results using the insertion method and the curvature expansion. It can be seen that the value of the depletion potential becomes more negative for an increased penetration parameter  $A$  of the lock. This means that the contact value decreases if the shapes of the key and the lock become more compatible. This is qualitatively also expected from the results of the Asakura-Oosawa approximation [7], shown as a dashed line. It is, in accordance with earlier works, surprisingly reliable for  $A = 0$ . It however fails to predict the contact value for geometries with a heavily depleted excluded volume. In this figure, the depletion agent is a hard-sphere fluid modeled via the White-Bear functional and a bulk packing fraction of  $\eta = 0.3$ .

these correlations completely. This is a poor approximation for the dense colloidal suspension. Taking the non-ideal character of the cytoplasm into account leads, according to the theory of asymptotic decay of correlation functions presented in Section 4.3, to an oscillatory structure of the depletion potential. Consequently a negative contact value inevitably leads to a positive value of the depletion potential for another normal distance. Note that, although the height of the barrier is smaller than the contact value, it exceeds the thermal energy by far and therefore prevents key and lock particle from coming together.

One possibility to solve this problem would be to bypass the barrier by choosing an alternative path for the key towards the lock. So far, only results for paths along the symmetry axes have been shown, but we also tested that the key experiences

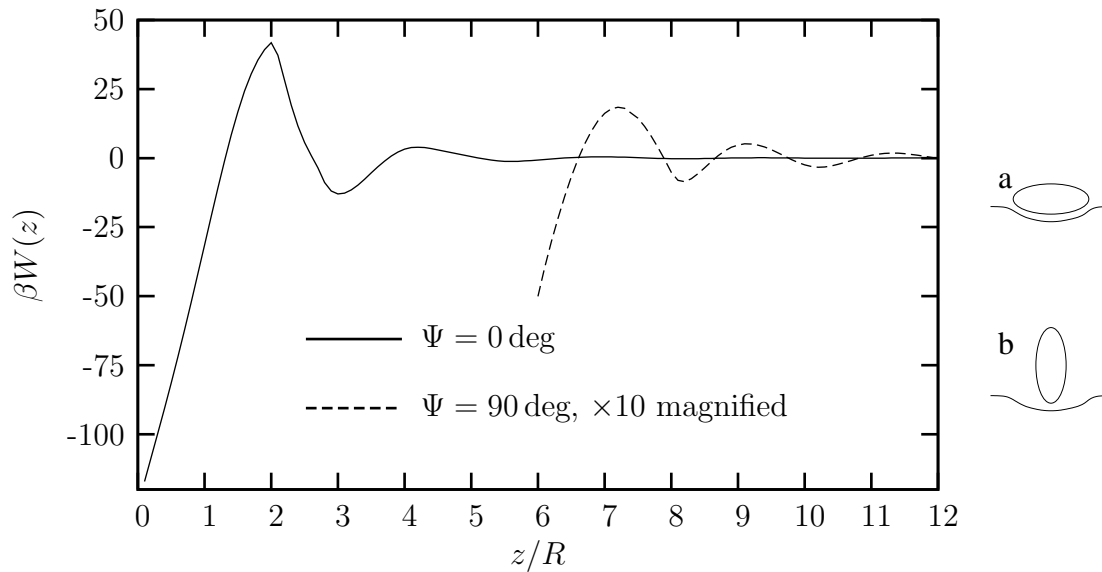


Figure 5.10: Depletion interaction between a biaxial ellipsoid with half axes  $(10, 10, 4)R$  and a lock particle with a compatible shape as sketched in Fig. 5.7. The penetration parameter is  $A = 1$ . The solid line shows the effective interaction when the ellipsoid is not turned, which corresponds to a situation as shown as (a) on the right hand side. It touches the lock not until  $z = 0$ . The dashed line shows the result when the key is rotated around the  $x$ -Axis by  $\Psi = 90$  deg [configuration (b)]. In this case touching occurs already for  $z = 6R$ . Note that the depletion potential is enlarged by a factor of 10 as it is small compared to the first case. The depletion agent is a hard-sphere fluids with  $\eta = 0.3$ .

a high barrier also for various other trajectories. In some cases the height is lower, but there is no path with a monotonic run of the depletion potential which would be needed to use effective interactions as an explanation for the efficiency of key-lock systems. Fortunately this problem can be resolved by introducing further degrees of freedom. We do this by considering a sufficiently *nonspherical* particle as a key. This situation is qualitatively different insofar as the degeneracy of the depletion potential with respect to the angular degrees of freedom of the key is removed. The orientation of the key then has a large influence on the depletion potential, as we show for a biaxial ellipsoid and a compatible key in Fig. 5.10.

The amplitude of the depletion potential strongly depends on the orientation of the key particle. This finding suggests to use an orientation for the approach such that the entropic barrier is minimal. This extreme case corresponds to a key rotated by 90 deg and sketched as configuration (b) in Fig. 5.10. In this case the overlap of

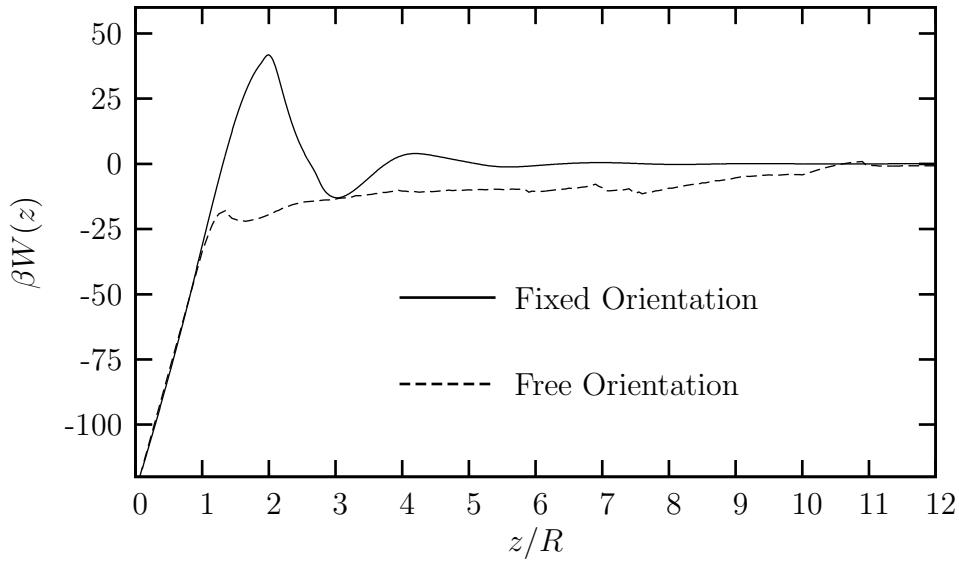


Figure 5.11: Depletion potential between an elliptical key and a lock particle as sketched in Fig. 5.7. For a setup where the key approaches the lock on the symmetry axes with a fixed orientation, the corresponding depletion potential is shown as a solid line. The particle has a very high contact value but also a high entropic barrier which is very unlikely to be overcome. If however the key approaches with a free orientation and is additionally allowed to move away from the symmetry axis, the barrier is practically fully attenuated and the system can follow the local gradients of the effective force and torques towards touching. Close to touching, the key follows a very similar trajectory in both cases (see Fig. 5.12). The depletion agent is a hard-sphere fluid with  $\eta = 0.3$ .

the excluded volumes is the lowest and, according to the qualitative prediction of the AOA, the contact value of the depletion potential is the lowest, too. This means that also the free-energy barrier is very much attenuated. This however brings two problems. First the effective interactions as a whole are not very strong and therefore cannot be used to explain the effectivity of key-lock systems. Furthermore a rotated key cannot be fit into the lock, i.e. it must be rotated after it reached the touching position. This rotation is influenced by an entropic torque and also hindered by a free-energy barrier.

No barrier is found when considering an approach of the key towards the lock where one gives up the unphysical constraint that the Euler angles and the position  $x$  of the center of the key are fixed. In a model we chose for each position  $z$  these parameters such that the key is in a local minimum of the depletion potential. We achieve this by a numerical minimization scheme which additionally ensures that the

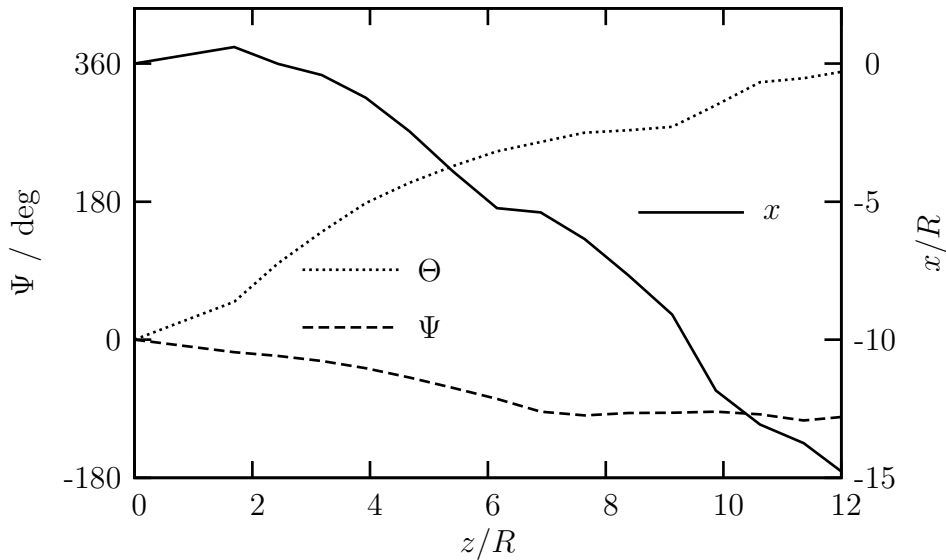


Figure 5.12: Orientation and position of the key when approaching with a free orientation. The depletion potential is shown as a dashed line in Fig. 5.11. For large distance  $z$  the Euler angle  $\Phi \approx -90$  deg, i.e. the key is rotated perpendicular to its orientation at touching. Its center is at a large distance  $x$  to the symmetry axis. The depletion forces and torques in this model ensure that for  $z \approx 0$  both the Euler angles  $\Theta$  and  $\Phi$  as well as the deviation  $x$  from the symmetry axis are close to zero which means that the particle is oriented and positioned optimal for touching. For the illustration of the trajectory see Fig. 5.13.

trajectory of the key through the phase space is continuous. This model is more realistic as it allows the key particle to orient according to the local entropic torque. With this assumptions we obtain a potential as shown by the dashed line in Fig. 5.11.

The resulting depletion potential is almost monotonic, in particular the free-energy barrier is very much attenuated and it is very likely to be overcome by the key particle. The effective interaction provides a force and a torque that “guides” the key to the lock for touching, whereby guiding refers not only to positioning, but also to a correct orientation of the key. This is a very remarkable mechanism. Obviously the additional degrees of freedom of a nonspherical particle do not only allow to bypass the energetic barrier which is always present for spherical particles but are also influenced by the local gradients of the depletion potential in a way that the key is correctly oriented when it comes close to the lock. This can be seen in Fig. 5.12 where the orientation and the position of the key is shown versus the distance from the lock. The corresponding trajectory is illustrated in Fig. 5.13.

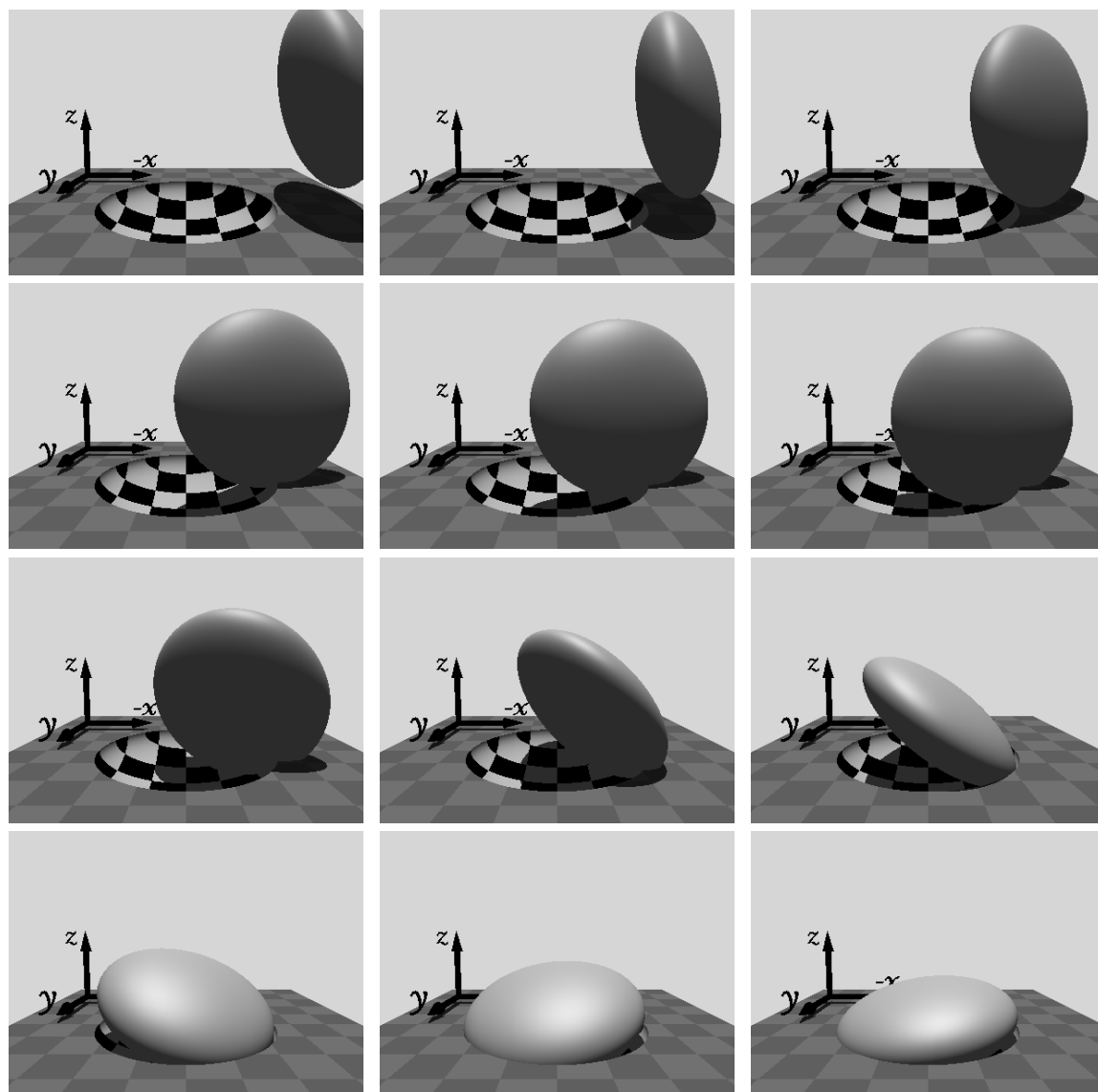


Figure 5.13: Sketches of the key-lock system. The figures illustrate a trajectory of the key particle along which it experiences a practically monotonic depletion potential. The sequence shows, going line-wise from top left to bottom right, the configuration of the system for  $z = 12, 11, \dots, 1$ . The respective positions and Euler angles are shown in Fig. 5.12, the potential is displayed in Fig. 5.11. Note the for practical reasons the lock is shown with an edge, although the calculation was done using the system with a rounded edge presented in Fig. 5.7.



Such a mechanism assumes thermodynamic equilibrium for all separation  $z$  which may be violated and therefore the results presented here should not be seen as effective potentials that quantitatively describes the dynamics of our key and lock system. Additionally we applied several approximations. However the idea that orientational degrees of freedom of sufficiently asymmetric key-objects can be used to bypass free-energy barriers should be qualitatively valid in more general situations.

# Chapter 6

## Summary and Outlook

It is usually very complicated to use direct numerical methods to obtain properties of fluids near complexly shaped walls. For this reason we develop and test a curvature expansion technique and apply it successfully to predict various thermodynamic observables near curved walls. This method treats the influence of the local curvatures  $H$  and  $K$  perturbatively, which allows to predict a quantity at complexly shaped walls based on the knowledge of the quantity for selected simple walls. This method is numerically far less costly than the application of numerical brute-force approaches.

We propose a morphometric form for thermodynamic potentials of fluids which satisfy three physically motivated restrictions [55]. This conjecture implies that thermodynamic excess quantities have only a linear contribution in the mean and the Gaussian curvature and not an infinite series of terms as assumed before. We verified this result for various systems by an extensive numerical study using density-functional theory and Monte-Carlo simulation data. It was however not possible to rigorously prove the morphometric conjecture for a non-trivial fluid. Considering the far-reaching implications of a multiplicative separation of the grand potential in geometric measures and thermodynamic properties it would be very interesting to investigate this issue further. There exist fluids which are known *not* to have a morphometric form of the grand potential [50, 40] and it should be elucidated under which conditions morphometric thermodynamics can be applied and when it breaks down.

The morphometric form of thermodynamic quantities is a very convenient ansatz for theoretical considerations when fluid interfaces have a complex shape so that direct methods cannot be applied. This is e.g. the case in porous media, where a fluid is confined by a complexly shaped solid matrix. Based on the thermodynamic quantities

---

found by geometric means only, transport properties can be derived in such systems. In microemulsions, where the thermodynamic state of a fluid determines the shape of its phase, morphometric thermodynamics provides a basis to understand the corresponding phase-diagram. A further application could be protein folding, which is currently researched using large-scale computer simulations to account for the influence of the surrounding fluid matrix. If the grand potential depends morphometrically on the geometry, the energy cost for a specific configuration of the protein molecule can be estimated based on pure geometric arguments with a largely reduced numerical effort. Calculating phase-diagrams for experimentally accessible types of fluids is usually very hard, as these fluids are usually polydisperse mixtures of various complexly shaped particles. Morphometry offers a practical ansatz within free-volume theory to understand thermodynamic properties of such systems and to derive their phase diagrams.

The next step of this work is concerned with structural properties of fluids, in particular the local density distribution of fluid particles near a wall. Based on the morphometric form of thermodynamic quantities we propose a curvature expansion of the density profile. This method assumes that the density depends only on the *local* geometric measures and can therefore be used to predict the density distribution around complexly shaped objects. For the prediction we use curvature expansion coefficients functions which we obtain from simple geometric setups. Some mathematical properties of the expansion functions can be understood by sum-rules that ensure a morphometric form for derived thermodynamic quantities. In the asymptotic limit we derive a general functional form for density profiles in arbitrary geometries and found numerically for a hard-sphere fluid that they can be predicted using only the density profile at a planar wall. Considering the very general assumptions exercised when deriving this form this finding should apply also to other fluids and would be very interesting to establish some of the numerical findings also analytically.

The curvature expansion of density profiles allows to study distributions of particles on complicated geometries. This is interesting e.g. in microfluidics, where very small amounts of a suspension are processed on a chip. In this regime fluids cannot be considered to have a continuous density distribution because surface effects dominate the system. For practical applications it is necessary to control the density distribution and the influence of curvature could be used for this purpose.

In the final chapter we employ the curvature expansion technique to calculate depletion interactions between two arbitrarily shaped objects. Depletion potentials are always negative for touching and hence offer a chemically non-specific mechanism

for the attractive forces. These are needed to explain the efficiency of enzymatic reactions. We propose a simple model for a biological key-lock system. The depletion interaction favors the touching state of the key particle the most which fits best into the cavity provided by the lock. This is an interesting mechanism concerning the selectivity of enzymes. We find furthermore that only sufficiently asymmetric key particles can reach touching with essentially no free-energy barrier, i.e. the effective interactions do not hinder both particles from coming together. Moreover, depletion forces and entropic torques even “guide” an asymmetric key such that it assumes a correct position and orientation when touching the lock. We present results for one system and it would be interesting to investigate also other systems in order to study the stability of the mechanism concerning the geometry of the involved objects. The selectivity of enzymatic reactions was not studied here within the context of effective forces and torques but it is tempting to assume that it can also be explained by using purely geometric arguments. If the key-particle has a sufficiently incompatible shape, it might experience a potential barrier or alternatively the correct positioning and orienting might not be promoted by depletion interactions any more.

Key-lock systems are a more realistically described by including effective interactions in the models. This is not only important to understand generically biologic processes but is also valuable for drug design for instance. Many drugs also act like a key and trigger a certain biochemical reaction. To create new agents one is interested to find appropriate molecules that on the one hand react efficiently with a given binding site and on the other hand are selective to reduce adverse reactions.

# Appendix A

## Geometric Quantities

A hard physical object - either infinite or finite - can be described mathematically by its surface  $S$  that divides the “inside” of the object from the “outside”. This section is devoted to an overview over all geometrical shape descriptors used in this thesis and does not aim to provide an accurate mathematical introduction into this field. The interested reader is referred to Refs. [99, 52]. This section provides formulas which are useful for actual calculations of geometrical quantities in three dimensions and points out mutual relations between the quantities as needed in this thesis.

A surface can be regarded as a mapping  $S : U \subset \mathbb{R}^2 \rightarrow \mathbb{R}^3$ , i.e. there exists a function  $\mathbf{r}(\alpha, \beta)$  that yields all points of the surface  $S$ . We assume that the function is “well behaved”, in particular it must be differentiable with respect to both arguments. Two tangential vectors are defined via

$$\mathbf{t}_\alpha = \frac{\partial \mathbf{r}(\alpha, \beta)}{\partial \alpha} \quad \text{and} \quad \mathbf{t}_\beta = \frac{\partial \mathbf{r}(\alpha, \beta)}{\partial \beta}. \quad (\text{A.1})$$

For every point  $\mathbf{r}(\alpha, \beta)$  there exists a normal  $\mathbf{n}(\alpha, \beta)$  which is defined via

$$\mathbf{n}(\alpha, \beta) = \frac{\mathbf{t}_\alpha \times \mathbf{t}_\beta}{\|\mathbf{t}_\alpha \times \mathbf{t}_\beta\|}, \quad (\text{A.2})$$

where  $\|\mathbf{r}\| = \sqrt{r_x^2 + r_y^2 + r_z^2}$  denotes the usual Euclidean norm. The orientation of the normal  $\mathbf{n}$  depends on the parameterization of  $\mathbf{r}(\alpha, \beta)$  and by convention we choose that the normal  $\mathbf{n}$  points away from the hard object we describe via its perimeter  $S$ .

The Weingarten-mapping or the shape operator  $W$  is defined using the short hand notation

$$W(\mathbf{t}) = \partial_{\mathbf{t}} \mathbf{n}, \quad (\text{A.3})$$

and describes the variation of the surface normal  $\mathbf{n}$ . For every linear combination  $\mathbf{t}$  of  $\mathbf{t}_\alpha$  and  $\mathbf{t}_\beta$ , i.e. for every vector pointing along the surface,  $W$  maps this vector

on the change of the normal vector along the direction of  $\mathbf{t}$ . One can show that  $W(\mathbf{t}) \cdot \mathbf{n} = 0$ , i.e. the change of the normal is always perpendicular to the normal. As the Weingarten mapping is a linear mapping from and to the tangential space  $\text{span}(\mathbf{t}_\alpha, \mathbf{t}_\beta)$  of the surface  $S$  it can, for the basis  $\{\mathbf{t}_\alpha, \mathbf{t}_\beta\}$ , be expressed by a matrix multiplication with a  $2 \times 2$  - matrix  $W$

$$\begin{pmatrix} W(\mathbf{t}_\alpha) \\ W(\mathbf{t}_\beta) \end{pmatrix} = W \cdot \begin{pmatrix} \mathbf{t}_\alpha \\ \mathbf{t}_\beta \end{pmatrix}. \quad (\text{A.4})$$

For the actual calculation one uses that

$$W(\mathbf{t}_\alpha) = \frac{\partial \mathbf{n}(\alpha, \beta)}{\partial \alpha}, \quad W(\mathbf{t}_\beta) = \frac{\partial \mathbf{n}(\alpha, \beta)}{\partial \beta}, \quad (\text{A.5})$$

and forms the outer vector product between Eq. (A.4) and  $(\mathbf{t}_\alpha, \mathbf{t}_\beta)$  which yields the following matrix equation

$$\begin{pmatrix} \partial_\alpha \mathbf{n} \cdot \mathbf{t}_\alpha & \partial_\alpha \mathbf{n} \cdot \mathbf{t}_\beta \\ \partial_\beta \mathbf{n} \cdot \mathbf{t}_\alpha & \partial_\beta \mathbf{n} \cdot \mathbf{t}_\beta \end{pmatrix} = W \begin{pmatrix} \mathbf{t}_\alpha \cdot \mathbf{t}_\alpha & \mathbf{t}_\alpha \cdot \mathbf{t}_\beta \\ \mathbf{t}_\beta \cdot \mathbf{t}_\alpha & \mathbf{t}_\beta \cdot \mathbf{t}_\beta \end{pmatrix}, \quad (\text{A.6})$$

which can be solved for  $W$ . The scalar products in the elements of the matrices are conventionally abbreviated by upper- and lower-case characters as indicated by the following short-hand notation of Eq. (A.6)

$$\begin{pmatrix} e & f \\ f & g \end{pmatrix} = W \begin{pmatrix} E & F \\ F & G \end{pmatrix} \Rightarrow W = \frac{1}{EG - F^2} \begin{pmatrix} -fF + eG & Ef - eF \\ -Fg + fG & -fF + Eg \end{pmatrix}. \quad (\text{A.7})$$

The eigenvalues of  $W$  are the inverse radii of curvature  $\kappa_1$  and  $\kappa_2$  and one therefore defines

$$H = \frac{1}{2} \text{tr}(W) = \frac{-2fF + Eg + eG}{2(-F^2 + eG)}, \quad K = \det(W) = \frac{f^2 - eg}{F^2 - eG}, \quad (\text{A.8})$$

to be the mean  $H$  and Gaussian  $K$  curvature respectively. Note that  $H = \frac{1}{2}(\kappa_1 + \kappa_2)$  and  $K = \kappa_1 \kappa_2$  as both trace  $\text{tr}(\cdot)$  and determinate  $\det(\cdot)$  are independent of the choice of the basis.  $H$  and  $K$  are sufficient to describe the shape of the surface  $S$ , but contain no information concerning the orientation and position of the surface in space.

The total area  $A$  of the surface can be calculated using

$$A[S] = \int_S d\mathbf{x} = \int_U \|\mathbf{t}_\alpha(\alpha, \beta) \times \mathbf{t}_\beta(\alpha, \beta)\| d\alpha d\beta. \quad (\text{A.9})$$

Similarly one defines

$$C[S] = \int_S H(\alpha, \beta) d\mathbf{x} \quad \text{and} \quad X[S] = \int_S K(\alpha, \beta) d\mathbf{x}, \quad (\text{A.10})$$

to be the integral mean  $C$  and integral Gaussian  $X$  curvature of  $S$ . The latter is also denoted as Euler characteristic and equals  $4\pi$  for every single-connected object independent of its shape.

One defines a parallel surface  $S'$  with a fixed normal distance  $u$  with respect to the original  $S$  using

$$\mathbf{r}'(\alpha, \beta) = \mathbf{r}(\alpha, \beta) + u \mathbf{n}(\alpha, \beta). \quad (\text{A.11})$$

All geometrical quantities presented in this section for the surface  $S$  can equally well be calculated for  $S'$ . One can prove the following useful relations, where primed quantities belong to the parallel surface  $S'$  with distance  $u$

$$H' = \frac{H + Ku}{1 + 2Hu + Ku^2} \quad \text{and} \quad K' = \frac{K}{1 + 2Hu + Ku^2}. \quad (\text{A.12})$$

Note that the solving these equations for  $H$  and  $K$  can be easily done by setting  $u \rightarrow -u$  and interchanging primed and unprimed quantities. An integration over  $S'$  can be performed using the Jacobian  $J(u)$

$$d\mathbf{x}' = J(u) d\mathbf{x}, \quad J(u) = 1 + 2Hu + Ku^2, \quad (\text{A.13})$$

which allows one to derive the following relations

$$\begin{aligned} V' &= V + Au + Cu^2 + \frac{1}{3}Xu^3, \\ A' &= A + 2Cu + Xu^2, \\ C' &= C + Xu, \\ X' &= X. \end{aligned} \quad (\text{A.14})$$

These relations are remarkable insofar as the knowledge of  $V$ ,  $A$ ,  $C$ , and  $X$  on one surface is sufficient to calculate the respective quantities for any parallel distance. This is a direct consequence of the Hadwiger theorem, which states that every motion-invariant, continuous and additive functional of  $S$  must be a linear combination of  $V[S]$ ,  $A[S]$ ,  $C[S]$ , and  $X[S]$ . The three conditions are also fulfilled for the primed quantities  $V'$ ,  $A'$ ,  $C'$ , and  $X'$  which can according to Eq. (A.14) indeed be written in the predicted form.

If a quantity  $Q$  is a functional of  $S$ , i.e. if  $Q$  is a mapping  $S \rightarrow \mathbb{R}$ , we introduce the “normal derivative”  $\partial_u Q[S]$  of  $Q$  which we define via

$$\partial_u Q[S] = \lim_{u \rightarrow 0} \frac{Q[S'] - Q[S]}{u}, \quad (\text{A.15})$$

where  $S'$  is a parallel surface to  $S$  with normal distance  $u$ . Using Eq. (A.12) and Eq. (A.14) one can evaluate the following normal derivatives using the definition in Eq. (A.15)

$$\begin{aligned} \partial_u V &= A, & \partial_u A &= 2C, & \partial_u C &= X, & \partial_u X &= 0 \\ \partial_u H &= K - 2H^2, & \partial_u K &= -2HK, & \partial_u \bar{H} &= \bar{K} - 2\bar{H}^2, & \partial_u \bar{K} &= -2\bar{H}\bar{K}, \end{aligned} \quad (\text{A.16})$$

where  $\bar{H} = C/A$  and  $\bar{K} = X/A$ . Note that  $\bar{H}^2 = (\bar{H})^2 \neq \bar{H}^2$ .

For a given triple of parameters  $(\alpha, \beta, u)$  one can define the following point  $\mathbf{r}'$  in space

$$\mathbf{r}'(\alpha, \beta, u) = \mathbf{r}(\alpha, \beta) + u \mathbf{n}(\alpha, \beta), \quad (\text{A.17})$$

and refer to  $(\alpha, \beta, u)$  as the normal coordinates of  $\mathbf{r}'$ . The transformation from the normal to Cartesian coordinates is trivially achieved by Eq. (A.17) and can be applied for any  $(\alpha, \beta, u)$ , the inverse transformation from a point  $\mathbf{r}'$  given in Cartesian coordinates to normal coordinates  $(\alpha, \beta, u)$  however is not necessarily unique. This is because some points outside a surface may be reached from multiple points  $\mathbf{r}(\alpha, \beta)$  on  $S$ . One can ensure a global (for all points *outside*  $S$ ) bijective mapping between Cartesian and normal coordinates by demanding that  $S$  is convex [ $\kappa_1, \kappa_2 > 0$  for all  $(\alpha, \beta)$ ]. Otherwise bijectivity can only be fulfilled piecewise.

Finally, some surfaces are discussed explicitly as they are commonly used in this thesis. In all cases,  $(x, y, z)$  denote Cartesian coordinates of a point while the two lateral coordinates  $\alpha$  and  $\beta$  are commonly renamed for reasons of clarity. Note that the locus where the external potential exerted on the fluid particles is discontinuous, represents a parallel surface to the actual physical wall. The parallel distance of the surfaces is  $R$ , where  $R$  is the radius of the fluid particles.

- **Planar wall:** The physical wall is located at

$$\mathbf{r} = (x, y, -R), \quad (\text{A.18})$$

where  $x, y \in \mathbb{R}$ . The external potential is discontinuous at  $z = 0$  and the curvatures  $H = 0 = K$  vanish for all  $x$  and  $y$ .

- **Cylindrical wall:** The physical wall is located at

$$\mathbf{r} = (R_C \sin(\phi), R_C \cos(\phi), z), \quad (\text{A.19})$$

where  $\phi \in (-\pi, \pi)$  and  $z \in \mathbb{R}$ . The external potential is discontinuous at a cylindrical wall with  $R'_C = R_C + R$ , which has the dimensionless curvatures  $H = R/(2(R_C + R))$  and  $K = 0$ .



- **Spherical wall:** The physical wall is located at

$$\mathbf{r} = R_S(\sin(\theta) \cos(\phi), \sin(\theta) \sin(\phi), \cos(\theta)), \quad (\text{A.20})$$

where  $\theta \in (0, \pi)$  and  $\phi \in (0, 2\pi)$ . The external potential is discontinuous at a spherical wall with  $R'_S = R_S + R$ , which has the dimensionless curvatures  $H = R/(R_S + R)$  and  $K = (R/(R + R_S))^2$ .

- **Ellipsoidal wall:** The physical wall is located at

$$\mathbf{r} = (a \sin(\theta) \cos(\phi), b \sin(\theta) \sin(\phi), c \cos(\theta)), \quad (\text{A.21})$$

where  $\theta \in (0, \pi)$  and  $\phi \in (0, 2\pi)$ . Note that the effective wall where the potential is discontinuous is *not* an ellipsoid. For a general triaxial ellipsoid, the dimensionless curvatures  $H$  and  $K$  are lengthy expressions which simplify for a biaxial ellipsoid with  $b = a$  to

$$H = \frac{Rc}{\sqrt{2}a} \frac{2a^2 + M^2}{M^3}, \quad K = \frac{4c^2 R^2}{M^4}, \quad (\text{A.22})$$

where  $M = \sqrt{(a^2 + c^2) + (a^2 - c^2) \cos(2\theta)}$ . If  $c > a = b$  the object is called “prolate”, for  $c < a = b$  “oblate”.

- **Shrunk ellipsoid:** For simulations it is inconvenient to consider an ellipsoid as a *physical* wall. Normally it is easier to implement an effective wall with the shape of an ellipsoid. In this case the corresponding physical wall is a parallel surface with distance  $u = -R$  to an ellipsoid. We refer to it as a “shrunk ellipsoid” as it is not an generic ellipsoid. The surface can be parameterized

$$\mathbf{r}'(\theta, \phi) = \mathbf{r}(\theta, \phi) - R\mathbf{n}(\theta, \phi) \quad (\text{A.23})$$

where  $\mathbf{r}(\theta, \phi)$  is a point on the surface of the underlying ellipsoid with half axes  $(a, b, c)$  and  $\mathbf{n}(\theta, \phi)$  is the surface normal.

# Appendix B

## Obtaining Curvature Expansion Coefficients

The properties of a fluid in contact with curved walls are normally very complicated to be obtained by means of direct methods. Every quantity  $Q$  associated with the interface can be considered as a functional of the wall, where the actual form of the functional mapping depends on the intrinsic parameters of the fluid. One intuitive approximation of the functional mapping is the curvature expansion of  $Q$  which assumes that the numerical value of  $Q$  does only depend on the *local* curvatures  $H$  and  $K$  of the wall. This approximation neglects the possible influence of lateral variations of the curvatures along the wall and furthermore assumes an analytic dependence on both  $H$  and  $K$

$$Q = Q_P + HQ_H + KQ_K + H^2Q_{H^2} + HKQ_{HK} + H^3Q_{H^3} + \mathcal{O}(R_{1,2}^{-4}). \quad (\text{B.1})$$

Here,  $Q_P$  denotes the value of  $Q$  at a planar and infinitely extended interface.  $Q_\xi$  for  $\xi = H, K, H^2, HK, H^3, \dots$  are curvature expansion coefficients. Equation (B.1) shifts the problem of determining  $Q$  in complex geometries to the problem of determining the coefficient functions  $Q_\xi$ . To this end, we propose the following scheme. Assuming that Eq. (B.1) is valid for arbitrary geometries we apply it also for selected simple geometric setups. One particularly simple wall geometry is a planar wall, which can usually be most easily implemented in numerical calculations. We denote the result for the quantity  $Q$  at a planar wall by  $Q_P$ . In order to find higher order curvature expansion coefficients  $Q_\xi$ , we consider two other geometric setups that can usually also be treated numerically. These are an infinitely long cylindrical wall with radius  $R_C$  and a spherical wall with radius  $R_S$ . In the context of a fluid of hard spheres

with radius  $R$ , the effective walls have dimensionless curvatures  $H = R/(2(R + R_C))$  and  $K = 0$  for the cylinder and  $H = R/(R + R_S)$  and  $K = (R/(R + R_S))^2$  for the sphere. Inserting the dimensionless curvatures for the cylinder in Eq. (B.1) yields

$$\begin{aligned} Q &= Q_P + \left(\frac{R}{2(R+R_C)}\right) Q_H + \left(\frac{R}{2(R+R_C)}\right)^2 Q_{H^2} + \left(\frac{R}{2(R+R_C)}\right)^3 Q_{H^3} + \dots, \\ &= Q_P + \sum_{\alpha=0}^{\infty} \left(\frac{R}{2(R+R_C)}\right)^{\alpha} Q_{H^{\alpha}}. \end{aligned} \quad (\text{B.2})$$

Note that all coefficients which contain  $K$  drop out of the expansion as  $K = 0$  for the cylinder. Therefore the dependence on the radius  $R_C$  of the cylinder is a polynomial in  $R/(2(R + R_C)) = H$ . Based on numerical data we fit the expansion coefficients  $Q_P$  and  $Q_{H^{\alpha}}$  for  $\alpha = 1, 2, \dots$ . Note that the fit should, as a test for the internal consistency of the numerical data, yield the same  $Q_P$  as obtained for the planar wall. We confirmed this in the context of various quantities  $Q$  with very high accuracy.

To obtain further coefficient functions we calculate  $Q$  for a spherical wall. According to Eq. (B.1), we expect the following behavior:

$$\begin{aligned} Q &= Q_P + \left(\frac{R}{R+R_S}\right) Q_H + \left(\frac{R}{R+R_S}\right)^2 (Q_{H^2} + Q_K) + \left(\frac{R}{R+R_S}\right)^3 (Q_{H^3} + Q_{HK}) + \dots, \\ &= Q_P + \sum_{\alpha=0}^{\infty} \left(\frac{R}{R+R_S}\right)^{\alpha} Q^{(\alpha)}. \end{aligned} \quad (\text{B.3})$$

Similarly to the cylinder, the shape dependence on the radius  $R_S$  of the sphere reduces to a polynomial in  $R/(R + R_S)$ . We abbreviate the respective coefficients by  $Q^{(\alpha)}$  and obtain them also from a fit of numerical data. We again verified for various  $Q$  that  $Q_P$  obtained from this fit is the same as the  $Q$  obtained at a planar wall. The internal consistency of the curvature expansion approach, Eq. (B.1), can be tested by comparing  $Q_H$  and  $Q^{(1)}$ , which must be equal. We found this relation fulfilled very accurately for all quantities  $Q$  analyzed.

For the radius expansion for a spherical wall, Eq. (B.3), all curvature expansion coefficients  $Q_{\xi}$  used in the full curvature expansion contribute to  $Q$ . As some of the coefficients feature the same order in  $R/(R + R_S)$ , they cannot be distinguished based on the data for a spherical wall alone. However, in combination with the results of the cylinder, which yields all  $Q_{H^{\alpha}}$ , we identify together with the  $Q^{(\alpha)}$  obtained from the spherical wall

$$Q_K = Q^{(2)} - Q_{H^2}, \quad Q_{HK} = Q^{(3)} - Q_{H^3}. \quad (\text{B.4})$$

This idea can unfortunately not be extended beyond the third order terms, as the fourth order coefficient  $Q^{(4)}$  for a sphere is already a sum of the three curvature

expansion coefficients  $Q_{H^4}$ ,  $Q_{H^2K}$ , and  $Q_{K^2}$ . Additional data would be needed to distinguish between  $Q_{H^2K}$  and  $Q_{K^2}$ . As such data must be obtained from calculations of  $Q$  at a complexly shaped wall (neither spherical nor cylindrical), it is normally not available with sufficient accuracy to be used for a curvature expansion. For this practical reason, we truncate the curvature expansion after the third order terms, as indicated in Eq. (B.1). Note that by considering only walls with globally constant curvatures also no contributions due to lateral variations in the curvature can be obtained.

In the case of a cylindrical and spherical wall, we fit numerical data versus an inverse radius,  $R_C$  or  $R_S$  respectively. For the practical implementation of the fit the question arises how many powers of the inverse radius should be included in the fit and what numerical data should be actually used for the fit. In this thesis we use the following two methods.

- If one is interested to find the curvature expansion coefficients such that the results obtained from Eq. (B.1) are very good predictions for the actual calculations, one may choose a set of relatively small radii  $R_C$  and  $R_S$  and do a fit as sketched in Eq. (B.2) and in Eq. (B.3). As only three power can be analyzed, not higher powers should be included for the fit. In doing such an analysis, not enough fitting orders are available to capture the full influence of the curved wall, however one can be sure that, by constructions, predictions based on Eq. (B.1) have the least square error compared to the actual numerical results. The disadvantage of such a procedure is that the fitting parameters depend on the set of data chosen and can therefore usually not be compared to analytical results.
- The other extreme case for an analysis is applied if one is not interested in an optimal fit of the data but in the correct values of the expansion coefficients. For this purpose, more than three powers in the curvature must be included in the fit to fully describe the influence of the curved wall. However it is numerically not reliable to include too many fitting coefficients. For the data in this thesis we use a fit up to the fourth order in the curvature. In order to allow a clear distinction between the different orders in the fit, numerical data of large radii  $R_C$  and  $R_S$  is used for the fit ( $100R$  and beyond). We refer to this procedure as “leading order curvature expansion”. As this method leads to poorly conditioned numerical problems it requires data with very low noise, which is usually only available for DFT results.

Coefficients found by the first procedure are used to predict quantities around complex and highly curved objects while otherwise the leading order curvature expansion coefficients are preferred. Note that in case of  $Q$  being a thermodynamic quantity, which is characterized by a truncated expansion Eq. (B.1), both procedures yield the same coefficients  $Q_\xi$ .

# Bibliography

- [1] R. J. Ellis, Trends Biochem. Sci. **26**, 597 (2001). [2](#), [70](#)
- [2] M. Kinoshita, T. Oguni, Chem. Phys. Lett. **351**, 79 (2002). [2](#), [70](#), [71](#)
- [3] M. Kinoshita, Chem. Phys. Lett. **387**, 47 (2004). [2](#), [70](#), [71](#)
- [4] S. B. Zimmerman and A. P. Minton, Annu. Rev. Biophys. Biomol. Struct. **22**, 27 (1993). [2](#)
- [5] A. P. Minton, Curr. Opin. Biotechnol. **8**, 65 (1997). [2](#)
- [6] A. D. Dinsmore, D. T. Wong, P. Nelson, and A. G. Yodh, Phys. Rev. Lett. **80**, 409 (1998). [2](#)
- [7] S. Asakura and F. Oosawa, J. Chem. Phys. **22**, 1255 (1954). [2](#), [13](#), [70](#), [85](#), [86](#)
- [8] P. Hohenberg and W. Kohn, Phys. Rev. **136**, B864 (1964). [5](#)
- [9] N. D. Mermin, Phys. Rev. **137**, A1441 (1965). [5](#)
- [10] R. Evans, Adv. Phys. **28**, 143 (1979). [5](#)
- [11] R. Evans *Les Houches, Session XLVIII, 1988 - Liquides aux interfaces/Liquids at interfaces*, edited by J. Charvolin, J. F. Joanny and J.Zinn-Justin (NorthHolland, Amsterdam, 1990). [5](#)
- [12] R. Evans, *Fundamentals of Inhomogeneous Fluids*, edited by D. Henderson (Dekker, New York, 1992). [5](#), [10](#)
- [13] J.-P. Hansen and I. R. McDonald, *Theory of Simple Liquids* (Academic Press, 2000). [7](#), [8](#), [63](#)
- [14] Y. Rosenfeld, J. Chem. Phys. **89**, 4272 (1988). [7](#), [9](#)

- 
- [15] Y. Rosenfeld, Phys. Rev. Lett. **63**, 980 (1989). [3](#), [7](#), [8](#), [9](#)
- [16] Y. Rosenfeld, J. Chem. Phys. **92**, 6818 (1990). [8](#)
- [17] Y. Rosenfeld, J. Chem. Phys. **93**, 4305 (1990). [8](#)
- [18] J. Percus and G. Yevick, Phys. Rev. **110**, 1 (1958). [8](#)
- [19] E. Kierlik and M. L. Rosinberg, Phys. Rev. A **42**, 3382 (1990). [8](#)
- [20] H. Reiss, H. Frisch, and J. Lebowitz, J. Chem. Phys. **31**, 369 (1959). [9](#), [24](#)
- [21] J. L. Lebowitz and J. S. Rowlinson, J. Chem. Phys. **41**, 133 (1964). [9](#)
- [22] H. Reiss, *Statistical Mechanics and Statistical Methods in Theory and Application*, edited by V. Landman (plenum, New York, 1976). [9](#)
- [23] J. K. Percus and G. J. Yevick, Phys. Rev. **110**, 1 (1957). [10](#)
- [24] R. Piazza, T. Bellini, and V. Degiorgio, Phys. Rev. Lett. **71**, 4267 (1993). [10](#)
- [25] J. C. Crocker and D. G. Grier, Phys. Rev. Lett. **73**, 352 (1994). [10](#)
- [26] J. C. Crocker and D. G. Grier, Phys. Rev. Lett. **77**, 1897 (1996). [10](#)
- [27] V. Degiorgio, R. Piazza, M. Corti, and J. Stavans, J. Chem. Soc. Faraday Trans. **87**, 431 (1991). [10](#)
- [28] J. E. Kirkwood, *Phase Transformations in Solids*, edited by R. Smoluchowski, J. E. Mayer and W. A. Weyl (Wiley, New York, 1951). [10](#)
- [29] W. W. Wood and J. D. Jacobson, J. Chem. Phys. **27**, 1207 (1957). [10](#)
- [30] B. J. Alder and T. E. Wainwright, J. Chem. Phys. **27**, 1208 (1957). [10](#)
- [31] P. Tarazona and Y. Rosenfeld, Phys. Rev. E **55**, R4873 (1997). [10](#)
- [32] Y. Rosenfeld, M. Schmidt, H. Löwen, and P. Tarazona, Phys. Rev. E **55**, 4245 (1996). [10](#)
- [33] Y. Rosenfeld, M. Schmidt, H. Löwen, and P. Tarazona, J. Phys.: Condens. Matter **8**, L577 (1996). [10](#)
- [34] M. Schmidt, Ph.D. thesis, Heinrich Heine Universität Düsseldorf (1997). [10](#)

- [35] G. A. Mansoori, N. F. Carnahan, K. E. Starling, and T. W. Leland, Jr., *J. Chem. Phys.* **54**, 1523-1525 (1971). [10](#)
- [36] N. F. Carnahan and K. E. Starling, *J. Chem. Phys.* **51**, 635 (1969). [10](#)
- [37] R. Roth, R. Evans, A. Lang, and G. Kahl, *J. Phys.: Condens. Matter* **14**, 12063 (2002). [10](#)
- [38] Y.-X. Yu and J. Wu, *J. Chem. Phys.* **117**, 10156 (2002). [10](#)
- [39] Y. Rosenfeld, *Phys. Rev. E* **50**, R3318 (1994). [11](#)
- [40] R. Evans, R. Roth, and P. Bryk, *Europhys. Lett.* **62**, 815 (2003). [12](#), [49](#), [51](#), [92](#)
- [41] S. Asakura and F. Oosawa, *J. Pol. Sci.* **33**, 183 (1958). [13](#)
- [42] A. Vrij, *Pure Appl. Chem.* **48**, 471 (1976). [13](#)
- [43] B. V. Derjaguin, *Kolloid-Z.* **69**, 155 (1934). [14](#)
- [44] P. Attard, *J. Chem. Phys.* **91**, 3083 (1989). [14](#), [70](#)
- [45] P. Attard and G. N. Patey, *J. Chem. Phys.* **92**, 4970 (1990). [14](#)
- [46] P. Attard and J. L. Parker, *J. Phys. Chem.* **96**, 5086 (1992). [14](#)
- [47] R. Roth, R. Evans, and S. Dietrich, *Phys. Rev. E* **62**, 5360 (2000). [14](#), [70](#), [71](#)
- [48] T. Biben, P. Bladon, and D. Frenkel, *J. Phys.: Condens. Matter* **8**, 10799 (1996). [14](#), [70](#)
- [49] J. R. Henderson, *Mol. Phys.* **50**, 741 (1983). [21](#)
- [50] P. Bryk, R. Roth, K. R. Mecke, and S. Dietrich, *Phys. Rev. E* **68**, 031602 (2003). [21](#), [27](#), [51](#), [92](#)
- [51] H. Reiss, H. L. Frisch, E. Helfand, and J. L. Lebowitz, *J. Chem. Phys.* **32**, 119 (1960). [24](#), [27](#), [35](#)
- [52] H. Hadwiger, *Vorlesungen über Inhalt, Oberfläche und Isoperimetrie*, (Springer, Berlin, Germany, 1957). [25](#), [26](#), [95](#)
- [53] R. Evans, J. R. Henderson, and R. Roth, *J. Chem. Phys.* **121**, 12074 (2004). [6](#), [25](#), [49](#), [50](#), [55](#), [60](#), [61](#)



- 
- [54] K. R. Mecke, Int. J. of Mod. Phys. B **12**, 861 (1998). [26](#)
- [55] P.-M. König, R. Roth, and K. R. Mecke, Phys. Rev. Lett. **93**, 160601 (2004). [26](#), [92](#)
- [56] W. Helfrich, Z. Naturforsch. **28C**, 693 (1973). [26](#), [51](#)
- [57] F. H. Stillinger and M. A. Cotter, J. Chem. Phys. **55**, 3449 (1971). [27](#), [61](#)
- [58] P. Bryk, Private Communication (2004). [39](#), [58](#)
- [59] R. Roth, Private Communication (2004). [43](#)
- [60] P. Tarazona, Mol. Phys. **52**, 81 (1984). [45](#), [51](#)
- [61] J. M. Brader, R. Evans, and M. Schmidt, Mol. Phys. **101**, 3349 (2003). [51](#)
- [62] K. R. Mecke, *Integralgeometrie in der Statistischen Physik*, (Verlag Harri Deutsch, Frankfurt, Germany, 1994). [51](#)
- [63] K. R. Mecke, Lecture Notes in Physics, **554**, 111 (2000). [52](#)
- [64] K. Mecke, J. Phys.: Condensed Matter **8**, 9663 (1996). [52](#)
- [65] K. Mecke, Fluid Phase Equilibria **150/151**, 591 (1998). [52](#)
- [66] C. H. Arns, M. A. Knackstedt, and K. R. Mecke, Phys. Rev. Lett. **91**, 215506 (2003). [52](#)
- [67] R. J. Ellis, Trends Biochem. Sci. **26**, 597 (2001). [52](#)
- [68] C. N. Likos, K. R. Mecke, and H. Wagner, J. Chem. Phys. **102**, 9350 (1995). [52](#)
- [69] R. K. P. Zia, Nucl. Phys., **B251**, 676 (1985). [54](#)
- [70] K. R. Mecke and S. Dietrich, Phys. Rev. E **59**, 6766 (1999). [54](#)
- [71] D. M. Tully-Smith and H. Reiss, J. Chem. Phys. **53**, 4015 (1970). [61](#)
- [72] R. J. Baxter, J. Chem. Phys. **52**, 4559 (1970). [63](#)
- [73] R. Evans R., R. J. F. Leote de Carvalho, J. R. Henderson, and D. C. Hoyle, J. Chem. Phys. **100**, 591 (1994). [63](#)
- [74] R. J. F. Leote de Carvalho and R. Evans, Mol. Phys. **83**, 619 (1994). [63](#), [65](#)

- [75] R. Evans and R. J. F. Leote de Carvalho, *Chemical Applications of Density Functional Theory*, edited by B. B. Laird, R. B. Ross, and T. Ziegler (1996). 63
- [76] W. E. Brown, R. J. F. Leote de Carvalho, and R. Evans, *Mol. Phys.* **88**, 579 (1996). 63
- [77] R. J. F. Leote de Carvalho, R. Evans, and Y. Rosenfeld, *Phys. Rev. E* **59**, 1435 (1999). 63
- [78] R. Evans, Private Communication (2004). 64, 66
- [79] C. Grodon, Diploma thesis, Universität Stuttgart (2003). 64
- [80] C. Grodon, M. Dijkstra, R. Evans, and R. Roth, *J. Chem. Phys.* **121**, 7869 (2004). 64, 65
- [81] R. Evans, J. R. Henderson, D. C. Hoyle, A. O. Parry, and Z. A. Sabeur, *Mol. Phys.* **80**, 755 (1993). 65
- [82] M. Dijkstra M., R. van Roij R., and R. Evans, *Phys. Rev. E* **59**, 5744 (1999). 65, 70
- [83] W. G. McMillan and J. E. Mayer, *J. Chem. Phys.* **13**, 276 (1945). 70
- [84] R. Roth, R. Evans, and A. A. Louis, *Phys. Rev. E* **64**, 051202 (2001). 70
- [85] R. Roth, J. M. Brader, and M. Schmidt, *Europhys. Lett.*, **63**, 549 (2003). 70
- [86] J. Martin and F.-U. Hartl, *Proc. Natl. Acad. Sci. USA* **94**, 1107 (1997). 70
- [87] A. P. Minton, *Curr. Opinion in Biotech.* **8**, 65 (1997). 70
- [88] M. M. Garner and M. B. Burg, *Am. J. Physiol.* **266** C877 (1994). 70
- [89] S. B. Zimmerman and A. P. Minton, *Annu. Rev. Biophys. Biomol. Struct.* **22**, 27 (1993). 70
- [90] H.-O. Johansson, D. E. Brooks, and C. A. Haynes, *Intl. Rev. of Cytology* **192**, 155 (2000). 70
- [91] B. Götzelmann, R. Evans, S. Dietrich, *Phys. Rev. E* **57**, 6785 (1998). 70
- [92] B. Götzelmann, R. Roth, S. Dietrich, M. Dijkstra, R. Evans, *Europhys. Lett.* **47**, 398 (1999). 70

- 
- [93] R. Dickmann, P. Attard, V. Simonian, J. Chem. Phys. **107**, 205 (1997). [70](#)
- [94] R. Roth, B. Götzelmann, and S. Dietrich, Phys. Rev. Lett. **83**, 448 (1999). [70](#)
- [95] P. Bryk, R. Roth, M. Schoen, S. Dietrich, Europhys. Lett. **63**, 233 (2003). [70](#)
- [96] R. Roth, R. van Roij, D. Andrienko, K. R. Mecke, and S. Dietrich, Phys. Rev. Lett. **89**, 088301 (2002). [70](#), [79](#), [81](#)
- [97] M. Kinoshita, J. Chem. Phys. **116**, 3493 (2002). [10](#), [71](#), [83](#), [85](#)
- [98] M. Kinoshita, Private Communication (2004). [84](#)
- [99] A. Gray, *Modern differential geometry of curves and surfaces with mathematica* (CRC Press, Boca Raton, USA, 1998). [95](#)

# List of Publications

- P.-M. König, R. Roth, and K. R. Mecke, *Morphological Thermodynamics of Fluids: Shape Dependence of Free Energies*, Phys. Rev. Lett **93** 160601 (2004).
- R. Roth and P.-M. König, *The depletion potential in one, two and three dimensions*, Pramana J. of Phys. **53** 1 (2004).
- P.-M. König, P. Bryk, K. R. Mecke, and R. Roth, *Curvature Expansion of Density Profiles*, Europhys. Lett. accepted (2005).
- K. R. Mecke, T. Hiester, R. Roth, and P.-M. König, *Asymptotic Decay of Correlations in Arbitrary Geometries*, in preparation.
- P.-M. König, S. Dietrich, and R. Roth, *Depletion Potentials Between Complexly Shaped Objects*, in preparation.
- P.-M. König, S. Dietrich, and R. Roth, *Effective Interactions in Biological Key-Lock Systems*, in preparation.
- P.-M. König and R. Roth, *Curvature Expansion, Sum Rules and Morphological Thermodynamics*, in preparation.

# Danksagung

Diese Arbeit wäre nicht möglich gewesen ohne die Unterstützung, die ich von vielen Seiten erfahren durfte. Es ist mir daher eine Freude, den folgenden Personen zu danken, die ganz besonders mit zu dem Gelingen dieser Arbeit beigetragen haben.

**Prof. Dr. S. Dietrich** gab mir die Möglichkeit, mich mit diesem faszinierenden Themengebiet zu beschäftigen. Ich habe viel von verschiedenen Diskussionen profitiert und das MPI in Stuttgart mit den hervorragenden Arbeitsbedingungen als eine sehr inspirierende Arbeitsumgebung schätzen gelernt und viel dadurch profitiert.

**Prof. Dr. C. Bechinger** als Zweitgutachter der Arbeit.

**Dr. R. Roth**, der dieses wirklich sehr interessante Thema vorgeschlagen hat. Viele Diskussionen waren entscheidend für die Entwicklung zentraler Konzepte in dieser Arbeit und es hat stets Spaß gemacht, mit ihm die Physik hinter den Dingen zu suchen. Von seiner Betreuung der Promotion habe ich ganz ausserordentlich profitiert.

**Prof. Dr. K. Mecke** hat Wesentliches zur Interpretationen von verschiedenen Ergebnissen beigetragen. Insbesondere seine Ratschläge zur Morphologie waren stets sehr hilfreich und ich habe viel von seiner Expertise auf verschiedenen Gebieten profitiert.

**C. Grodon**, der mit mir eine gewisse Leidenschaft für Lattenzäune und “nützliche” Shellscrippte teilt. Seine “Polarexpedition” war die Basis für die Asymptotiktheorie und von ihm bekam ich viele nützliche Anregungen.

**T. Hiester**, meinem mathematischen Gewissen. Durch die zahlreichen Diskussionen mit ihm sind Zusammenhänge oft klarer geworden und er hat wesentlichen Anteil an der Entwicklung der “Voodoo”-theorie.

**B. Breidenbach**, meinem programmierstilistischen Gewissen. Seine Anregungen haben mir stets weitergeholfen und die vielen Diskussionen, nicht nur über sehr grundlegende Fragestellungen der Physik, habe ich stets genossen.

**Prof. Dr. R. Evans** and **Dr. P. Bryk** for the excellent collaboration and the fruitful discussions concerning the interpretations of many results.

**C. Goll**, **M. Sprenger**, **Dr. A. Gambassi** und **Dr. F. Schlesener** für die tolle Arbeitsatmosphäre in der Gruppe.

# Curriculum Vitae

Name	Peter-Michael König
Date of birth	29 April 1978
Place of birth	Würzburg
Nationality	German

## Education

1984 - 1988	Grundschule Würzburg-Versbach
1988 - 1997	Riemenschneider-Gymnasium Würzburg
1997 - 1998	Grundwehrdienst

## Studies

1998 - 2000	Universität Würzburg
2000 - 2001	State University of New York (Prof. K. K. Likharev)
2001 - 2001	Universität Würzburg (Prof. W. Hanke)
2002 - 2005	Universität Stuttgart (Prof. S. Dietrich)
since 2002	Max-Planck-Institut für Metallforschung
since 2002	International Max Planck Research School